Meng Wang

Loughborough University

A Tesla-Blumlein PFL-Bipolar

Pulsed Power Generator

by

Meng Wang,   MSc,   BEng

A Doctoral Thesis submitted in partial fulfilment of the requirements for

the award of Doctor of Philosophy of Loughborough University, UK

March 2016

Meng Wang

Acknowledgements

I would like to express my sincere gratitude and to acknowledge the assistance and continuous support received from my supervisor Professor Bucur Novac, who was a constant source of inspiration and expert advice during my research work. I am very fortunate to have been associated with him.

Special thanks are also due to thank Professor Ivor Smith for his efforts and I am also grateful to him for his reviews and advice throughout the writing of the thesis.

I am very grateful to Mr. Keith Stanley for his technical assistance in designing and constructing the experimental systems and his advice related to numerous mechanical problems. Without his help none of the systems described would have been built.

I would also like to thank Mr. Peter Senior and other colleagues in the Plasma and Pulsed Power Group at Loughborough University, for providing friendly help.

I must reserve a special thank you for my parents Mr. Xuemin Wang and Mrs. Shegai Li who supported me during the course of this degree, without their support none of the work described would have been possible.

I would like to thank my husband Mr. Long Yu for his unconditional constant support and patience during this period. He has shared all the achievements and frustrations.

Finally, I would like to thank all my other friends who helped to keep my confidence up and to be there when I needed them.

Meng Wang

Abstract

A Tesla-Blumlein PFL-Bipolar pulsed power generator, has been successfully designed, manufactured and demonstrated. The compact Tesla transformer that it employs has successfully charged capacitive loads to peak voltages up to 0.6 MV with an overall energy efficiency in excess of 90%. The Tesla–driven Blumlein PFL generator is capable of producing a voltage impulse approaching 0.6 MV with a rise time close to 2 ns, generating a peak electrical power of up to 10 GW for 5 ns when connected to a 30 Ω resistive load. Potentially for medical application, a bipolar former has been designed and successfully implemented as an extension to the system and to enable the generation of a sinusoid-like voltage impulse with a peak-to-peak value reaching 650 kV and having a frequency bandwidth beyond 1 GHz.

This thesis describes the application of various numerical techniques used to design a successful generator, such as filamentary modelling, electrostatic and transient (PSpice) circuit analysis, and Computer Simulation Technology (CST) simulation. All the major parameters of both the Tesla transformer, the Blumlein pulse forming line and the bipolar former were determined, enabling accurate modelling of the overall unit to be performed. The wide bandwidth and ultrafast embedded sensors used to monitor the dynamic characteristics of the overall system are also presented. Experimental results obtained during this major experimental programme are compared with theoretical predictions and the way ahead towards connecting to an antenna for medical application is considered.

List of Principal Symbols

L_p primary inductance

L_s secondary inductance

C_p primary capacitance

C_s secondary capacitance

q_p electric charge on primary capacitance

q_s electric charge on secondary capacitance

ω_p resonant frequency of primary circuit

ω_s resonant frequency of secondary circuit

k   coupling coefficient

ω_1 angular resonant frequency of primary circuit

ω_2 angular resonant frequency of secondary circuit

η   energy transfer efficiency

Q_p quality factor of primary circuit

Q_s quality factor of secondary circuit

τ   damping time constant

$M_{i,j}$ mutual inductance between the i_{th} and the j_{th} filaments

r_p inner radius of primary winding

w_p axial length of primary winding

h_p thickness of primary winding

δ   skin depth

Z_i^p position in axis Z of primary filaments

R_i^p position in axis R of primary filaments

K(k)   complete elliptic integral of the first kind

E(k)   complete elliptic integral of the second kind

r_r radius of secondary winding

w_s	axial length of secondary winding
p	axial pitch of the former of secondary rings
R_{s0}	radius to bottom of the first ring of secondary winding
R_{s29}	radius to bottom of the last ring of secondary winding
Z_i^s	position in axis Z of secondary filaments
R_i^s	position in axis R of secondary filaments
E_b	pulse breakdown electric field
Q_i	electric charge of i_{th} conductor
V_j^0	potential of j_{th} conductor relative to conductor 0
$B_{i,j}$	Maxwell coefficients between i_{th} conductor and j_{th} conductor
r_1	radius of Blumlein PFL outer cylinder
r_2	radius of Blumlein PFL middle cylinder
r_3	radius of Blumlein PFL inner cylinder
Z_1	characteristic impedance of Blumlein PFL inner line
Z_2	characteristic impedance of Blumlein PFL outer line
Z'	load impedance of Blumlein PFL
ε_r	relative permittivity of dielectric material
μ_r	relative permeability of dielectric material
l_B	length of Blumlein PFL
v	wave propagation velocity
ε_0	permittivity of vacuum
ρ	resistivity of dielectric
d_1	diameter of bipolar former inner electrode
d_2	internal diameter of bipolar former intermediate electrode
d_2'	outer diameter of bipolar former intermediate electrode
d_3	internal diameter of bipolar former outer electrode
λ_c	cut-off wavelength

f_c cut-off frequency

Contents

List of Tables

List of Figures

1. Introduction

1.1. Introduction to Pulsed Power technology

Pulsed power expresses the technology of building up electrical energy over a relatively long period of time and subsequently releasing it very quickly, resulting in a large amount of instantaneous power over a short period of time as shown in Figure 1.1. The green line indicates the low-level constant power used to charge the capacitors used in a pulsed generator. The red line shows the massive increase in power that can be achieved by releasing the energy in a short, transient pulse, using pulsed power technology.
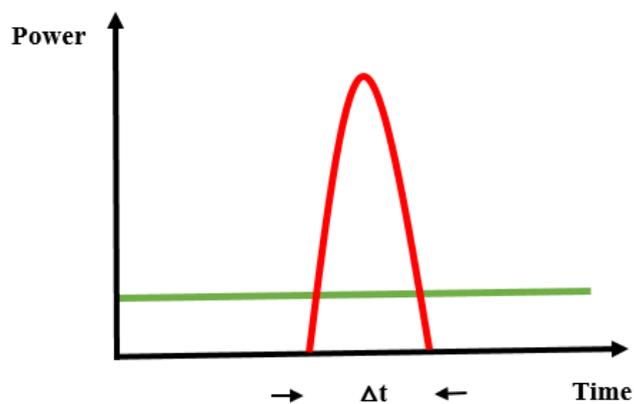
Figure 1.1 Principle of pulsed power

Therefore, the essential idea of pulsed power is that energy is collected from a primary energy source at low power level and, low power density, by a long duration voltage pulse and stored in a large volume energy storage. The energy is then rapidly released with a time compression and volume compression achieved as shown in Figure 1.2. The power is finally delivered to the load at high power level, high power density, by a short duration voltage pulse and used in a much smaller volume. It is important to

note that the time compression is beneficial as it increases the electric field breakdown strength and allows a volume compression that makes the pulsed power systems much more compact.
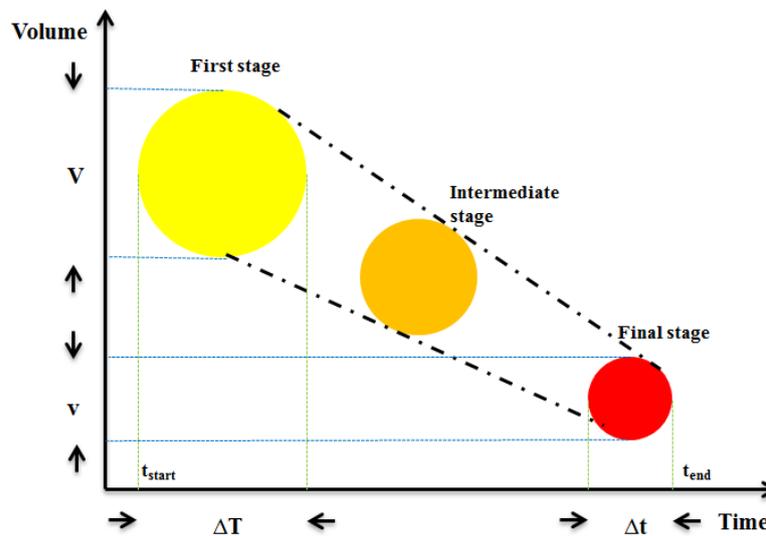
Figure 1.2 Compression stages of a pulsed power generator (4-Dimensions)

In conclusion, pulsed power technology involves the electrical generation of very short voltage pulses (picoseconds to milliseconds) with the possibilities of producing:

➢ Currents up to several hundreds of megamperes.

➢ Voltages up to several megavolts.

➢ Energy release up to several hundreds of trillions of Joules per second. (100s TW)

➢ Power densities up to several hundreds of millions of watts per square centimetre and pressures of millions of atmospheres.

➢ Temperatures of millions of degrees Kelvin.

As already described, a typical scheme of high-power pulsed power generator is always based on an energy store that is charged slowly at a relatively low charging power and, by activating a closing switch, is discharged rapidly. By this procedure, a large power multiplication can always be obtained. In addition to power multiplication,

this scheme can simultaneously be applied to shape or condition the pulse i.e., to create the required rise time and pulse duration. The basic components of a high-power pulsed power generator are shown schematically in Figure 1.3 [1.1].
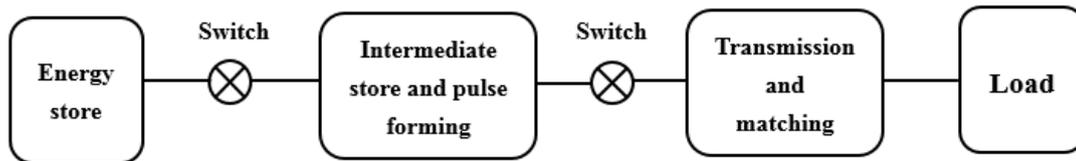
Figure 1.3 Main components of a pulsed power generator

The initial energy can be stored in mechanical springs and flywheels, compressed gas, electric field (capacitors), magnetic field (inductors), electrochemical batteries and others. However, only capacitive energy storage and inductive energy storage have been widely used. The capacitor bank and the Marx generator are two of the most widely employed capacitive-based pulsed power systems [1.2].

Relatively slow pulsed power systems (μs, ns range) may be both constructed using lumped components and described by simple lumped circuit theory. Fast pulsed power systems (ns, ps range) however, are constructed using transmission lines and therefore must be described using transmission line theory. In addition to the generator, consideration must be given to the diagnostics, power controls and other ancillary elements that complete a functional high-power pulsed power generator.

1.2. Literature review

1.2.1. History of Pulsed Power

The initial stage in the development of pulsed power systems was during the Second World War, and was for use in radar technology. A massive developmental programme

was undertaken to understand and use pulsed radar, a technology requiring very short high power pulses. After that, development continued with other related applications, which led to the design and manufacture of several novel pulsed power machines.

At the beginning of the Cold War, when U.S. and Soviet scientist at Los Alamos National Laboratories and Arzamas 16 respectively began the race in the development of nuclear weapons, they also began to investigate the possibility of producing electrical energy by nuclear fusion. The only possibility of reaching this goal was seen in the generation of ultrahigh magnetic fields of 1000 T and more to enable the production of high magnetic pressures for plasma confinement. For the generation of such high fields a device called the Magnetic Flux Compression Generator was invented in the fifties by A. Sakharov in the Soviet Union and Clarence Maxwell Fowler in the U.S.A. [1.3]

After U.S. President Reagan's proclamation of the Strategic Defence Initiative in 1983, often called 'Star Wars', pulsed power technology offered extremely good financial incentives for the development of improved materials and electrical components with high energy and power densities. The United Kingdom and France both participated in this race, but with low budgets compared with those of the U.S. and the Soviet Union. The main topics investigated were electrical devices such as electromagnetic guns, laser weapons and high power microwave weapons. Engineers and scientists began to look elsewhere after the cold war ended, and the financial support for pulsed power was greatly reduced. With the trend to commercial applications, they had to learn very rapidly that the introduction of pulsed power techniques into the commercial market

depended strongly on the competitiveness of their products when compared with those already available using conventional technologies.

In 1997, the International Society of Pulsed Power Applications was founded in Germany with the specific aim of supporting the commercial side of European Pulsed Power applications. Since 2000, the Korean Electro Research Institute (KERI) has also developed pulsed power technology for industrial applications, mostly based on high-power electronics. KERI's activity covers components, military systems and industry applications. Moreover, it has developed several pulsed power supplies responding to industrial needs. Other important research, covering practically the whole range of pulsed power technology, is actively ongoing in China, India and other countries.

1.2.2. Examples of outstanding pulsed power generators

In what follows, a brief outline is provided of four of the most representative pulsed power generators worldwide. Some of the technology required for these generators is also in use in the work described in this thesis.

1.2.2.1. KALIF

KALIF, which stands for 'Karlsruhe Light Ion Facility', is a typical representative of a single-pulse terawatt machine (Figure 1.4). The data for the pulse at the vacuum interface is: power = 1.5 TW, voltage = 1.7 MV, pulse duration = 60 ns, pulse energy = 60 kJ. Its primary energy store is a Marx generator consisting of 25 stages working with oil insulation, with each stage built from two capacitors. After erection of the Marx generator, the energy is transferred to a coaxial water-insulated intermediate storage capacitor. Through a self-breaking water switch, the intermediately stored

energy is transferred to a pulse-forming line. At the exit of the pulse-forming line, a set of 14 self-breaking water switches is distributed over the outer radius of the inner conductor. A fast-rising pulse enters the transmission line and the pulse propagates through a dielectric prepulse slab, which contains 11 gas switches to suppress the prepulse. The pulse itself propagates along the second half of the transmission line, and enters the vacuum chamber containing the load [1.4].
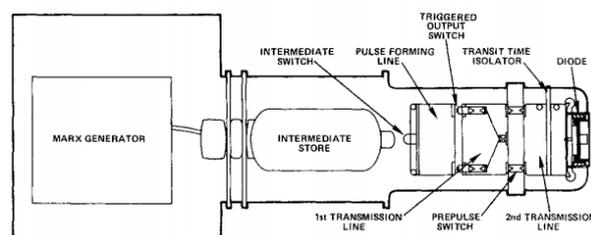
Figure 1.4 Schematic of the pulse generator KALIF [1.4]

1.2.2.2. Z – Machine
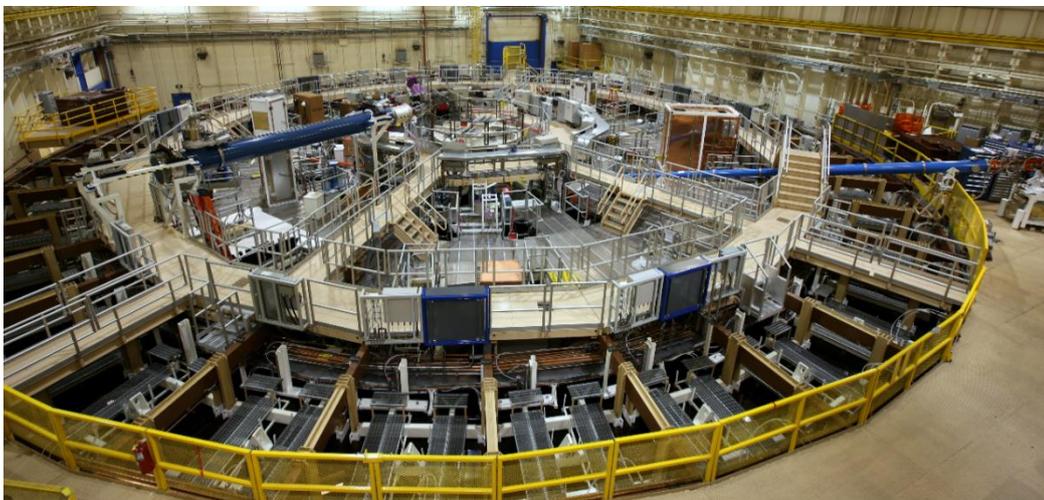
Figure 1.5 Z-Machine at Sandia National Laboratories (USA) [1.5]

At present the largest pulsed power generator in the world is the Z-Machine (Figure 1.5), located at Sandia National Laboratories (USA). The Z-Machine is used to drive Z-pinches, from whence its name. The very elaborate pulsed power design of the machine is based on 36 single-pulse Marx generators, coupled to a water-line pulse-

forming technology as used in its predecessor, the PBFA Ⅱ accelerator [1.1]. The machine stores 12 MJ of electrical energy in the Marx generators and delivers the energy to a water-dielectric coaxial intermediate store within 1 μs. Each Marx generator, has 60, 1.3 μF capacitors charged to a voltage up to 90 kV. The Marx charges the intermediate store at a peak voltage of 5 MV. A low-jitter laser-triggered gas switch is used to couple the energy into a second, lower-impedance coaxial water line during 200 ns. Self-breaking water switches then transfer this energy into a constant-impedance water-dielectric parallel-plate line. The electrical pulse at this point reaches a voltage of 2.5 MV and the pulse has a width of 105 ns full width at half maximum (FWHM). The total power generated in the accelerator at this point is 60 TW [1.5]. The electrical energy is further delivered to an insulator stack, the boundary between the water dielectric and the vacuum that is necessary to drive the z-pinch load, after which it enters into the vacuum portion of the accelerator. There are four levels in the interface to which the lines are connected. The electrical energy is then transmitted through four conically converging, magnetically insulated vacuum transmission lines towards the Z-pinch load. [1.6]

The water transmission lines have a bi-plate, constant-impedance, constant-anode/cathode-gap design. This design optimises the energy efficiency of the transmission lines and maximizes the coupling of the energy in the transmission lines to an inductive load. One of the great achievements of the Z-Machine is the successful design of magnetically-insulated transmission lines (MITLs). These elements consist of four separate, conical-disc feeds, coupled together at the vacuum coil. The MITLs operate successfully at a peak electric field of 2 MV/cm with a very small vacuum gap

of only 1 cm. A critical point in the vacuum power flow is the double post hole coil that couples the four, conical-disc MITLs together. This is to combine the current from each level and to deliver the summed current to the final single z-pinch load without any electric breakdown. [1.6]

1.2.2.3.   RADAN

The RADAN series of pulsed power machines was developed at HCEI, Tomsk and involves a combination of compact pulsed power high-voltage generators and high-current electron accelerators. The basic high-voltage units of RADAN instruments are built around coaxial pulsed forming lines and efficient charging device provided by a Tesla transformer, in contrast to the majority of pulsed power generators that rely on Marx generators. Marx-based machines have been in active service for many years and have played an important role in pulsed power research and development. However, a typical Marx generator is usually very heavy and takes up a large amount of weight and volume. For compactness, the circuitry of all RADAN generators includes a high-voltage pulsed forming line (PFL) with oil insulation, charged using a Tesla transformer, with a gas spark gap switch used to trigger the PFL. The generator includes the charging system, as well as diagnostic tools and control systems [1.7]. The first models of compact nanosecond generators developed at Tomsk were RADAN-150 (150 kV, 2 ns) and RADAN-220 (200 kV, 3 ns). Both machines employed commercial high-voltage pulsed capacitors and high-voltage closing switches (such as gas spark gaps and thyratrons). Their operational experience revealed certain limitations and drawbacks. The basic units were therefore re-developed as new and more powerful RADAN pulsers, resulting in the appearance of

improved models such as RADAN-303 and RADAN-EXPERT generators. The basic

parameters of the RADAN series are shown in Table 1.1. [1.8]

Table 1-1 Basic parameters of high-voltage of RADAN generators

RADAN Series	150	220	303	EXPERT
Type of PFL	Single	Single	Double	Double
Wave impedance, (Ω)	22	22	45	40
Pulse width, (ns)	2	2	4	4
Maximum charging voltage, (kV)	170	220	250	200
Stored energy, (J)	0.7	1.2	5	1.5
Diameter of the coaxial PFL, (mm)	70	102	124	100
Type of high-voltage gas switch	P-43	P-49	Special	Uncontrollable gas switch
Primary voltage, (kV)	3	3 or 5	0.55	0.9
Maximum pulse repetition rate, (Hz)	17	10	100	15
Maximum power consumption, (W)	80	100	1000	Low
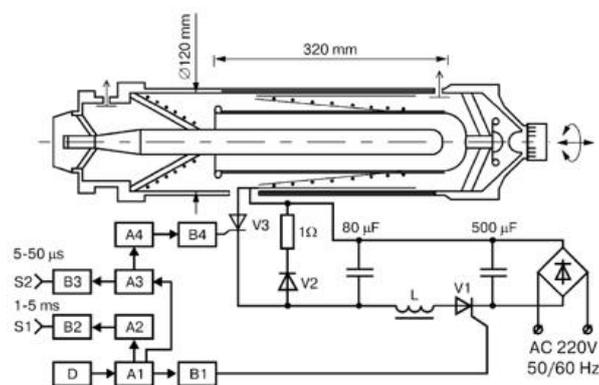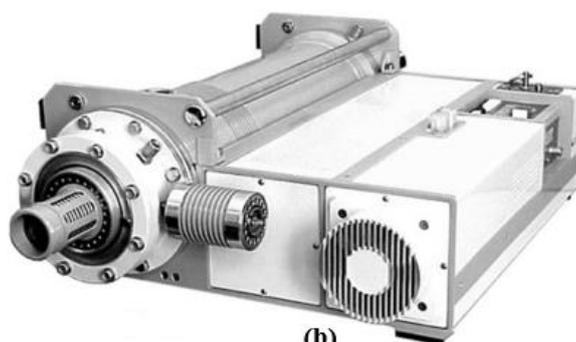
Figure 1.6 (a) design of high-voltage unit, spark gap, and low-voltage circuit of the RADAN-303B pulsed double forming line (PDFL) generator; (b) nanosecond generator RADAN-303B [1.8]

1.2.2.4.   Linear Transformer Drivers (LTDs)

The linear transformer driver (LTD) represents a revolution in pulsed power technology, as a new method for constructing high current, high-voltage pulsed power generators. Fast LTD technology is promising to make pulsed power generators more compact and less expensive, because it does not need any pulse forming lines to produce nanosecond output pulses. The equivalent circuit of a pulsed power generator based on LTD technology is shown in Figure 1.7. The salient feature of the approach is the switching and inductive adding of the pulses at a low voltage directly from the capacitors through low inductance transfer and soft iron core isolation. High currents can be achieved by feeding each core with many capacitors connected in parallel in a circular array. High voltage is obtained by inductively adding many stages in series. In addition to the relative compactness, LTD technology has a number of very significant advantages compared to the established Marx-and-water-PFL technologies. The LTD devices do not require insulating dielectric stacks for high-voltage hold-off and the coaxial voltage adders made of LTDs, and correspondingly the power transmission lines can be directly connected without interface to the final load vacuum chamber, with self-magnetically insulated transmission lines (MITL) transferring the electric power to the load. All the switches operate with pressurized air and not with SF_6, so there are no hazards and no gas recovery units are required. The device is contained within the steel walls of the LTD cavities and is earthed at all times. Hence, the electrical hazard is dramatically reduced and there is no electromagnetic power 'noise' radiated to the surrounding area. In addition, the most important advantage is that LTD drivers offer the possibility of high repetition rate operation. [1.9]
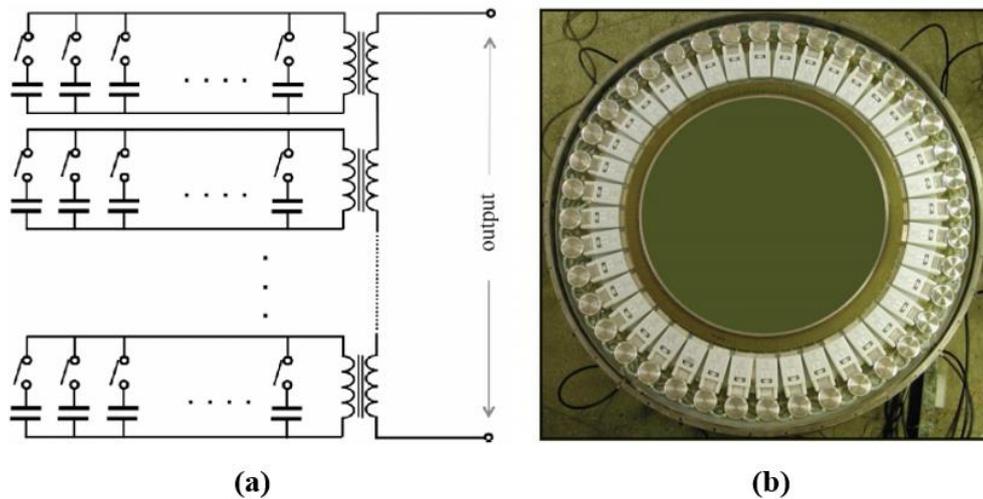
Figure 1.7 (a) equivalent circuit of pulsed power generator based on LTD [1.10]; (b) 1 MA, 100 kV, 70 ns LTD in Sandia Laboratory [1.11]

1.3. Applications of Pulsed Power Technology

Typical applications of pulsed power technology that are becoming widespread include:

a) Production of nano-powders

With the advantages of nano-technology there has been a great demand for a mass production process for the manufacture of nano-sized powders for various industrial applications such as cosmetics, electrodes for MLCC (multi layer ceramic capacitors) and the production of silver fibre for anti-bacterial products. A pulsed power based electric wire explosion can be used to produce in large quantity these nano-particles [1.12]. Nano-particles are larger than individual atoms and molecules but smaller than bulk solids. The main advantages of the pulsed power generation of nano powders are that the particle size can be controlled by varying the injected power and the technique is a cost effective method of producing metal nano powders. [1.13]

b) Plasma-based ion implantation and deposition

Plasma-based ion implantation (PBII) and deposition (PBIID) is another modern technology employing pulsed power technique in material processes. For both surface modification and thin film deposition, PBII surface modification and PBIID coating are applied in a wide range of situations, such as diamond-like carbon materials, coating for space applications, such as the International Space Station, stress reduction and preferred orientation in nitrides, treatment of insulating substrates, treatment of complex structures and inner surfaces [1.14].

c) Food processing

Pulsed electric field (PEF) processing has been demonstrated by many researchers to be equivalent to pasteurization, in terms of its pathogen reduction for a wide range of foods including fluid foods, semisolids and powder foods. Without having any thermal component, PEF has the potential to non-thermally pasteurize several foods via exposure to high-voltage short pulses. Because of this, it also offers considerable benefit in the preservation of taste, colour and nutritional value above other processing techniques that are often heat sensitive and extremely expensive energetically [1.15].

d) Sludge treatment

Sewage sludge is composed of organic materials, bacteria and mostly water. The bacteria contain digested organic materials and the objective of the sewage sludge treatment is to destroy the bacteria cell membranes. High voltage pulsed power can be used to generate an arc discharge (plasma) inside the sludge, which will ensure that this happens [1.16].

e) Inertial confinement fusion

Inertial confinement fusion is a process in which nuclear fusion reactions are initiated by heating and compressing a fuel target, typically in the form of a pellet that most often contains a mixture of deuterium and tritium. Heating can be achieved using a pulsed laser or high power X-ray radiation generated by powerful pulsed power generators. In the case of the Z-Machine described earlier, the extremely large output of pulsed power energy is transferred into a wire array mounted in the z-direction. The very large current flowing along the wire array produces a magnetic field $B(\theta)$, resulting in a $J(z) \times B(\theta)$ force in the radial direction. This z-pinch produces a wire array implosion, thereby releasing a huge bursts of X-ray radiation suitable for heating an inertial confinement fusion (ICF) process [1.17].

f) Bioelectricity and medical applications

Bioelectricity refers to the use of pulsed power and plasma technologies to manipulate cells, tissues and organisms. The application of intense pulsed electric fields with ultra-short durations has been proven to target intracellular structures inside the cell nucleus without permanent damage to the cell membrane. The ultra-short durations of pulses make the cut-off frequency of the Fourier spectrum of the pulses very high, enabling the electric field to penetrate the outer membrane and affect the subcellular structures. This allows modulation of the cell function without permanent damage to the outer cell membrane [1.18].

There are a multitude of medical applications for electroporation, reaching from gene therapy to electrochemotherapy. The most advanced of these applications seems to be

electrochemotherapy, in which a chemotherapeutic drug is injected either into a tumor or intravenously and the tumor is then treated with pulsed electric fields. Cancer treatment has certainly attracted much attention, with extremely short pulse electric fields being applied to the nucleoplasm, to induce apotosis of the cancer cell by triggering its natural death mechanism [1.19].

g) Treatment of exhaust gases

Non-thermal plasma processing is one of the most successful and desirable air-cleaning technologies to control harmful gases in air and to generate ozone. Non-thermal plasmas, in which the mean energy of the electrons is higher than that of the ions and the neutrals in gas, have many kinds of chemically activate radicals, such as O, O_3, N, N^*, N_2^+ and OH [1.19]. Using pulsed power technology, non-thermal plasmas have been generated by a pulsed electron beam or a pulsed streamer discharge, and have been used to treat nitric oxides (NO_X), sulphur dioxide (SO_2), carbon dioxide (CO_2) and volatile organic compounds (VOCs), and to generate ozone (O_3) [1.20].

h) Electromagnetic launcher

The electromagnetic launcher is a device designed for applications both in civilian and military areas. For example, it may be used to produce hypervelocity particles for impact studies, to develop kinetic weapons or to serve as a cost-saving space launcher. Based on their operating principle, electromagnetic launchers may be loosely divided into three basic types: the rail gun, the induction coil gun and the electrothermal gun [1.2].

i) High power microwave

High power microwave (HPM) sources are designed for directed energy weapons applications. The technology used to drive such sources has its root in pulsed power and a comprehensive understanding of their behaviour requires the use of tools that have been previously developed by the plasma physics community. Their development is related to sources of radiation in the microwave portion of the electromagnetic spectrum, extending from approximately 300MHz to 300 GHz. For the case of high average power sources, applications of HPM are: 1) heating and current drive of plasma in tokamaks and other confinement schemes, 2) rf acceleration in high energy linear colliders, 3) radar and communication systems, 4) active denial technology for nonlethal crowd control [1.21] [1.22].

1.4. Aim of the thesis

The main aim of the work performed was to produce new knowledge in pulsed power physics and technology. The work included the design of a 10 GW generator, based on a complete understanding of how various technologies operate together. The other major aim was related to the practical development of a powerful pulsed power generator. After the generator was manufactured and assembled, planned experiments and simulations were conducted to achieve the following goals:

➢ Test the completed Tesla-driven Blumlein PFL on a $30\,\Omega$ load.

➢ Connect the Blumlein PFL to a bipolar pulse former, to generate a bipolar voltage impulse.

➢ Research different combinations of peaking switch and crowbar switch distances to optimise the bipolar pulse former.

➢ Use an innovative and simple high bandwidth V-dot sensor to diagnose the output from the bipolar pulse former.

➢ Compare Computing Simulation Technology (CST) modelling and PSpice simulation results with experimental data.

A schematic design of the system developed is presented in Figure 1.8.
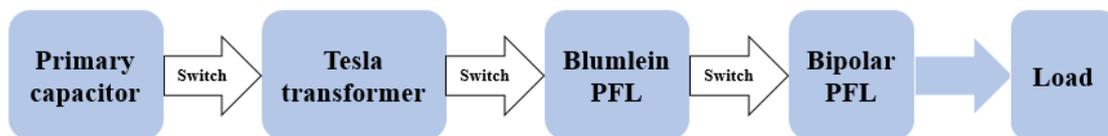
Figure 1.8 Schematics of the pulsed power generator

The intention is to use the completed generator in medical applications. The generator output has a 50 Ω construction and is ideally-matched for powering an antenna. Based on a bespoke designed antenna, the intense pulsed electric field will be considered for use in cancer treatment under water.

1.5. Outline of the thesis

Chapter 1 provides an introduction to the thesis, including an outline of the principle of pulsed power, together with a brief history and also including a literature review of the most important and representative pulsed power generators worldwide. It also describes in a few words the main pulsed power applications and finally summarises the overall aim of the thesis.

Chapter 2 presents details of the Tesla transformer that is used to raise the relatively low voltage of the capacitors to the high voltage required to charge the Blumlein PFL.

A short introduction into Tesla transformer action is followed by a detailed description of the numerical methods used to calculate the transformer parameters required in the design of the unit.

Chapter 3 deals with the 600 kV Blumlein PFL, including the description and design of the electrostatic modelling of the unit.

Chapter 4 details the design of the novel bipolar pulse former. Computing Simulation Technology (CST) modelling is used to optimise the design and help in understanding the experimental results.

Chapter 5 outlines the diagnostics used in the generator. A novel and simple V-dot sensor using off-the-shelf connector is described, capable of measuring GHz bandwidth high voltage pulses in transmission lines.

Chapter 6 presents the experimental arrangements and numerical modelling of the whole system.

Chapter 7 details the main experimental results including a comparison with theoretical prediction.

Chapter 8 summarises the findings and proposes the directions of future work.

A list of publications presented at international conferences and published in prestigious academic journals is provided in chapter 9.

1.6. References

[1.1] H. Bluhm (2006). Pulsed Power Systems: Principle and Applications. Germany: Springer.

[1.2] S T Pai and Qi Zhang (1995). *Introduction to high power pulse technology*. Singapore: World Scientific Publishing Co. Pre. Ltd..

[1.3] N. R. Pereira and J. Davis. (1988). X-rays from Z-pinches on relativistic electron-beam generators. *Journal of Applied Physics*. 64 (3), ppR1-R2.

[1.4] H. Bluhm, K. Boehnel, L. Buth, P. Hoppe, H. U. Karow, A. Klumpp, D. Rusch, T. Scherer, U. Schuelken, J. Singer (1985). Experiments of KFK's Light-Ion Accelerator KALIF. *Proc. 5th IEEE International Pulsed Power Conference*. Arlington, Virginia, USA. pp114-117.

[1.5] Sandia National Laboratories. Available: http://www.sandia.gov/z-machine/. Last accessed 14th Nov 2015.

[1.6] R. B. Spielman, W. A. Stygar, J. F. Seamen, F. Long, H. Ives, R. Garcia, and T. Wagoner (1997). Pulsed power performance of PBFA Z. *Proc. 11th IEEE International Pulsed Power Conference*. Baltimore, Maryland, USA. pp709-714.

[1.7] M. I. Yalandin and V. G. Shpak. (2001). Compact High-Power Subnanosecond Repetitive-Pulse Generators (Reviews). *Instruments and Experimental Techniques*. 44 (3), pp285-310.

[1.8] G. A. Mesyats, S. D. Korovin, V. V. Rostov, V. G. Shpak and M. I. Yalandin. (2004). The RADAN Series of Compact Pulsed Power Generators and Their Applications. *Proceedings of the IEEE*. 92 (7), pp1166-1179.

[1.9] M. G. Mazarakis, W. E. Fowler, K. L. LeChien, F. W. Long, M. K. Matzen, D. H. McDaniel, R. G. McKee, C. L. Olson, J. L. Porter, S. T. Rogowski, K. W. Struve, W. A. Stygar, J. R. Woodworth, A. A. Kim, V. A. Sinebryukhov, R. M. Gilgenbach, M. R. Gomez, D. M. French, Y. Y. Lau, J. C. Zier, D. M. VanDevalde, R. A. Sharpe and K. Ward. (2010). High-Current Linear Transformer Driver Development at Sandia National Laboratories. *IEEE Transactions on Plasma Science.* 38(4), pp704-713.

[1.10] Weihua Jiang. (2013). Repetition rate pulsed power technology and its applications: (V) The implication of pulse adding. *High Power Laser and Particle Beams*. 25 (8), pp1877-1882.

[1.11] M. G. Mazarakisaa, W. E. Fowler, F. W. Long, D. H. McDaniel, C. L. Olson, S. T. Rogowski, R. A. Sharpe, and K. W. Struve (2005). High Current Fast 100-ns LTD Driver Development in Sandia Laboratory. *Proc. 15th IEEE International Pulsed Power Conference*. Monterey, California, USA. pp390-393.

[1.12] Weihua Jiang and Kiyoshi Yatsui. (1998). Pulsed Wire Discharge for Nanosize Powder Synthesis. *IEEE Transactions on Plasma Science*.26 (5), pp1498-1500.

[1.13] R. Sarathi, T. K. Sindhu, S. R. Chakravarthy and R. Jayaganthan. (2007). Processing and characterization of Nano Aluminium powder Using Electric Explosion process (EEP). *Proc. 16th IEEE International Pulsed Power Conference*. Albuquerque, New Mexico, USA. pp391-394.

[1.14] Jacques Pelletier and Andre Anders. (2005). Plasma-Based Ion Implantation and Deposition: A Review of Physics, Technology, and Applications. *IEEE Transaction on Plasma Science*. 33 (6), pp1944-1959.

[1.15] M. M. Gongora-Nieto, D. R. Sepulveda, P. Pedrow, G. V. Barbosa-Canovas, B. G. Swanson. (2002). Food Processing by Pulsed Electric Fields: Treatment Delivery, Inactivation Level, and Regulatory Aspects. *LWT - Food Science and Technology*. 35 (5), pp375-388.

[1.16] Akira Mizuno, Yuji Hori. (1988). Destruction of living cells by pulsed high voltage application. *IEEE Transactions on Plasma Science*. 24 (3), pp387-394.

[1.17] M. G. Haines, T. W. L. Sanford and V. P. Smirnov. (2005). Wire-array z-pinch: a powerful x-ray source for ICF. *Plasma Physics Control Fusion*. 47, ppB1-B11.

[1.18] Karl H. Schoenbach, SunaoKatsuki, Robert H. Stark. (2002). Bioelectrics— New Applications for Pulsed Power Technology. *IEEE Transactions on Plasma Science.* 30(1), pp293-300.

[1.19] H. Akiyama, T. Sakugawa, T. Namihira, K. Takaki, Y. Minamitani and N. Shimomura. (2007). Industrial Applications of Pulsed Power Technology. *IEEE Transactions on Dielectric and Electrical Insulation*. 14 (5), pp1051-1064.

[1.20] T. Oda. (2003). Non-thermal plasma processing for environmental protection: decomposition of dilute VOCs in air. *Journal of Electrostatics*. 57, pp293-311.

[1.21] Steven H. Gold, Gregory S. Nusinovich. (1997). Review of high-power microwave source research. *Review of Scientific Instruments*. 68 (11), pp3945-3974.

[1.22] E. Schamiloglu. (2004). High Power Microwave Sources and Applications. *Proc. Microwave Symposium Digest, 2004 IEEE MTT-S International.* 2, pp1001-1004.

2. Tesla transformer

2.1. Introduction and history of Tesla transformers

Air core pulse transformers normally operate either at very high power levels or ultrahigh RF frequencies. One of their advantages is that since there is no magnetic core, problems with magnetic saturation do not arise. However in order to achieve good flux linkage between the primary and secondary windings, these need to be located very close to one another, and despite this their coupling coefficients (k) tend to be lower than those of magnetic core transformers, particularly those having a high gain.

A further important advantage is that air core transformers are not limited by either current handling capacity or magnetic saturation of their core. They are usually used in different applications to more conventional transformers, with their predominant use being for charging capacitive loads, such a pulse forming lines (PFLs) or high-voltage capacitors, to the required high potential, which may run into the MV range and be at an energy level exceeding hundreds of kJ. Their energy source is usually a relatively low-voltage capacitor, which is often rapidly discharged into a single-turn coil.

In general, there are two basic types of high voltage air core pulse transformer, which can be operated up to megavolt levels [2.1]. The first and most common is the single layer helical winding and the second is the spiral-strip winding, with these differing from one other primarily in the arrangement of the secondary windings. Each has its own merits and drawbacks. Helical transformers have a low coupling coefficient

(k<0.8), and in the present work they were used for the Tesla generator because of their ease of manufacture and ability to support an extremely high secondary/primary turns ratio. They have a low secondary winding capacitance and can be easily be adapted to a coaxial geometry. By comparison, the main advantage of the spiral strip type is that they may have a high coupling coefficient, usually exceeding 0.9. They have a coaxial output, as is required by most loads, but are relatively complex to manufacture and have a very high secondary capacitance. There are two problems common in both types of winding. One is the turn-to-turn electrical breakdown, which is most common with helical transformers used in charging systems for pulse forming lines (PFLs). Because the rise time of the voltage transient is short (less than 10ns) and is generated by the discharge of the PFL into the output of a directly coupled transformer, the breakdown problem can be serious. The capacitances between turns and from each turn to ground are normally sufficient to fast rising transients. Consequently, a voltage pulse approaching the fall amplitude of the transient can momentarily appear across the final turns of the secondary winding and cause a breakdown. The other problem is partial shorting from eddy currents induced in the voltage-grading devices and structural components present in high-voltage transformers. [2.2]

The Tesla transformer is named after Nikola Tesla who was born in Smiljan, Croatia, in 1856. Between 1899-1900, he worked in his laboratory in Colorado Springs where he developed the types of air-cored high voltage resonant transformers now known as Tesla transformers or Tesla coils [2.3]. His revolutionary work is well reported in a series of patents. The first record of his air-cored transformer is dated 1891 and

appeared in the patent 'System of electric lighting', which described their use in the generation of high voltages at high frequency for the production of light [2.4]. His resonant transformer was originally named "Apparatus for transmitting electrical energy" in a 1914 patent [2.5], since it was intended for transferring electrical energy without wires to lamps and possibly other devices.

The first mathematical analysis of Tesla's air core transformer is due to Oberbeck in 1895. The transformer was treated as two air coupled resonant circuits and the analysis examined the case where the two coupled circuits are tuned to resonate at the same frequency [2.6].

In a later paper, dated 1904, P. Drude proved that the maximum output voltage is achieved in the secondary circuit of a Tesla transformer by tuning the primary and secondary circuit to resonate at the same frequency and by having a coupling coefficient of 0.6 [2.6].

In 1966 D. Finkelstein, presented the dual resonance condition under which complete energy transfer from the primary circuit to the secondary circuit takes place. He went on to show that for any coupling coefficient other than 0.6, the instant at which the complete energy transfer takes place is delayed. The design he proposed used a spiral-strip type secondary winding wound on an acrylic former, with the inter-turn insulation provided by multi-layered Mylar. A Mylar film was also used to insulate the single-turn primary winding from the multi-turn secondary winding. De-ionised water insulated the transformer within its housing, enabling it to withstand an output voltage up to 1 MV. The transformer was used with a variety of loads, including exploding

wires and high-voltage water filled capacitors and also to test a water-filled spark gap. [2.7]

F. M. Bieniosek in 1990, presented an analysis for a triple resonance transformer circuit i.e. three coupled circuit all in resonance, used to improve the output efficiency of the MEDEA II electron accelerator [2.8]. The stray capacitance of the spiral secondary winding was comparable to that of the load capacitance, and as a consequence a significant quantity of energy remained stored in the stray capacitance and was not delivered to the load. The inclusion of a suitable inductor between the transformer secondary winding and the load, enables the circuit to operate in the triple resonance mode, thereby increasing the energy transfer efficiency to the load. Due to this design change, there was however a reduction in the peak voltage across the secondary winding. [2.8]

A compact and repetitive Tesla transformer based pulsed accelerator was developed separately by G. A. Mesyats in 1991 and Yu. A. Andreev in 1997, at the Institute of Electro-physics (IEP) and the Institute of High Current Electronics (IHCE) respectively, both in Russia. The pulsed power source of these accelerators is based on a Tesla transformer integrated with an oil-insulated coaxial pulse-forming line with an open steel magnetic core to increase the coupling coefficient to almost unity. The secondary winding was wound on a conical former and the voltage step-up ratio was very high. This ensured that the charging voltage of the primary capacitor bank could be less than 1 kV, enabling low voltage capacitors and switches to be used in the primary circuit, to both help reduce the cost and to solve problems arising from a high-voltage in the primary circuit. [2.9] [2.10]

J. L. Korioth in 1999, proposed a design with a 'super low' inductance primary (SLIP), for use in dual resonant transformers, with the aim of making the primary arrangement of capacitor bank and switch both compact and of low inductance. One unit used two 6″ long, 8″ diameter coaxial cylinders, with twelve 2 nF primary capacitors and a hydrogen spark-gap switch placed between a slit in the conductive cylinders. The primary widing inductance was 200 nH and the resonant frequency about 2.1 MHz. [2.11]

M. Denicolai in 2002, confirmed that to achieve an optimal performance, the primary and secondary coils should resonate at the same frequency and that the coupling coefficient should be 0.6. He also showed that, to minimise the losses in the transformer, it is essential for the maximum voltage generated in the secondary winding to be obtained in the shortest possible time. [2.12]

2.2. Tesla transformer theory

The typical Tesla transformer consists of two inductively coupled and damped resonant circuits as shown in Figure 2.1, in which subscripts (p) and (s) identify the inductance (L), capacitance (C) and resistance (R) of the primary and secondary circuits, and (M) is the mutual inductance between the two circuits.
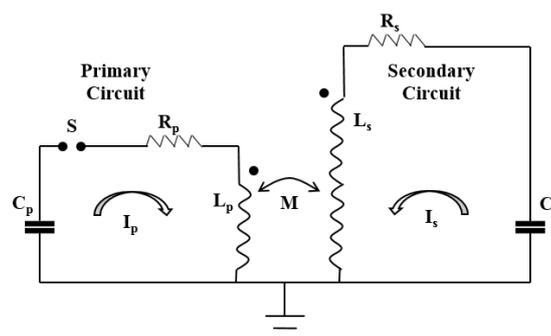
Figure 2.1 Primary and secondary circuit of a Tesla transformer

The primary circuit contains a high voltage capacitor C_p which is discharged through the closing switch S often a spark gap into the low inductance primary coil L_p. The secondary circuit comprises coil L_s with one side earthed and a capacitor C_s. If the two coils are magnetically coupled, every discharge of the primary capacitor generates a magnified voltage in the secondary coil [2.7]. The primary capacitor is initially charged, and when the switch S is closed, the energy stored in the capacitor feeds the inductor. Current flows back and forth through the inductor and the spark gap, to and from the capacitor, at a resonant frequency determined by the values of C_p and L_p. The amplitude decays towards zero at a rate which is a function of the circuit losses. Part of the energy is magnetically coupled into the secondary L_s. The operation of the transformer is described by the following equations.

Applying Kirchhoff's law after the switch S is closed gives for the primary circuit [2.13]:

$$\frac{1}{C_p} \int i_p \, dt + R_p i_p + L_p \frac{di_p}{dt} + M \frac{di_s}{dt} = 0 \tag{2.01}$$

and for the secondary circuit:

$$\frac{1}{C_s} \int i_s \, dt + R_s i_s + L_s \frac{di_s}{dt} + M \frac{di_p}{dt} = 0 \tag{2.02}$$

The instantaneous charges q_p and q_s on capacitors C_p and C_s are:

$$i_{p,s} = \frac{dq_{p,s}}{dt} \tag{2.03}$$

substituting this equation into equations (2.01) and (2.02), rearranging and introducing the differential operator with respect to time t $D \left(= \frac{d}{dt} \right)$ yields [2.14]:

$$\left[D^2 + \frac{R_p}{L_p}D + \omega_p^2\right]q_p + k\sqrt{\frac{L_s}{L_p}}D^2q_s = 0 \qquad (2.04)$$

$$\left[D^2 + \frac{R_s}{L_s}D + \omega_s^2\right]q_s + k\sqrt{\frac{L_p}{L_s}}D^2q_p = 0 \qquad (2.05)$$

where

$$k = \frac{M}{\sqrt{L_pL_s}} \qquad (2.06)$$

and

$$\omega_p = \frac{1}{\sqrt{L_pC_p}} \qquad (2.07)$$

$$\omega_s = \frac{1}{\sqrt{L_sC_s}} \qquad (2.08)$$

where ω_p and ω_s are the resonant frequencies of the uncoupled primary and secondary circuits, and *k* is the coupling coefficient ($0 < k < 1$). Equations (2.04) and (2.05) can be solved numerically (for example by a Runge Kutta method) [2.15].

By considering two special cases; (1) in which the resistive losses in the circuit are neglected i.e. $R_p = R_s = 0$ a complete analytical solution is possible and (2) when the primary and secondary resonant frequencies are matched $\omega_p = \omega_s$ and a low-loss approximate solution is possible, which assists in determining the important parametric factors.

2.2.1. Lossless circuit ($R_p = R_s = 0$)

Substituting $R_p = R_s = 0$ into equations (2.04) and (2.05) and solving for V_s yields [2.16]:

$$V_s(t) = V_0 \sqrt{\frac{L_s}{L_p}} \frac{2k}{\sqrt{(1-T)^2 + 4k^2 T}} sin\left(\frac{\omega_2 + \omega_1}{2} t\right) \times sin\left(\frac{\omega_2 - \omega_1}{2} t\right) \qquad (2.09)$$

in which, $T = \frac{\omega_p{}^2}{\omega_s{}^2}$ and

$$\omega_1 = \omega_s \sqrt{\frac{(1+T) - \sqrt{(1-T)^2 + 4k^2 T}}{2(1-k^2)}} \qquad (2.10)$$

$$\omega_2 = \omega_s \sqrt{\frac{(1+T) + \sqrt{(1-T)^2 + 4k^2 T}}{2(1-k^2)}} \qquad (2.11)$$

where, ω_1 and ω_2 are the angular resonant frequencies of the primary and secondary circuits when coupled. Their values are always real and clearly $\omega_2 > \omega_1$. From equation (2.09) it can be seen that the secondary voltage has a high oscillation frequency $\frac{\omega_1 + \omega_2}{2}$ which is amplitude modulated by a second and lower frequency oscillation $\frac{\omega_2 - \omega_1}{2}$.

Equation (2.09) shows that the maximum voltage across the secondary capacitance can be expressed as

$$V_0 \sqrt{\frac{L_s}{L_p}} \frac{2k}{\sqrt{(1-T)^2 + 4k^2 T}}$$

which can be achieved only if both sine terms in equation (2.09) are simultaneously equal to ± 1 and are related by

$$(\omega_2 + \omega_1)t = (2n + 1)\pi \tag{2.12}$$

and

$$(\omega_2 - \omega_1)t = (2m + 1)\pi \tag{2.13}$$

where *n* and *m* are integers. The earliest time at which the maximum secondary voltage will occur is when $m = 0$ and thus $t = \pi/(\omega_2 - \omega_1)$. Substituting and rearranging equations (2.12) and (2.13) then yields

$$\frac{\omega_2}{\omega_1} = \frac{1+n}{n} \tag{2.14}$$

and on substituting equations (2.10) and (2.11) into (2.14)

$$k = \sqrt{\frac{\left(\frac{2n+1}{2n^2+2n+1}\right)^2 (T+1)^2 - (1-T)^2}{4T}} \tag{2.15}$$

The energy transfer efficiency η is

$$\eta = \frac{\frac{1}{2}C_s V_{max}^2}{\frac{1}{2}C_p V_0^2} \tag{2.16}$$

where V_{max} is the maximum voltage achieved across the secondary capacitance during the time period $t \leq \pi/(\omega_2 - \omega_1)$. Satisfying the condition of equations (2.12) and (2.13) gives

$$\eta = \frac{4k^2 T}{(1-T)^2 + 4k^2 T} \tag{2.17}$$

Complete energy transfer takes place, when $\eta = 1$ and $T = 1$ which requires that the resonant frequencies of the primary and secondary circuits are matched. The maximum voltage across the secondary capacitance is then

$$V_S = V_0 \sqrt{\frac{L_S}{L_p}} \text{ , when } k = \frac{2n+1}{2n^2+2n+1} \tag{2.18}$$

Since the lossless circuit is impractical, the analysis provides only an upper limit to the actual transformer performance. The operating condition is also generally unrealistic because of the practical difficulties in constructing high-voltage, high-gain transformers. Then analysis of the second and low-loss circuit is given below.

2.2.2. Low-loss circuit

The lossless assumption is clearly only approximate, as any practical transformer has losses in both the primary and secondary circuits. The ohmic resistance losses are greatly enhanced by skin and proximity effects as the resonant frequency increases, and the dielectric loss in the capacitors also increase at the same time and appear as an increased effective series resistance (ESR). Perhaps the major contribution however comes from the time dependent electrical breakdown phenomena in the spark gap switch.

With the quality factor of the primary and secondary circuits defined as [2.13], the Q factor of the two circuits are:

$$Q_p = \frac{\omega_p L_p}{R_p} \tag{2.19}$$

$$Q_s = \frac{\omega_s L_s}{R_s} \tag{2.20}$$

and an approximate expression for the secondary voltage across the secondary winding capacitance is [2.2]

$$V_s(t) = \frac{V_0}{2}\sqrt{\frac{L_s}{L_p}} e^{\left(\frac{-t}{\tau}\right)}\left[\cos\left(\frac{\omega t}{\sqrt{1-k}}\right) - \cos\left(\frac{\omega t}{\sqrt{1+k}}\right)\right] \qquad (2.21)$$

where V_0 is the initial charging voltage, $\tau = \frac{4Q_pQ_s(1-k^2)}{\omega(Q_p+Q_s)}$ is the damping time constant, and $\omega = \omega_p = \omega_s$ is the angular frequency of the applied voltage [2.15].

A Tesla transformer design can be optimised to achieve the highest secondary voltage, with the maximum voltage gain being [2.12]

$$G_{max} = \left[\frac{V_2(t)}{V_1}\right]_{max} = \frac{2k}{\sqrt{\sqrt{(1-T)^2+4k^2T}}}\sqrt{\frac{L_2}{L_1}} \qquad (2.22)$$

In the lossless case the requirements of equations (2.12) and (2.13), where *n* and *m* are integers, are extremely important. However, without losing generality, m can be set to zero, thereby changing the requirements to simply

$$\frac{\omega_2}{\omega_1} = \frac{1+n}{n} \qquad (2.23)$$

To make time t as small as possible so that the maximum voltage occurs in the shortest time from $t = 0$, assume $n = 1$, which yields the condition:

$$\omega_2 = 2\omega_1 \qquad (2.24)$$

In addition, if Z is the impedance operator for two parallel and coaxial circular loops [2.7], it can be written as equation (2.25), where M is the mutual inductance between the two loops:

$$Z = \begin{bmatrix} j\omega L_p + {}^1\!/\!_{j\omega C_p} & j\omega M \\ j\omega M & j\omega L_p + {}^1\!/\!_{j\omega C_p} \end{bmatrix} \tag{2.25}$$

introducing substitutions (2.06), (2.07) and (2.08), enables equation (2.25) to be rewritten as

$$(1 - k^2)\omega^4 - (\omega_p^2 + \omega_s^2)\omega^2 + \omega_p^2\omega_s^2 = 0 \tag{2.26}$$

For complete energy transfer, the two electrical circuits must have same resonant frequency $\omega_p = \omega_s$, in which case equation (2.26) becomes

$$(1 - k^2)\omega^4 - 2\omega_p^2\omega^2 + \omega_p^4 = 0 \tag{2.27}$$

with roots ω_1 and ω_2, where

$$\omega_{1,2}^2 = \omega_p^2 \left[{}^{(1 \pm k)}\!/\!_{(1 - k^2)} \right] \tag{2.28}$$

The ratio of the square of the two frequencies is

$$\omega_2^2 \!/\!_{\omega_1^2} = {}^{(1 + k)}\!/\!_{(1 - k)} \tag{2.29}$$

Combining equation (2.24) and (2.29)

$${}^{(1 + k)}\!/\!_{(1 - k)} = 4$$

$$k = {}^3\!/\!_5 = 0.6$$

The requirements that $\omega_p = \omega_s$ and $k = {}^3\!/\!_5 = 0.6$ provide the criterion for selecting the Tesla parameters for maximum voltage gain and maximum energy transfer from the primary circuit to the secondary circuit.

2.3. Modelling of Tesla transformer

2.3.1. Filamentary modelling

2.3.1.1.   Introduction to filamentary modelling

When electrical pulses are present in an electromagnetic field, the transient behavior of both the electric currents and magnetic fields are fully described by Maxwell's Equations. For low-frequency problems these can be reduced to the diffusion equations commonly used to describe the similar physics of electric current and magnetic field penetration into a conductor. Depending on the details of the problem under investigation, the diffusion equation can be solved using several different methods with judiciously selected boundary conditions. Magnetohydrodynamic modelling is the conventional technique. Unfortunately it is a very demanding task to apply this technique to a complex arrangement or to determine the ohmic heating and the electromagnetic forces. In the past such considerations have led to the development of extremely complex numerical codes, run on large computers in laboratories developing nuclear weaponry. On occasions, the costs involved have even been so high as to exceed the cost of an actual experiment. Alternative codes that employ finite element analysis (FEA) are available commercially, and are used currently at Loughborough to solve difficult multi-physics problems [2.17], but these are again invariably complex and costly.

Filamentary modelling is a simple but accurate and general-purpose numerical technique that enables a full description of electromagnetic, thermal and dynamic interactions to be included in a model, while still preserving considerable mathematical

simplicity. It provides a very useful tool when more advanced codes are either unavailable or too costly, or when fast preliminary designs of complex implosion machines are required. It owes much to work developed at Loughborough University [2.18-2.24], with a long history of progressively more complicated and refined theoretical models attempting to reproduce as accurate as possible reliable experimental data. Loughborough has recently introduced a number of novel features into the modelling, mostly related to the fast dynamics of imploding/exploding structures, and has successfully applied the technique in a very wide range of pulsed power applications, including explosively driven flux-compression generators [2.19], multi and single-turn inductive launchers [2.20-2.21], and electromagnetic flux-compression [2.22]. The technique has also been used to provide an improved understanding of a novel electromagnetic technique developed for remote activation through thick metallic shields [2.23].

Filamentary modelling is an accurate technique used to calculate the Tesla transformer parameters. The transformer is divided into a large collection of circular current filaments. The filaments are sufficiently small for the current distribution in their cross sectional areas to be regarded as constant and, as a rule of thumb, the dimensions will be much less than the equivalent skin depth. The number of filaments required to describe accurately the parameters under transient condition is obtained by calculating the parameters for a relatively small numbers of filaments, and then repeating the calculation for an increased number, until the difference between the two calculations is less than 0.1% [2.24].

Once the replacement of the solid conductors by the current filaments is complete, the resistance of each filament is determined from its cross-sectional area, length and temperature dependent resistivity. By assuming a uniform current distribution across the cross section of the filaments, the self-inductances can readily be calculated from well-known formula, as can the mutual inductance between every possible pair of filaments. Thereby the electromagnetic problem is reduced to a simple circuit problem, in which the solid conductors are represented by an assembly of current filaments. The currents in each branch are defined as state variables, and the circuit equations are written as a set of linear first order differential equations that have to be solved for the circuit currents. A typical set of equations will appear in matrix form as:

$$\frac{d}{dt}\begin{bmatrix} M_{1,1} & M_{1,2} & & M_{1,N} \\ M_{2,1} & M_{2,2} & \cdots & M_{2,N} \\ & \vdots & \ddots & \vdots \\ M_{N,1} & M_{N,2} & \cdots & M_{N,N} \end{bmatrix}\begin{bmatrix} I_1 \\ I_2 \\ \vdots \\ I_N \end{bmatrix} = \begin{bmatrix} V_1 \\ V_2 \\ \vdots \\ V_N \end{bmatrix} \tag{2.30}$$

where N is the number of filaments, $\frac{d}{dt}$ is the time derivative, I_i (i=1…N) is the current in the i_{th} filament. V_i(i=1…N) is the complete inductive voltage term in the circuit including the i_{th} filament and $M_{i,j}$ (i,j=1…N) is the mutual inductance between the i_{th} and j_{th} filaments. When i=j, $M_{i,j}$ becomes L_i, the self-inductance of the i_{th} filament [2.25]. Equation (2.30) can be written in compact form as:

$$\frac{d}{dt}\left(\sum_{j=1}^{N} M_{i,j}I_j\right) = V_i \quad (i = 1 \dots N) \tag{2.31}$$

The set of first order differential equations that corresponds to the filamentary circuit model can be solved using numerical ordinary differential equation solvers such as the Runge-Kutta technique, with the filamentary currents thus calculated providing the

current distribution in the conductors. Most electromagnetic devices in pulsed power have rotational symmetry about one axis, so the model of Tesla transformer can be restricted to one in cylindrical co-ordinates with symmetry about the Z-axis. In the following sections, it is shown how the self and mutual inductance associated with coils can be determined.

2.3.1.2. Self-inductance of primary winding

The primary winding of the Tesla transformer is a single-turn copper sheet, wound on a cylindrical plastic mandrel as shown in Figure 2.2. The copper sheet is sandwiched and heat bonded between two layers of Mylar-polyethylene laminate, to provide improved isolation. For the present Tesla design, the dimensions used the following input data for filamentary modelling calculations are: r_p (inner radius)=170.25 mm, w_p (axial length)=152 mm, h_p (thickness)=0.15 mm, δ (skin depth)=0.065 mm. The 2D filamentary representation of the primary winding is shown in Figure 2.3.
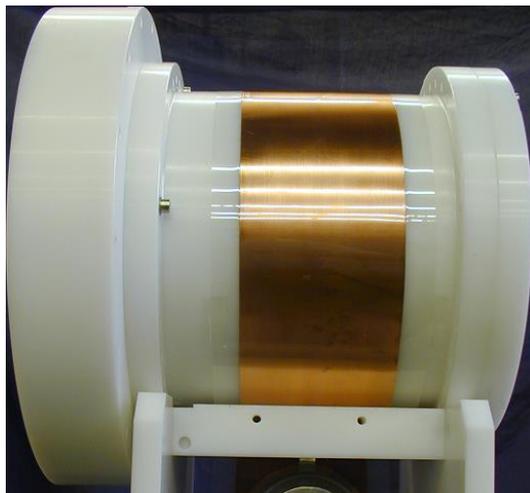
Figure 2.2 Primary winding of Tesla transformer
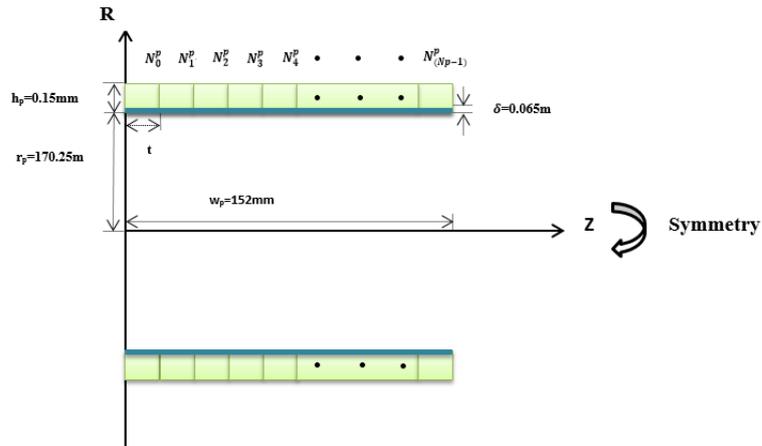
Figure 2.3 2D Filamentary representation of primary winding

In Figure 2.3, the primary winding is divided into N_p filaments as thin tapes. According to the axial and radial dimensions, the place of every tape in axes (Z, R) can be defined by:

$$Z_i^p = \frac{(2i+1)}{2} t = \frac{(2i+1)}{2} \times \frac{w_p}{N_p} \qquad (2.32)$$

$$R_i^p = r_p + \frac{\delta}{2} \qquad (2.33)$$

The self-inductance of a thin tape can be taken as [2.26]:

$$L_i^p(R_i^p, t) = \mu_0 R_i^p \left[\ln\left(\frac{8R_i^p}{t}\right) - 0.5 \right] \qquad (2.34)$$

where μ_0 is the permeability of free space.

The mutual inductance between two thin tapes can be calculated using the formulas [2.26]:

$$M_{i,j}^p = \frac{2\mu_0 \sqrt{R_i^p \cdot R_j^p}}{k} \left[\left(1 - \frac{k^2}{2}\right) K(k) - E(k) \right] \qquad (2.35)$$

where

$$k = \sqrt{\frac{4 \cdot R_i^p \cdot R_j^p}{\left(R_i^p + R_j^p\right)^2 + \left(Z_i^p - Z_j^p\right)^2}} \tag{2.36}$$

K(k) is the complete elliptic integral of the first kind:

$$LegendreK(k) = \int_0^1 \frac{1}{\sqrt{(1-t^2)(1-k^2t^2)}} dt \tag{2.37}$$

and E(k) is the complete elliptic integral of the second kind:

$$LegendreE(k) = \int_0^1 \sqrt{\frac{1-k^2t^2}{1-t^2}} dt \tag{2.38}$$

Once the filamentary current is known, the magnetic energy stored in all the filamentary self and mutual inductances can be calculated at any time during discharge of the capacitor bank. The total energy stored in a winding can be found directly by adding the magnetic energy associated with each of the filaments and the result obtained must be equal to the energy stored in the corresponding element of the lumped component model given by $\frac{LI^2}{2}$. According to equations (2.30), (2.34) and (2.35), the inductance of primary winding can be taken as given by [2.26]:

$$L_p = \frac{\sum_{i=0}^{Np-1} \sum_{j=0}^{Np-1} M_{i,j} I_i I_j}{2\left(\sum_{i=0}^{Np-1} I_i\right)^2} \tag{2.39}$$

The number of filaments is determined by calculating the inductance of the primary winding from a small number, and then repeating the calculation. The percentage differences between calculations based on $N_P=1000$ are shown in Figure 2.4.
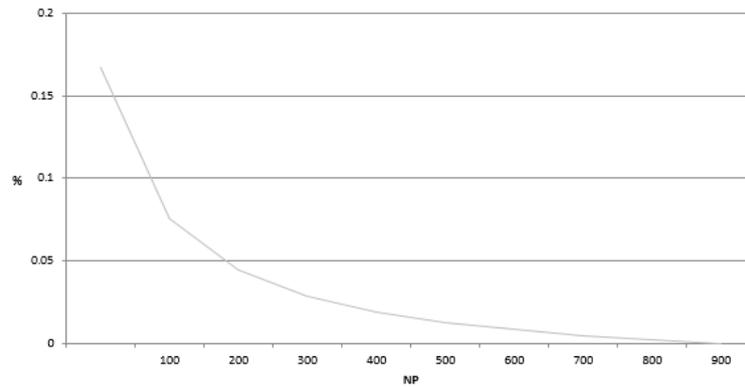
Figure 2.4 Differences between filamentary calculations of primary winding

From Figure 2.4, N_p=500 was chosen for convenience to calculate the inductance and

the result obtained was $L_p = 375nH$.

2.3.1.3.   Self-inductance of secondary winding

The secondary winding is of helical form to avoid any breakdown at the high-voltage

end of the winding and is wound on a plastic conical former as evident in Figure 2.5.

The high voltage will appear at the upper end and the lower end is earthed.

Figure 2.5 Secondary winding of Tesla transformer

Filamentary modelling of the secondary winding is represented in cross-section in Figure 2.6 for a collection of 30 filamentary rings. For the present Tesla design, the dimensions used the following input data for filamentary modelling calculations: r_r(radius)=0.625 mm, w_s (axial length)=180 mm, p (axial pitch of the former)=6 mm, R_{s0} (radius to bottom of first ring)=150 mm, R_{s29} (radius to bottom of last ring)=91 mm.
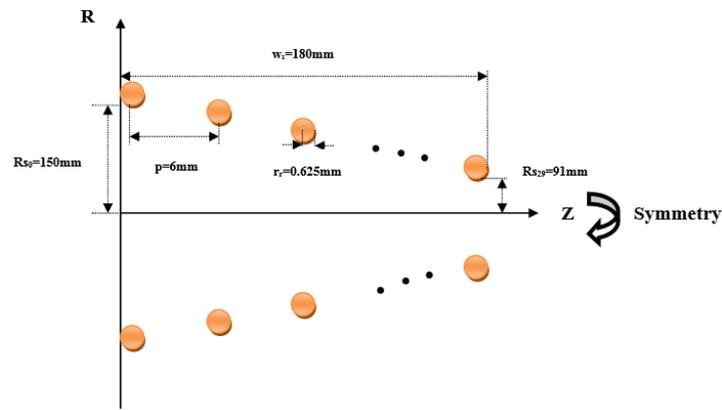
Figure 2.6 2D Filamentary representation of secondary winding

Based on the axial and radial dimensions, the place of every ring in the axes (Z, R) can be defined as:

$$Z_i^s = i \cdot p + r_r \tag{2.40}$$

$$R_i^s = Rs_0 - i \cdot p \cdot \frac{Rs_0 - Rs_{29}}{w_s} \tag{2.41}$$

The self-inductance of every ring is given by [2.26] [2.27]:

$$L_i^s(R_i^s, r_r) = \mu_0 R_i^s \left[\ln\left(\frac{8\pi R_i^s}{r_r}\right) - 2.45 \right] \tag{2.42}$$

where μ_0 is the permeability of free space.

Similarly, the mutual inductance between two rings can be calculated from [2.26] [2.27]:

$$M_{i,j}^S = \frac{2\mu_0 \sqrt{R_i^S \cdot R_j^S}}{k}\left[\left(1 - \frac{k^2}{2}\right)K(k) - E(k)\right] \tag{2.43}$$

where

$$k = \sqrt{\frac{4 \cdot R_i^S \cdot R_j^S}{\left(R_i^S + R_j^S\right)^2 + \left(Z_i^S - Z_j^S\right)^2}} \tag{2.44}$$

Based on the above equations for the secondary winding and equations (2.37) (2.38), the self-inductance of the secondary winding can be calculated from:

$$L_S = \frac{\sum_{i=0}^{29}\sum_{j=0}^{29} M_{i,j} I_i I_j}{2\left(\sum_{i=0}^{29} I_i\right)^2} \tag{2.45}$$

and the result obtained is $L_S = 177\ \mu H$.

2.3.1.4. Mutual inductance between primary and secondary windings

The model used for calculating the mutual inductance M between the primary and secondary windings is shown in Figure 2.7.
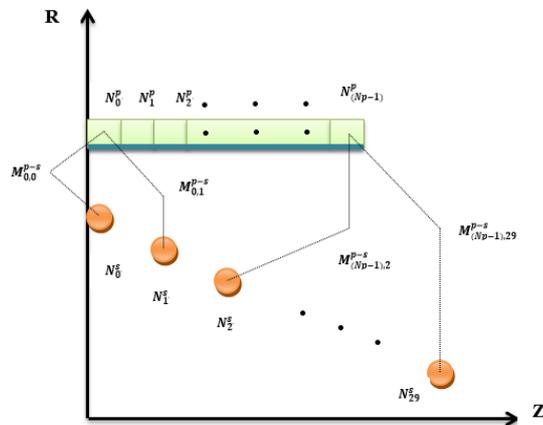
Figure 2.7 2D Filamentary representation of mutual inductance

The mutual inductance between the thin tape and the rings can be calculated using formula [2.26] [2.27] from:

$$M_{i,j}^{p-s} = \frac{2\mu_0 \sqrt{R_i^p \cdot R_j^s}}{k}\left[\left(1 - \frac{k^2}{2}\right)K(k) - E(k)\right] \tag{2.46}$$

where

$$k = \sqrt{\frac{4 \cdot R_i^p \cdot R_j^s}{\left(R_i^p + R_j^s\right)^2 + \left(z_i^p - z_j^s\right)^2}} \tag{2.47}$$

The mutual inductance calculated for the experimental Tesla transformer from equation (2.46) is $M = 4.86\,\mu H$, resulting in a coupling coefficient $k = \frac{M}{\sqrt{L_p \cdot L_s}} = 0.6$, which is precisely the value required by the dual resonant conditions. The ideal voltage multiplication factor $k_v = \sqrt{\frac{L_s}{L_p}} = 22$.

2.3.2. Electrostatic modelling

2.3.2.1. Electric field distribution

The electrical field distribution of the secondary winding can be determined using an electrostatic solver such as Maxwell SV (produced by ANSYS [2.28]), which can provide the distribution of the electric field strength and the Maxwell matrix related to the capacitance network. The matrix can then be used to calculate the equivalent capacitance of the secondary winding by adopting a Stray Capacitance Modelling Method. The distribution of electric field strength is used to analyse the possibility of electrical breakdown.

The simulation model in Maxwell SV is shown as in Figure 2.8, with the secondary winding modelled by a helical coil with 30 coaxial rings. The distance between any two rings and the angle of the secondary winding are both equal to those of the actual coil. The yellow sheet represents the primary winding, with the left edge set as an axisymmetric boundary and the background is transformer oil.
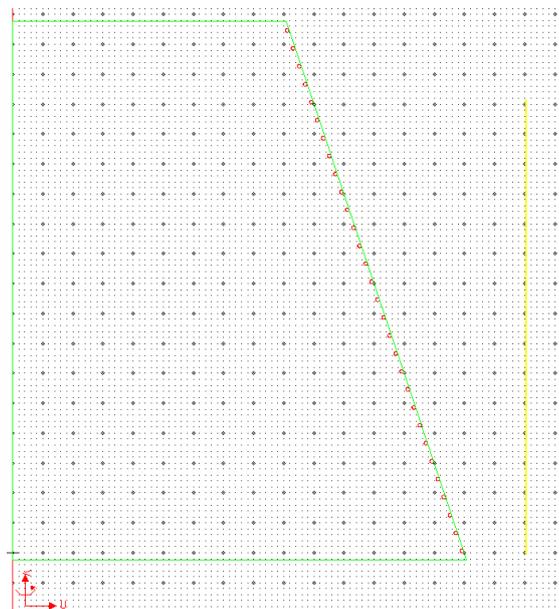
Figure 2.8 Maxwell model of Tesla transformer
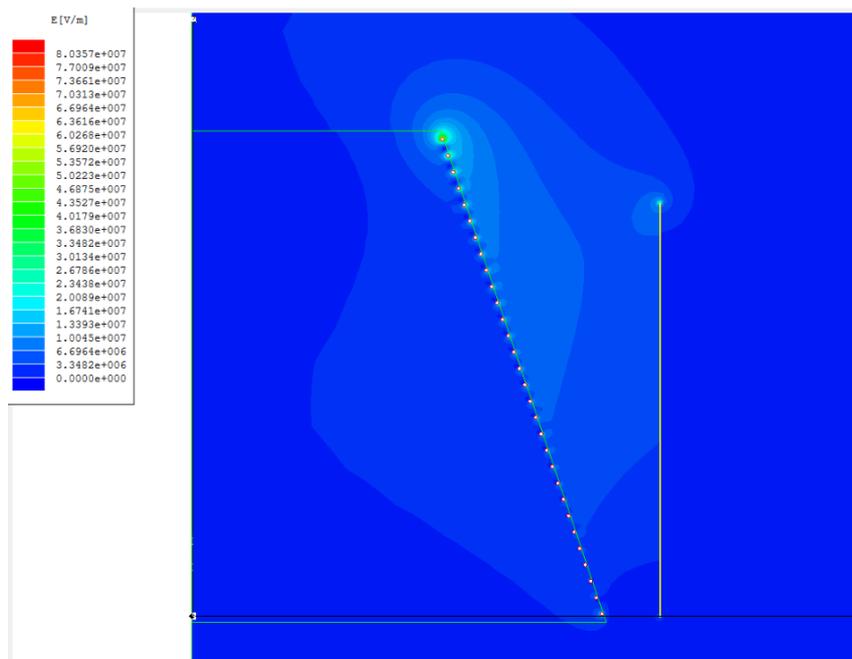
Figure 2.9 2D electric field distribution inside Tesla transformer for a secondary voltage of 600 kV

The distribution of electric field strength can be clearly observed in the simulation of Figure 2.9, which shows that the strongest part is adjacent to the high voltage ring. The pulse breakdown electric field E_b of transformer oil is determined using a J.C.Martin formula [2.29] [2.30]:

$$E_b = 480 \cdot t^{-\frac{1}{3}} A^{-0.067} \frac{kV}{cm} = 1.748 \times 10^8 V/m \tag{2.48}$$

where t represents the time in microseconds for which the instantaneous voltage exceeds 60% of the peak applied voltage and A is the surface area of the electrode.

2.3.2.2. Stray capacitance of Tesla transformer

Figure 2.10 Maxwell matrix

The Maxwell matrix of Figure 2.10 is the capacitance network for the Tesla transformer and includes all the secondary winding elements. The stray capacitance of a coil consists of the turn to turn and turn to earth capacitances can all be calculated using the Maxwell matrix.

The analysis and the corresponding technique are as follows. For a system of N conductors, with one chosen as an 'earth' or common reference, it can be easily be

shown that there are N+1 equations for the charges $Q_{i,i}$=1…N on the remaining conductors. In compact matrix form this can be written [2.31]

$$Q_i = \sum_{j=1}^{N} B_{i,j} V_j^0 \tag{2.49}$$

where V_j^0 is the potential of conductor j relative to conductor 0, chosen as a common reference, and the $B_{i,j}$ terms are the Maxwell coefficients, and are termed the coefficients of self-capacitance C_i:

$$C_i = B_{i,i} \tag{2.50}$$

which is defined as the charge to potential ratio on the ith conductor when all the other conductors are earthed. Since the potential has the same sign as the charge, the $B_{i,i}$ coefficients are always positive. $B_{i,j}$ are termed the coefficients of induction and represent the partial capacitance or the negative of the mutual capacitance $C_{i,j}$ between conductors i and j. Thus,

$$C_{i,j} = -B_{i,j} = -B_{j,i} \tag{2.51}$$

and are calculated as the ratio of the induced charge on the ith conductor to the potential of the jth conductor, when all other conductors are earthed. The induced charge is always opposite in sign to the inducing charge, so that all $B_{i,j}$ are either negative or zero. Finally, the partial capacitance $C_{0,i}$ of the common reference conductor 0 with any other conductors i can be expressed as:

$$C_{0,i} = \sum_{k=1}^{N} B_{i,k} \tag{2.52}$$

Figure 2.11 shows the way in which the helical secondary winding capacitances can be modelled into a simple lumped form, by considering the coil as an assembly of N parallel coaxial identical rings having the equivalent complex lumped network. [2.31]
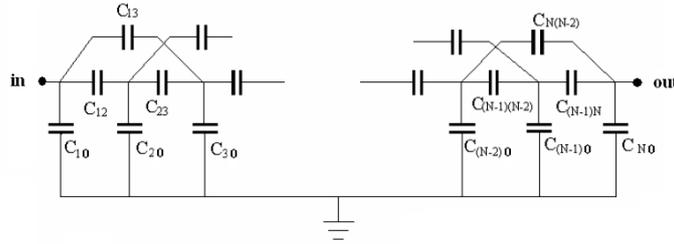
Figure 2.11 Secondary winding capacitance network (N=29) [2.31]

The earth is considered as the 0 conductor. Using the matrix in figure 2.10, Equation (2.49) can be re-written as [2.31]:

$$
\begin{bmatrix} Q^x \\ Q^y \end{bmatrix} = \begin{bmatrix} D^{xx} & D^{xy} \\ D^{yx} & D^{yy} \end{bmatrix} \cdot \begin{bmatrix} V^x \\ V^y \end{bmatrix}
\tag{2.53}
$$

where

$$
Q^x = \begin{bmatrix} Q_1 \\ Q_N \end{bmatrix} ; Q^y = \begin{bmatrix} Q_2 \\ \vdots \\ Q_{N-1} \end{bmatrix} ; V^x = \begin{bmatrix} V_1 \\ V_N \end{bmatrix} ; V^y = \begin{bmatrix} V_2 \\ \vdots \\ V_{N-1} \end{bmatrix}
\tag{2.54}
$$

and

$$
D^{xx} = \begin{bmatrix} B_{1,1} & B_{1,N} \\ B_{N,1} & B_{N,N} \end{bmatrix} ; D^{xy} = \begin{bmatrix} B_{1,2} & \cdots & B_{1,N-1} \\ B_{N,2} & \cdots & B_{N,N-1} \end{bmatrix}
$$

$$
D^{yx} = \begin{bmatrix} B_{2,1} & B_{2,N} \\ \vdots & \vdots \\ B_{N-1,1} & B_{N-1,N} \end{bmatrix}
$$

$$
D^{yy} = \begin{bmatrix} B_{2,2} & \cdots & B_{2,N-1} \\ \vdots & \ddots & \vdots \\ B_{N-1,2} & \cdots & B_{N-1,N-1} \end{bmatrix}
\tag{2.55}
$$

The aim of the technique is to reduce the system of N capacitances in Figure 2.11, to a system which has only an equivalent series capacitance with two parallel capacitances to earth, one at the system input and one at its output, as in Figure 2.12.
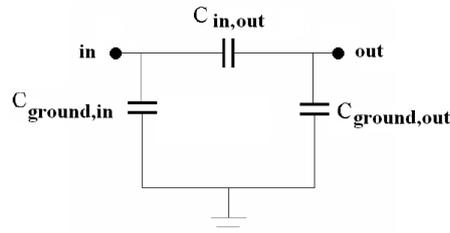
Figure 2.12 Equivalent capacitances [2.31]

To perform this transformation, all the capacitances from 2 to N must be removed from the circuit, by ensuring that they are uncharged. This condition can be written in compact matrix form as $Q^y = 0$, and introducing this into equation (2.54) enables firstly V^y to be found from equations [2.31] [2.32] as:

$$V^y = -(D^{yy})^{-1}D^{yx}V^x \tag{2.56}$$

and by re-introducing V^y into equation (2.54), the matrix Q^x is found as:

$$Q^x = (D^{xx} - D^{xy}(D^{yy})^{-1}D^{yx})V^x = B^xV^x \tag{2.57}$$

where B^x is a four-element matrix defined as:

$$B^x = D^{xx} - D^{xy}(D^{yy})^{-1}D^{yx} \tag{2.58}$$

which contains the Maxwell coefficients for the new simpler system of capacitances shown in Figure 2.12. The new equivalent series capacitance placed between the system input and output is calculated using equation (2.51) as:

$$C_{in,out} = -B^x_{1,2} = -B^x_{2,1} \tag{2.59}$$

and the new partial capacitances to earth, at the input and output terminals, are obtained using equation (2.52) as:

$$C_{ground,in} = B_{1,1}^x + B_{1,2}^x \qquad\qquad (2.60)$$

$$C_{ground,out} = B_{2,1}^x + B_{2,2}^x \qquad\qquad (2.61)$$

Applying this technique to the matrix in Figure 10, yields: $C_{in,out} = 2.05\ pF$, $C_{ground,in} = 12.87\ pF$, $C_{ground,out} = 32.97\ pF$ and the corresponding simplified lumped circuit representation of the secondary winding is shown in Figure 2.13. In the practical arrangement the input is directly connected to the bank ground and therefore all three capacitances are in parallel with the two Blumlein PFL capacitances.
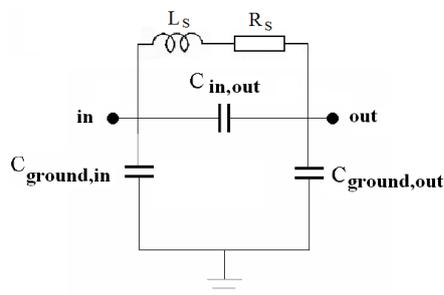
Figure 2.13 Lumped representation of the secondary winding circuit [2.31]

2.4. References

[2.1] S T Pai and Qi Zhang (1995). *Introduction to high power pulse technology*. Singapore: World Scientific Publishing Co. Pre. Ltd..

[2.2] W. J. Sarjeant and R. E. Dollinger (1989). *High-Power Electronics*. USA: TAB BOOKS Inc..

[2.3] N. Tesla, manuscript edited by Aleksandar Marincic (1978). *Colorado Springs Notes, 1899-1900*. Nolit Press.

[2.4] N. Tesla (23 June 1891). *System of electric lighting*. Patent no. 454622.

[2.5] N. Tesla (1 December 1914). *Apparatus for transmitting electrical energy*. Patent no. 1119732.

[2.6] Marco Denicolai (May 2001). *Tesla Transformer for Experimentation and Research*. Helsinki University of Technology: Licentiate Thesis.

[2.7] David Finkelstein, Philip Goldberg and Joshua Shuchatowitz. (1966). High Voltage Impulse System. *Review of Scientific Instruments*. 37 (2), pp159-162.

[2.8] F. M. Bieniosek. (1990). Triple resonance pulse transformer circuit. *Review of Scientific Instruments*. 61 (6), pp1717-1719.

[2.9] G. A. Mesyats, V. G. Shpak, M. I. Yalandin, and S. A. Shunailov. (1991). Compact High-Current Repetitive Pulse Accelerators. *Proc. 8th IEEE International Pulsed Power Conference*. San Diego, California, USA. pp73-77.

[2.10] Yu.A.Aadreev, Yu.I.Buyanov, A.M.Efrcmov, V.I.Koshelev, B.M.Kovalchuk, K.N.Sukhushin, V.A.Vizir, V.B.Zorin (1997). High power ultrawideband electromagnetic radiation generator. *Proc. 11th IEEE International Pulsed Power Conference*. Baltimore, Maryland, USA. pp730-735.

[2.11] Johnelle L. Korioth, Richard P. Copeland, David W. Scholfield (1999). A novel super low inductance primary ring utilized in a pulsed dual resonant tuned

transformer. *Proc. 12th IEEE International Pulsed Power Conference*. Monterey, California, USA. pp811-814.

[2.12] Marco Denicolai. (2002). Optimal performance for Tesla transformers.*Review of Scientific Instruments*. 73 (9), pp3332-3336.

[2.13] F. E. Terman (1943). *Radio Engineers' Handbook*. New York: McGraw-Hill.

[2.14] W. R. Smythe (1950). *Static and Dynamic Electricity*. New York: McGraw-Hill.

[2.15] Paul W.Smith (2002). *Transient Electronics Pulsed Circuit Technology*. London: John Wiley & Sons Ltd.

[2.16] B. T. Phung, T. R. Blackburn, R. Sheehy and R. E. James (1991). Tesla transformer design and application in insulator testing. *Proc. 7th International Symposium on High Voltage Engineering*. Dresden, Germany. pp133-136.

[2.17] D. F. Rankin, B. M. Novac, I. R. Smith and M. Hubbard (2006). Complex multiphysical modelling of pulsed ultrahigh magnetic field systems. *Proc. 2nd European Pulsed Power Symposium*. Hamburg, Germany. pp212-216.

[2.18] B. M. Novac, I. R. Smith, M. C. Enache. (2000). Accurate modelling of the proximity effect in helical flux compression generators. *IEEE Transactions on Plasma Science*. 28 (5), pp1353-1355.

[2.19] B. M. Novac, I. R. Smith, M. C. Enache and H. R. Stewardson. (1997). Simple 2D model for helical flux-compression generators. *Laser and Particle Beams*. 15 (3), pp379-395.

[2.20] K. Gregory, I. R. Smith, V. V. Vadher and M. J. Edwards. (1995). Experimental validation of a capacitor discharge induction launcher model. *IEEE Transactions Magnetics*. 31 (1), pp599-603.

[2.21] B. M. Novac, I. R. Smith, M. C. Enache and P. Senior. (2002). Studies of a very high efficiency electromagnetic launcher. *Journal of Physics D: Applied Physics*. 35, pp1447-1457.

[2.22] B. M. Novac, I. R. Smith and M. Hubbard. (2004). 2D modelling of electromagnetic flux-compression in θ-Pinch Geometry. *IEEE Transactions on Plasma Science*. 32 (5), pp1896-1901.

[2.23] B. M. Novac, I. R. Smith, P. E. Jarvis, and C. J. Abbott. (2003). Accelerating Conductors by Electromagnetic Action Through Metallic Shields. *IEEE Transactions Magnetics*. 39 (1), pp305-309.

[2.24] J. Luo, B. M. Novac, I. R. Smith and J. Brown. (2005). Fast and accurate two-dimensional modelling of high-current, high-voltage air-cored transformers. *Journal of Physics D: Applied Physics*. 38, pp955-963.

[2.25] Noboru Miura, Koichi Nakao. (1990). Computer analysis of megagauss field generation by condenser bank discharge. *Japanese journal of applied physics*. 29 (8), pp1580-1599.

[2.26] Frederick W. Grover (1973). *Inductance Calculations: Working formulas and Tables*. 2nd ed. New York: Dover Publications, Inc.

[2.27] Jing Luo (2007). *Novel insulation techniques for high-voltage pulse transformers.* Loughborough University: Ph.D. Thesis.

[2.28] http://www.ansys.com/Products/Electronics/ANSYS+Maxwell. Last accessed 29th November 2015.

[2.29] H. Bluhm (2006). Pulsed Power Systems: Principle and Applications. Germany: Springer.

[2.30] T.H.Martin, A.H.Guenther and M.Kristiansen (1996). *J.C.Martin on Pulsed Power*. New York: Plenum Press.

[2.31] Qin Yu and Thomas W. Holmes. (2001). A Study on Stray Capacitance Modeling of Inductors by Using the Finite Element Method. *IEEE Transactions on Electromagnetic Compatibility*. 43 (1), pp88-93.

[2.32] Warren B. Boast (1964). *Vector fields: A vector foundation of electric and magnetic fields*. Harper & Row publishers.

3. Blumlein pulse forming line

3.1. Fundamentals of Blumlein pulse forming line

3.1.1. Introduction of Blumlein pulse forming line

In any high power pulsed system, the transmission line is one of the basic elements and can serve several important functions. It can produce very fast rise-time pulses, with the pulse width determined by the length of the line, or it can transmit a large amount of pulsed power. With proper switching, transmission lines can be used to re-shape the incoming pulse, with the pulse width determined by the length of the transmission line. When used for this purpose, they are referred to as pulse forming lines (PFLs). On the basis of their structure, they can be classified as simple transmission lines, double transmission lines (Blumlein lines), multiple (stacked) transmission lines or magnetically insulated transmission lines (MITL). [3.1]

In the present research, a Blumelin PFL was employed to shape the output pulse of the Tesla transformer, since it is adequate for use in generating ultra-short pulse with a fast rise time. The Blumlein line is a typical double-line, which may be conceptually considered as two simple transmission lines connected in such a way that they are charged in a parallel configuration and subsequently discharged in series [3.2]. With proper termination, it can, in principle, produce an output voltage twice as high as that of a simple transmission line. A cylindrical PFL was constructed on the basis that it would be compact, easy to operate and relatively more reliable.

In cylindrical form, the basic structure consists mainly of three coaxial cylinders of different radii arranged in the way shown in Figure 3.1. The space between the cylinders is normally filled with a liquid dielectric medium, such as oil or deionised water, for most high power pulse applications. Between the middle and inner cylinders a switch (S) is connected to control the hold-off voltage of the line. The radii of the three cylinders are chosen so that the conditions of keeping the characteristic impedance uniform along the entire line and maintenance of the required voltage are satisfied. The load is commonly connected between the inner and outer cylinders and the high voltage input is fed in via the middle cylinder as indicated in the figure.
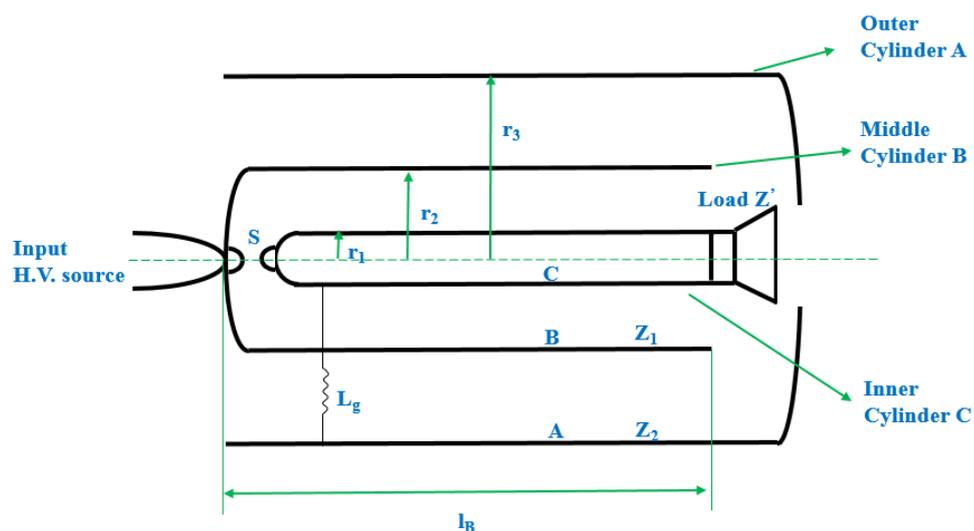
Figure 3.1 Basic structure of a cylindrical Blumlein line with a matched load where A=outer cylinder of radius r_3 ,B=middle cylinder of radius r_2 ,C=inner cylinder of radius r_1 ,S=H.V. switch, Z_1,Z_2=characteristic impedances of the inner and outer lines,Z'=load impedance,L_g=grounding inductor.

The Blumlein PFL consists of two coaxial transmission lines: one formed by the middle-inner combination and the other by the middle-outer combination. An important feature of any Blumlein is that its cross sectional configuration and the separation between the conductors must also remain constant along the length of the line. If a dielectric is inserted between the lines the dielectric constant must remain

constant throughout the length of the line. The electrical parameters of the coaxial transmission line are thus uniformly distributed along its length. The parameters per unit length for a coaxial line are [3.3]:

$$C = \frac{2\pi\epsilon_r}{\ln\left(\frac{Rout}{Rin}\right)} \tag{3.01}$$

$$L = \frac{\mu_r \ln\left(\frac{Rout}{Rin}\right)}{2\pi} \tag{3.02}$$

and the characteristic impedance of the line is

$$Z_0 = 60\sqrt{\frac{\mu_r}{\epsilon_r}}\ln\left(\frac{Rout}{Rin}\right) \tag{3.03}$$

where ϵ_r is the relative permittivity of the dielectric material between the conductors, $Rout, Rin$ are the outer and inner radii of the coaxial line and μ_r is the relative permeability of the dielectric material between the conductors. [3.3]

3.1.2. Circuit Analysis

In order to facilitate the analysis, Figure 3.2 shows the equivalent circuit of the Blumlein line. A length l_B of the line of impedance Z_1 and Z_2 is charged to a potential V by the power source. Analysis of the behaviour can readily be described using a series of voltage time diagrams, which show the potential on the two lines during the pulse forming action. For purposes of illustration, Figure 3.2 shows the simplest situation, where the impedances of the load and line are matched:

$$Z_1 = Z_2, \ Z' = Z_1 + Z_2 \tag{3.04}$$
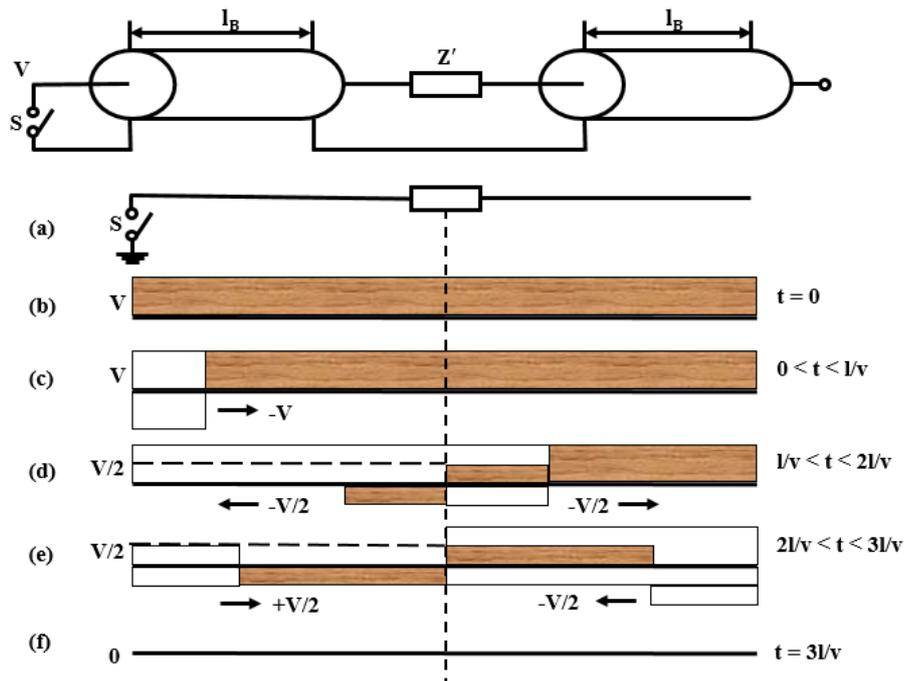
Figure 3.2 Potential distribution on the two lines at various times after closure of switch

➢ On closure of the switch S, which initiates pulse forming action, the end of line 1 next to the switch is effectively shorted. The voltage on the load rises from zero to a value determined by the initial charge voltage V. The reflection coefficient at this end of line 1 is -1, simultaneously a step voltage –V propagates towards the load and as it propagates it discharges the line.

➢ At the open end of line 2 the reflection coefficient is +1. At the junction of line 1 and the load the reflection coefficient can be calculated by observating that line 1 is effectively loaded by a combination of the load in series with the impedance of line 2. For correct operation of the Blumlein pulse forming line, the load impedance must be equal to twice the characteristic impedance of the each line. Thus line 1 is loaded by an impedance of $Z_1 + Z'$ and the reflection coefficient at the load is

$$\rho = \frac{Z_1 + Z' - Z_1}{Z_1 + Z' + Z_1} = \frac{1}{2} \tag{3.05}$$

57

When the first reflection reaches the load, after a transit time delay $\delta = l/v$, the step is partly transmitted and partly reflected with a reflection coefficient of +1/2 as shown by equation(3.05). Thus a step of –V/2 is launched back into line 1 propagating towards the switch. The transmitted step will have an amplitude equal to the sum of the incident step $V_+ = -V$ and the reflected step $V_- = -V/2$, i.e. $-3V/2$. The diagram given in Figure 3.3 helps to explain how this step is divided between the load and line 2. By consideration of what amounts to a simple voltage divider it can be shown that a step of amplitude $-V/2$ is launched into line 2 and that the potential across the load is V. [3.4]
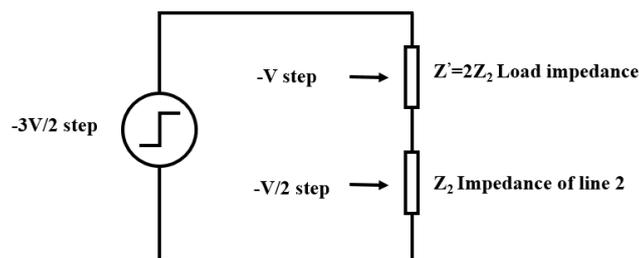
Figure 3.3 Division of the voltage step between line 2 and the load [3.4]

➢ The second step propagates along line 2, discharging the line to a potential of $V/2$, and is reflected at the open end of this line with a coefficient of +1 to fully discharge the line as a $-V/2$ step propagates back to the load. The step in line 1 first charges the line to a potential of $-V/2$ and then reflects it with a coefficient of -1 so that it also discharges line 1 as it propagates back to the load. When the two steps arrive at the load they effectively cancel each other and the pulse on the load terminates (Figure 3.4). The pulse duration is clearly equal to

$$T = 3\frac{l}{v} - \frac{l}{v} = 2\frac{l}{v} = 2\tau \tag{3.06}$$

If the impedance of the load and the lines are not matched, further reflections of the propagating step occur at the load and the resulting output pulse has a more complicated shape, rather than the single rectangular pulse shown in Figure 3.4.
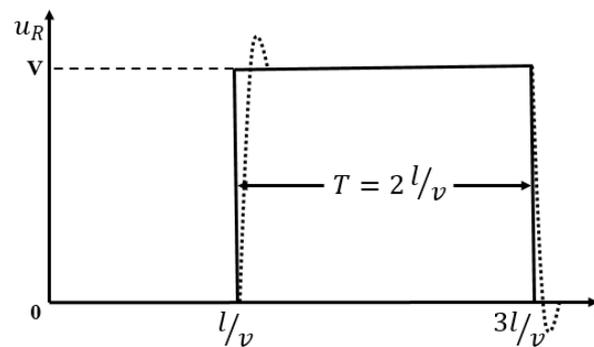
Figure 3.4 Pulse on the load

3.2. Design consideration and procedure

To rate the performance of a Blumlein line, it is usual to refer to certain parameters such as the output voltage, current, the transfer efficiencies of the voltage, energy and power etc. Ideally a Blumlein line should be designed to have the following properties: high output voltage and current, high transfer efficiencies for both energy and power, high reliability and compact in size.

3.2.1. Design consideration

The PFL constructed was required to meet the specification that

Output Voltage=500 kV

Load Impedance=30 Ω

Pulse Duration=10 ns

In order to get adequate results for most aspects, it is essential to have a matched line, and the following discussion is based on a properly matched Blumlein line. The effective length l_B can be determined from equation (3.06) as

$$l_B = \frac{cT}{2\sqrt{\varepsilon_r}}$$

(3.07)

where c is the velocity of light, ε_r is the relative permittivity, and T is the pulse duration.

From the specification given above, the characteristic impedance of each line should be 15Ω.

$$Z_i = \frac{60}{\sqrt{\varepsilon_r}} \ln\left(\frac{r_{i+1}}{r_i}\right)$$

(3.08)

where r_i and r_{i+1} are the inner and outer radii respectively, Z_i is the characteristic impedance (i=1,2) and ε_r is the relative permittivity of the dielectric. The capacitance of each coaxial line is

$$C_i = \frac{2\pi\varepsilon_0\varepsilon_r l_B}{\ln\left(\frac{r_{i+1}}{r_i}\right)}$$

(3.09)

where the permittivity of vacuum $\varepsilon_0 = 8.854 \times 10^{-12}\ F/m$.

3.2.2. Dielectric

A dielectric insulator is a material that can provide a high resistance to the passage of an electrical current. Liquid dielectrics are often used for the pulsed power applications, because of their mechanical or structural compatibility with the high power pulse system, which is usually required to store a high density of electrical energy and to

wishstand high voltages. In principle, a large variety of liquids can be used as insulators in the high voltage environment, but for practical usage however only a small number of these is suitable. The most widely employed liquids in high power pulse applications are transformer oil and water. Table 3-1 shows the room temperature resistivity and dielectric constants of insulators considered in the present design.

Table 3-1 Room temperature resistivity and dielectric constant for dielectric

Material	$\rho \ (\Omega \cdot cm)$	Dielectric constant
Distilled water	$10^5 - 10^6$	80
Transformer oil	$10^{12} - 10^{15}$	2.25

Based on equations (3.07) (3.08) and table 3-1, the following parameters were calculated.

Table 3-2 Parameters in different dielectric

Material	$l_B(m)$	$\dfrac{r_3}{r_1}$
Distilled water	0.168	87.535
Transformer oil	1	2.117

Because the ratio of $\frac{r_3}{r_1}$ for water in table 3-2 is too high for manufacturing purposes, transformer oil was used as the dielectric. The design details are: inner electrode with an outer radius $r_1 = 104 \ mm$, intermediate electrode with an outer radius $r_2 = 152.5 \ mm$, outer electrode with an internal radius $r_3 = 222.25 \ mm$, both the intermediate and the inner electrode are steel cylinders with a wall thickness of $\sigma = 1.5 \ mm$. The calculated impedances and capacitances are: $Z_1 = 14.916 \ \Omega$, $Z_2 = 15.066 \ \Omega$, $C_1 = 335.7 \ pF$, $C_2 = 332.3 \ pF$.

3.2.3. Electrostatic modelling

The breakdown characteristics of oil under pulsed voltages have been studied extensively under various conditions. The breakdown electric field can be estimated using the Charlie Martin formula for oil under a HV impulse [3.5]:

$$E_b = 480 \times t^{-1/3} A^{-0.067} \, kV/cm \tag{3.10}$$

where t is the time in microseconds for which the instantaneous voltage exceeds 60% of the peak applied voltage and A is the surface area of the electrode in cm^2. Application of this formula, with $t \approx 0.4 \, \mu s$, to the outer surface of the inner electrode, for which $A \approx 6540 \, cm^2$, predicts there is a 50% chance of breakdown at an electric stress of $E_b \approx 360 \, kV/cm$.

Maxwell SV software [3.6] was used to highlight possible dangers arising from the existence of regions of high electric field in the Blumlein pulse forming line. The design of the three electrodes was tedious (Figure 3.5), mainly related to finding the optimum diameter and position of the electric grading ring attached to the inner HV electrode in respect to a recess in the outer surface of that electrode. The final geometry electrode (Figure 3.6) produced an electric field distribution with a peak electric field strength of $223 \, kV/cm$, for the Blumlein pulse forming line charged to $600 \, kV$, which represents a substantial reduction from the peak field of $443 \, kV/cm$ generated by the commonly used and simpler geometry of Figure 3.5.

(a)   **(b)**   **(c)**   **(d)**
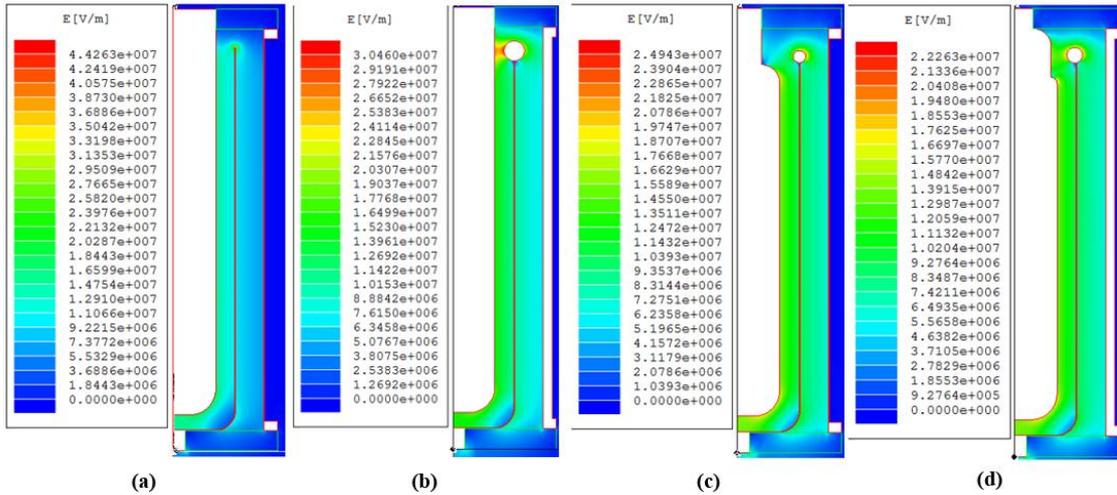
Figure 3.5 2D electric field distribution inside Blumlein pulse forming line at 600 kV (a) for the simplest design, the maximum field strength is 443 kV/cm. (b) for a much simpler design, the maximum field strength is 305 kV/cm. (c) for a better design, the maximum field strength is 250 kV/cm. (d) for the present design, the maximum field strength is 223 kV/cm.

(b)

(a)   **(c)**
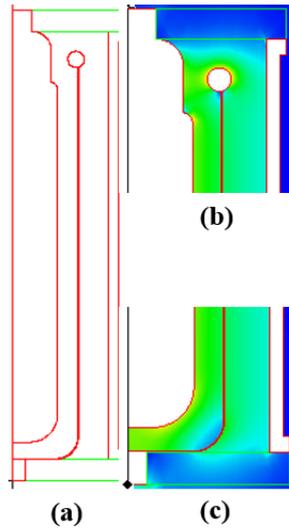
Figure 3.6 2D geometry of present design. (b) and (c) are details near the electric grading elements for the design.

If the maximum electric stress inside the present Blumlein pulse forming line as provided by the Maxwell software is compared with the breakdown value calculated using equation (3.10), the conclusion is that the oil is stressed up to 62% of the predicted breakdown value. The probability of failure PF can be more accurately predicted using the formula [3.7]:

$$PF = 1/2 \left(E_{max} / E_b \right)^{1/0.067} \tag{3.11}$$

63

where E_{max} is the maximum applied electric field in kV/cm. For $E_{max} \approx 223\ kV/cm$ the resulting value for $PF \approx 3.6 \times 10^{-4} \approx 1/2760$ and it can be interpreted that if the line is charged to 600 kV, a failure will statistically only occur inside the Blumlein pulse forming line only once in every 2760 shots.

The two capacitance of the Blumlein pulse forming line calculated before were also obtained using Maxwell SV software as $C_1 = 326.5\ pF$, $C_2 = 341.3\ pF$, resulting in an overall equivalent capacitance $C_{B-PFL} = 667.8\ pF$.

3.3. Overall configuration and manufacture
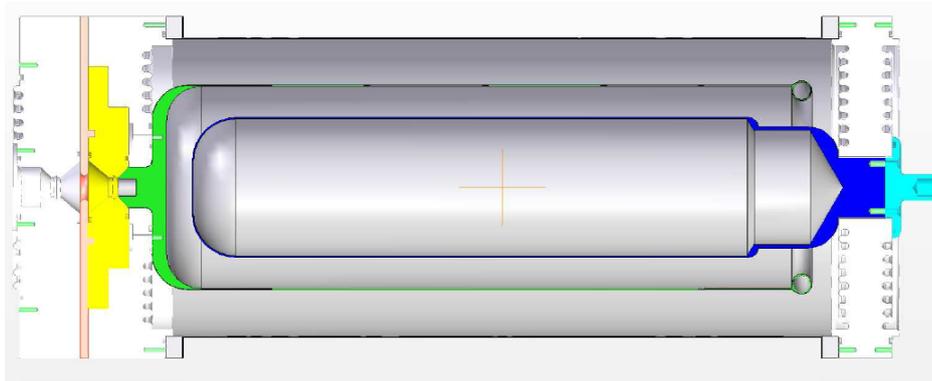
Figure 3.7 Structure of the cylindrical Blumlein
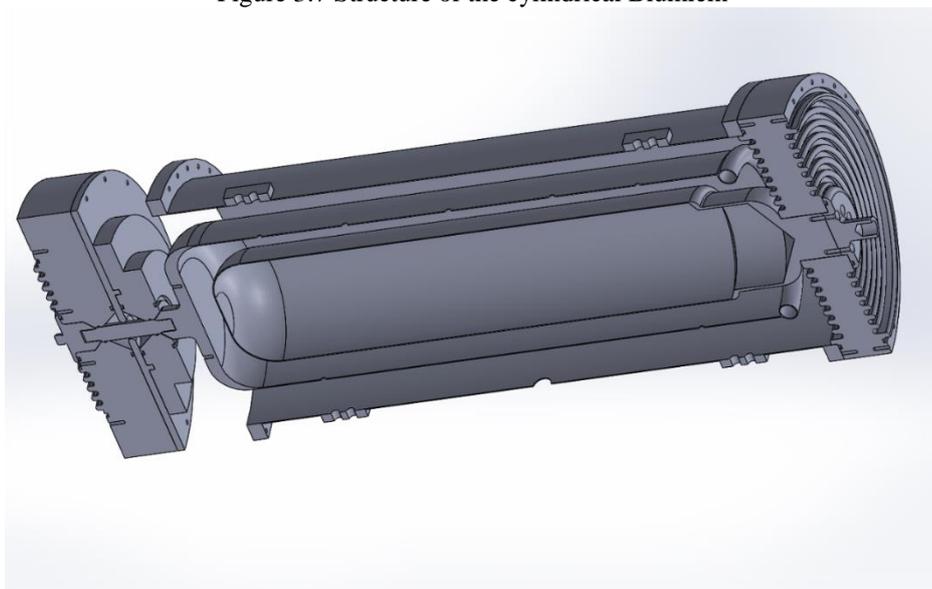
Figure 3.8 3D drawing of the Blumlein-PFL
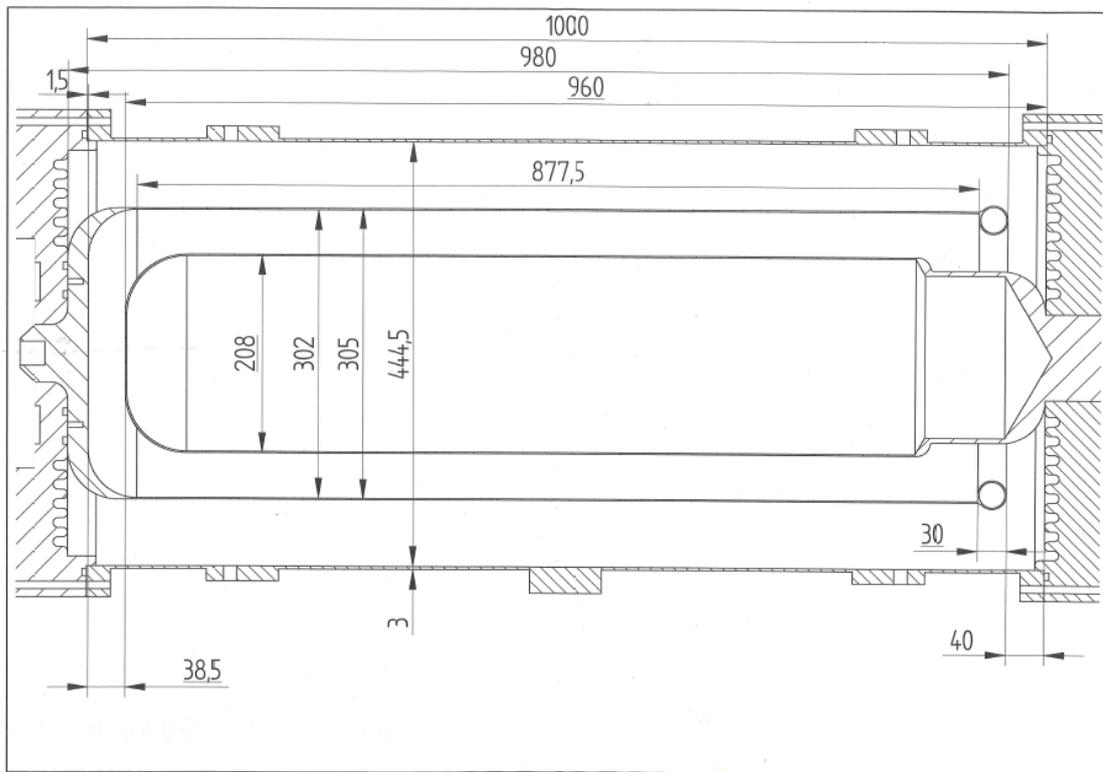
Figure 3.9 Dimensions of the Blumlein-PFL

Figures 3.7, 3.8, 3.9 present a 3D drawing of the Blumlein PFL using 3D computer aided design(CAD) solid modelling software Solid Edge [3.8].
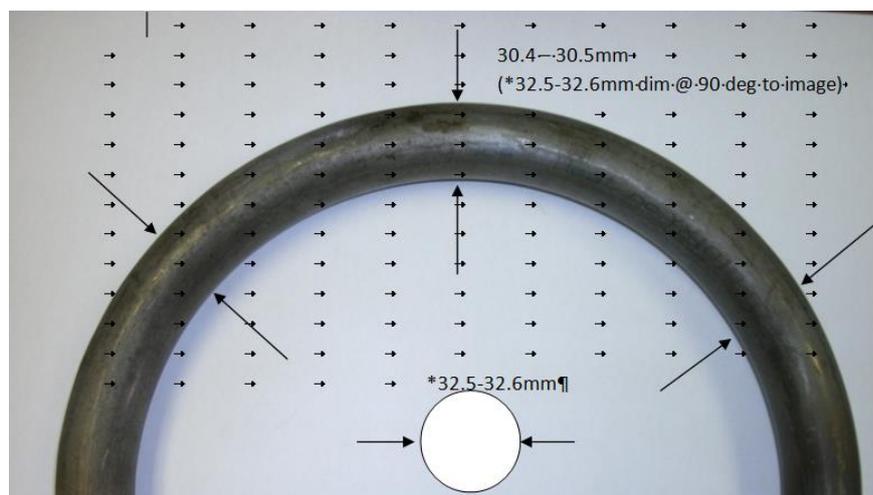
Figure 3.10 Blumlein pulse forming line intermediate electrode grading ring
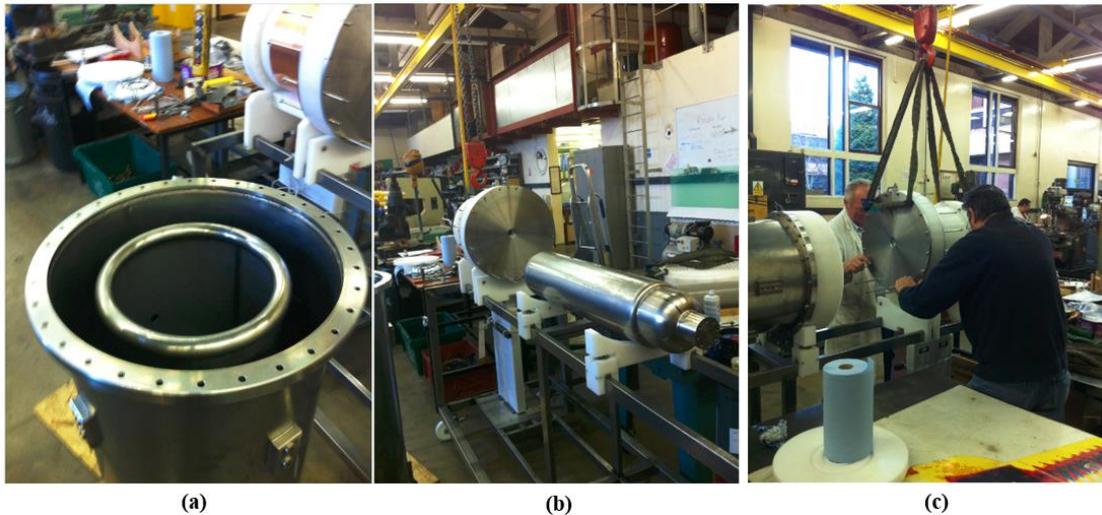
Figure 3.11 Aspects from manufacturing and assembly. (a) outer and intermediate electrodes partially assembled. (b) inner electrode ready for mounting. (c) attaching the Tesla to the Blumlein PFL.

Manufacture of a Blumlein pulse forming line 1 m long inner and intermediate electrodes is demanding, in particular the electrical grading ring attached to the intermediate electrode, which requires a precision better than 1 mm (Figure 3.10) that has to be maintained after welding to the electrode which needs special high-tech manufacture. Figure 3.11 shows various views when mounting the Blumlein PFL. Filling the cavity between the electrodes with oil is made under vacuum and is a tedious process, but after all bubbles were completely removed no breakdown issues have been encountered during continuous usage.

3.4. References

[3.1] S T Pai and Qi Zhang (1995). *Introduction to high power pulse technology*. Singapore: World Scientific Publishing Co. Pre. Ltd..

[3.2] A. D. Blumlein (1948). U.S. Patent 2465,840.

[3.3] H. Bluhm (2006). *Pulsed Power Systems: Principle and Applications*. Germany: Springer.

[3.4] Paul W.Smith (2002). *Transient Electronics Pulsed Circuit Technology*. London: John Wiley & Sons Ltd.

[3.5] T. H. Martin, A. Guenther, and M. Kristiansen, Eds. (1996). *J. C. Martin on Pulsed Power*. New York: Plenum Press.

[3.6] http://www.ansys.com/Products/Electronics/ANSYS+Maxwell. Last accessed 29th December 2015.

[3.7] K. E. Nielsen, H. A. Davis, E. O. Ballad, J. M. Elizondo, R. F. Gribble, B. T. McCuistian and W. M. Parsons (1999). Atlas Transmission Line Breakdown Analysis. *Proc. 12th IEEE International Pulsed Power Conference*. Monterey, California, USA. pp381-384.

[3.8] http://www.plm.automation.siemens.com/en_gb/products/solid-edge/. Last accessed 29th December 2015.

4. Bipolar former

4.1. Introduction of bipolar former

4.1.1. Motivation

It is straightforward to show that a monopolar voltage impulse is not well-suited to feed an antenna and that a bipolar signal will have a number of advantages as listed below [4.1]:

➢ better suited frequency spectrum i.e., the low frequency part of the monopolar pulse with frequencies less than 100 MHz and which cannot be radiated by a compact antenna, is greatly reduced in the bipolar pulse spectrum (Figure 4.1).

➢ reduced risks of insulation breakdown by flashover because:

    i.   the low-frequency components of the monopolar pulse, not matching the antenna characteristics, are reflected back to the generator; this unwanted phenomenon is absent in the case of a bipolar pulse.

    ii.   bipolar pulses have only a half voltage peak in respect to the peak voltage of the initial monopolar pulse but, very importantly, maintain the same peak-to-peak amplitude.

➢ the bipolar signal lacks any DC spectral components, thus improving the operator safety i.e., there is no risk of residual charges on the arms of an (not yet short-circuited) antenna.

➢ the technique used to generate a bipolar pulse, using a monopolar pulse as a driver, usually performs also a time compression of the driving signal thereby increasing the upper limits of its frequency spectrum. (Figure 4.1)

(a)   (b)
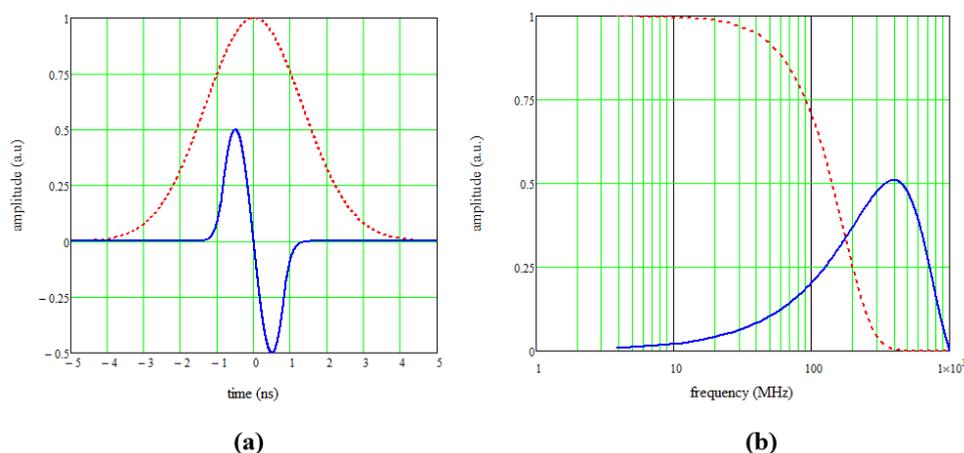
Figure 4.1 Comparison between a monopolar signal (dotted red line) and a bipolar signal (continuous blue line) in: (a) time domain and (b) frequency domain

4.1.2. Principle of bipolar former

There are three types of high power ultra-wideband bipolar pulse formers:

➢ High voltage bipolar pulse generator; a Vvedenski scheme[4.2] is widely used in which a forming long-cable line with a wave impedance φ is made with the screen ends joined together and the strand ends connected to the load R_l and the matching resistance R_m from one side and the second side, respectively. Commutator K switches between the common point of the screens and ground connection. Charge voltage V_0 is applied between the armour and ground. Such scheme allow a monopolar pulse to form on the unmatched load $R_l \neq \varphi$ at $R_m = 0$ and bipolar pulse when $R_m = 0$ and $R_l = \varphi$. The bipolar pulse presented in Figure 4.2 has an amplitude $V = \pm {V_0}/{2}$ and common length $\tau =$

$2l/v$ where l is the line length and v is the velocity of the wave propagation in a line. [4.3]

Figure 4.2 Vvedenski scheme and bipolar voltage pulse forming if $R_m = 0$ and $R_l = \varphi$ [4.3]

➤ Bipolar pulse former with chopping-peaking switch; In this scheme two simultaneously operating spark gaps are placed on opposites ends of a pulse forming line (PFL)[4.4]. To produce a bipolar pulse, the driver which has a suitable starting monopolar pulse is equipped with an additional unit that includes chopping and peaking high-pressure gas gaps. When both gaps operate simultaneously, a bipolar pulse is produced at the convert output whose peak-to-peak amplitude equals the doubled breakdown voltage of the peaking switch. The line is charged to a voltage of $-2V_0$ and switched at the output into a matched load. As a result, the uninverted portion of the pulse with amplitude equal to $-V_0$ and duration, t_{fl}, equal to the time the wave takes to execute one pass along the line is formed on the load. The opposite end of the line is short-circuited on operation of the second spark gap, providing the formation of the inverted portion of the pulse. This pulse portion arrives at the load with a delay of t_{fl}, and the same duration, and therefore its amplitude is V_0 [4.5][4.6]. The obvious requirements for this scheme are that the rise time of the unipolar pulse t_r should be shorter than t_{fl}, and that the switching time of the spark gap should be short

and have only a small spread around t_{fl}. In reality making $t_r \ll t_{fl}$ is difficult and if the switching time of the spark gaps are not sufficiently short, the amplitude of the output is less than $2V_0$.
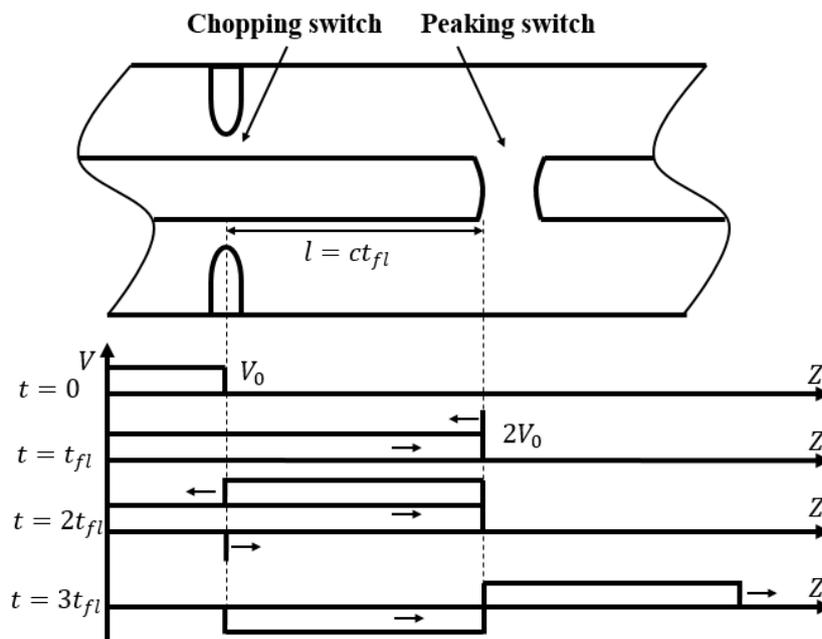
Figure 4.3 Bipolar pulse former with C-P switch and wave mode

➢ Blumlein bipolar pulse former; this has a design similar to a conventional Blumlein PFL, but with two closing switches installed at its input: one switch mounted in series for connection to the power source (usually not installed in a conventional Blumlein PFL) and the other mounted in parallel (part of a conventional Blumlein PFL) to discharge the unit (Figure 4.4). The electrical energy released by the Tesla-driven Blumlein generator charges the forming line T_0 to a voltage up to V_0. When the peaking switch trips, a $\frac{V_0}{2}$ pulse propagates by T_1 that is loaded at the end with lines T_2 and T_3 connected in series. The voltage wave passing through T_3 forms a V_0 half-wave of a bipolar pulse when it reaches the load. When the reflected wave reaches the input side of T_1 and the

71

wave passing into T_2 reaches its end, the earthing switch operates. Thus, the negative wave of the voltage removal propagates along line T_1, and the double negative wave reflected from the opened end propagates along T_2. These two waves reach the output of T_1 and the input of T_2 where they combine, and form at the load a negative bipolar pulse half-wave with an amplitude of $-V_0$. [4.7][4.8]
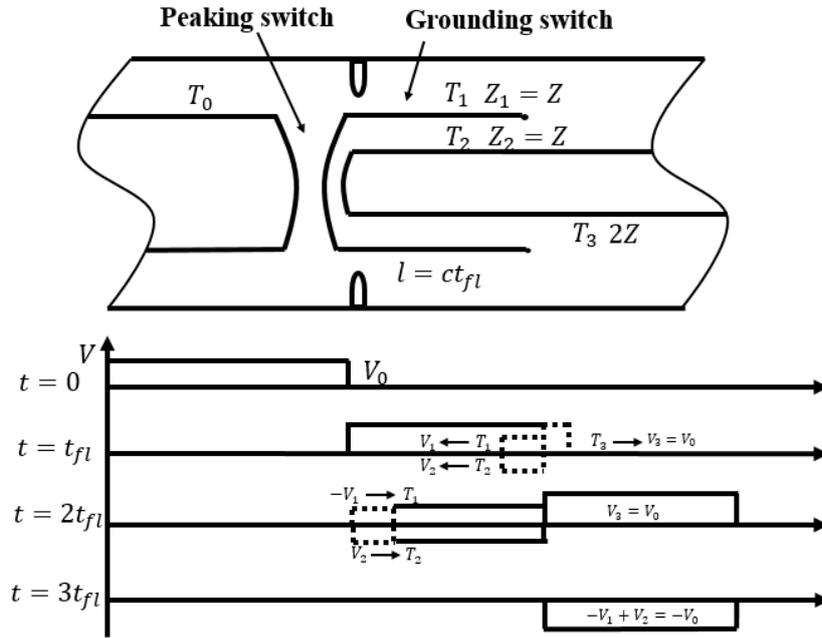
Figure 4.4 Blumlein bipolar pulse former

$$V_1 = \frac{2Z+Z_2-Z_1}{2Z+Z_2+Z_1}V_0 = {V_0}/{2} \tag{4.01}$$

$$V_2 = -\frac{2Z_2}{2Z+Z_2+Z_1}V_0 = -{V_0}/{2} \tag{4.02}$$

$$V_3 = \frac{2\times 2Z}{2Z+Z_2+Z_1}V_0 = V_0 \tag{4.03}$$

The circuit diagram of the bipolar pulse former using Orcad PSpice [4.9] is shown in Figure 4.5 and a simulation result in Figure 4.6.
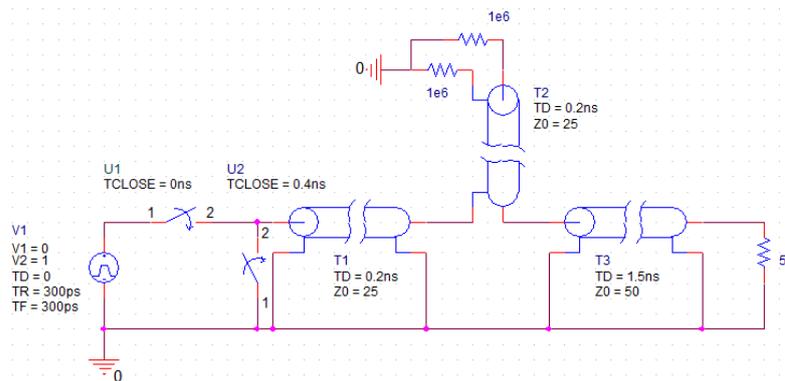
Figure 4.5 Circuit diagram of the bipolar pulse former
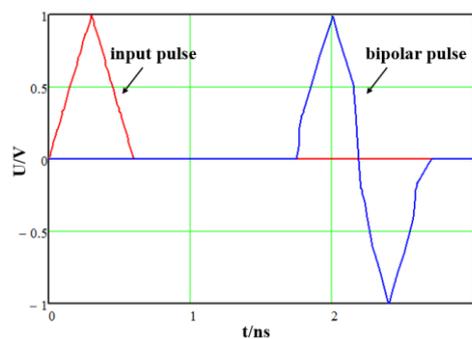
Figure 4.6 Calculated result of bipolar pulse former

The monopolar pulse is generated by the quasi-simultaneous operation of a peaking switch U1 and a grounding switch U2 (Figure 4.5). The Blumlein converts each edge at the input into a monopolar pulse in order to form a bipolar pulse at the output. The conditions that make the concept efficient are listed below [4.10]:

- the transit time through T1 and T2 should be precisely the same;

- the delay between the operation of U1 and U2 should be twice the transit time in T1;

- T2 should be terminated by a perfect short circuit;

- the junction of lines T1, T2 and T3 should respect the theoretical impedance mismatch.

4.2. Design details

4.2.1. Adapting the Blumlein to a bipolar former

To test the Tesla-Blumlein PFL generator it was operated with the high voltage series-connected 30 Ω resistive load. As PSpice [4.9] simulation results show (Figure 4.7), simply removing this resistor and attaching the bipolar former directly to the Blumlein PFL output or placing it in parallel to the output before attaching the bipolar former, are both unacceptable. The calculations are performed with the bipolar former operated only with its series-connecting switch (i.e., without a grounding switch). In the first case the generated voltage has a very high and negative undesirable pre-pulse, which may affect the proper functioning of the bipolar switches. In the second case the voltage signal has too low a positive (useful) amplitude. After a few calculations and preliminary trials, an acceptable compromising technical solution was found in the form of a 130 Ω resistance parallel-coupled to the Blumlein PFL output.
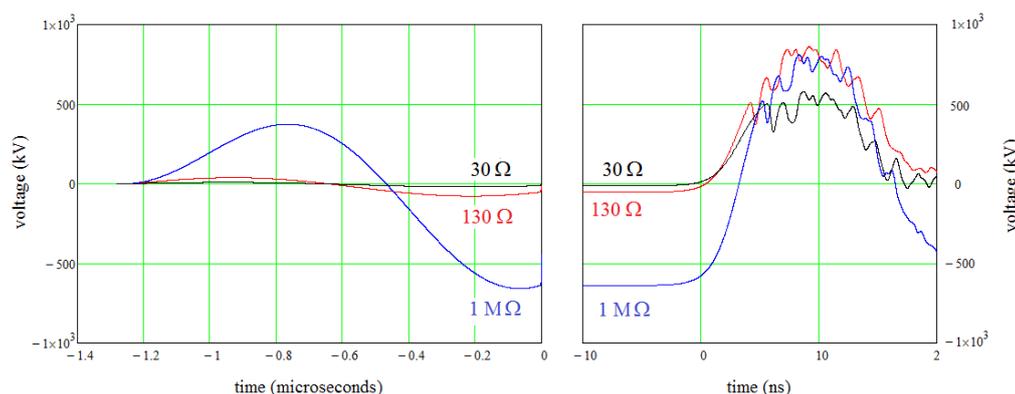
Figure 4.7 Results from the PSpice simulation of the Blumlein PFL output voltage (left: during unit charging; right: during discharging) for three different values of a parallel-attached resistor: 30 Ω, 130 Ω and 1 MΩ (open circuit). The time origin corresponds to the action of the closing switch that triggers the Blumlein PFL discharge.

The use of a series-connected 30 Ω resistive load needed to be changed because the stray capacitance and self-inductance of the resistive layers caused undesirable resonances and ringing. Aqueous-electrolyte resistors were used as load to adapt the Blumlein with the bipolar former. Low capacitance, good stability and easy maintenance can be realized by using aqueous-electrolyte resistors as resistive material. In contrast to solid-state resistors, the resistance is easily changed by adjustment of the electrolyte concentration. Copper electrodes are chosen to maintain the concentration of the $CuSO_4$ solution as well as to prevent erosion of the electrodes which will contaminate the solution. To minimize the chances of electrical flashover, the liquid of each resistor (liquid length 100 mm, diameter 15 mm) was kept inside a Teflon cylinder, with both the inside and outside of the wall having a ribbed geometry. In preparation of the $CuSO_4$ solution, deionized or distilled water was used to avoid the introduction of a significant quantity of the other ions present in tap water [4.11].

The final resistor was made from ten identical aqueous 1.3 kΩ resistors ($CuSO_4$ doped demineralized water) placed in a radial-symmetrical configuration. The resistance R of an aqueous-electrolyte resistor is determined by the resistivity ρ, the distance between parallel electrodes l, and the electrode area A [4.12]

$$R = {\rho l}/{A} \tag{4.04}$$

where $R = 1.300 \text{ k}\Omega$, $l = 100.0 \text{ mm}$, $A = \pi \cdot \left(\frac{d}{2}\right)^2$, $d = 15.00 \text{ mm}$ and the resistivity thus required is $\rho = 229.7 \ \Omega - \text{cm}$.

The resistivity is implicitly dependent upon the temperature T_s of the electrolyte and explicitly dependent upon the concentration C, here expressed in g/l. This latter dependence may be fitted to a power law [4.12]:

$$\rho = aC^b \tag{4.05}$$

where ρ is in $\Omega - cm$, $a = 1553$ and $b = -0.7465$ [4.13] are the fitting constants. The concentration obtained is $C = 12.94 \ g/l$, which can be confirmed by the resistivity curve of Figure 4.8. Reagent grade $CuSO_4$ was weighed, dissolved in a known volume of distilled water, and then degassed prior to use. Care was taken to avoid heating the solution and all measurements were taken at $T_s \approx 20°C$ [4.13]. The resistance was measured under continuous ac condition to make the resistance accurately by adjusting the volume of chemical or distilled water. The completed resistor is shown in Figure 4.9.
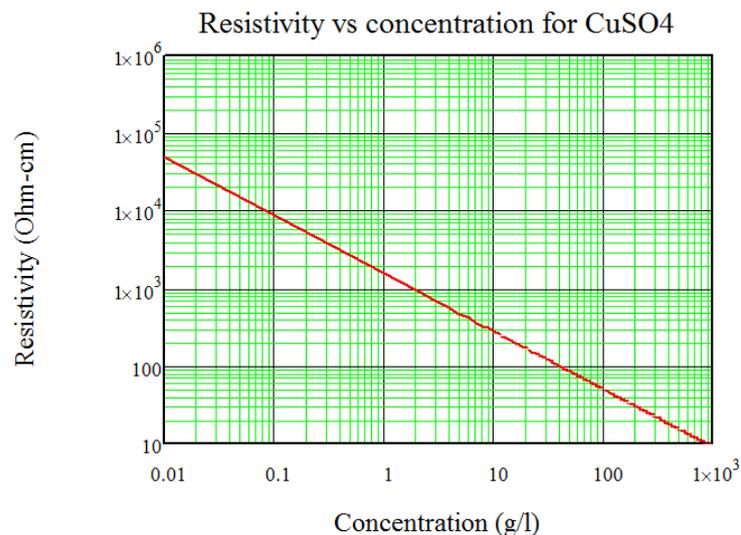
Figure 4.8 Resistivity for copper sulphate [4.13]
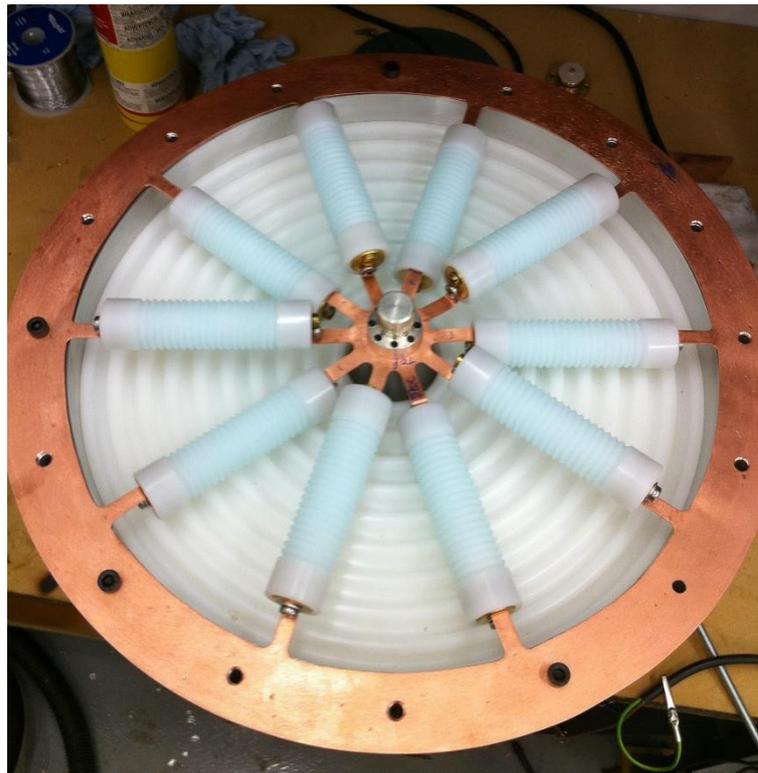
Figure 4.9 130 Ω resistor, made from ten identical aqueous 1.3 kΩ resistors radially mounted in parallel. When connected to the output of the Blumlein PFL generator, the empty space is filled with transformer oil.

4.2.2. Bipolar former design

The positive driving monopolar impulse is allowed to rise to a very high-voltage before the series-connected switch closes to attach the bipolar unit to the driving generator. At this moment, the electromagnetic energy that has been transferred from the driving source is capable of very rapidly pulse-charging the bipolar former, thus performing a pulse compression compared with the rise time of the driving monopolar pulse. During the charging time, a fraction of the fast positive voltage impulse is directly transferred to the load, with the bipolar former electrodes playing the role of a capable divider. The charging period ends with the second crowbar switch closure triggering discharge of the unit. As usual, the discharge of a Blumlein PFL generates a voltage impulse with a polarity opposite to the charging polarity i.e., the voltage generated on the load

during the discharge period is negative. To 'equilibrate' the bipolar voltage impulse i.e., for the amplitudes of two opposite polarity load voltage peaks to be close, the gap and geometry of both closing switches need to be carefully adjusted during what is usually a rather tedious process.

4.2.2.1. Bipolar former dimensions

The bipolar former is designed to feed the bipolar waveform to a normal 50 Ω antenna for radiation [4.14]. To achieve the best configuration, the dimensions of the matched line are discussed as follows. The Blumlein-based bipolar former has a coaxial structure.   An intermediate part is used both as an internal conductor of one line, and as an external conductor of the second one described as above. All metallic electrodes are made of aluminum and insulators of the bipolar former are made of ultra-high molecular weight polyethylene ($\varepsilon_r = 2.4$). The characteristic impedance of each line should be 25 Ω.

$$Z_i = \frac{60}{\sqrt{\varepsilon_r}} \ln \left(\frac{r_{i+1}}{r_i} \right) \tag{4.06}$$

where r_i and r_{i+1} are the inner and outer radii respectively, Z_i is the characteristic impedance (i=1,2), ε_r is the relative permittivity of the dielectric. The dimensions are then: inner electrode with a diameter $d_1 = 30.5 \, mm$, intermediate electrode with an internal diameter $d_2 = 58 \, mm$, outer diameter $d_2' = 68 \, mm$, outer electrode with an internal diameter $d_3 = 130 \, mm$.

Two versions of the bipolar former were manufactured, with lengths $l_{long} = 40 \, mm$.

4.2.2.2.   Closing switches

As already mentioned, a pair of closing switches is installed at the bipolar former input. The peaking switch was designed with two electrodes to increase the active surface, reduce the erosion, and minimize the field reinforcement [4.15][4.16]. The grounding switch is an annular grounding switch sharing a common electrode with the peaking switch. This set up allows the U. V. light of the first breakdown to pre-ionize the second gap and so to reduce the jitter. The geometry of the grounding switch was designed to ensure one simultaneous multi-channel discharge to help reduce the inductance of the sparks and to reach a good distribution of energy at the Blumlein input [4.17]. The high rising rate of the peaking switch allows an extreme over voltage of the field enhancement sites around the grounding switch [4.18]. An electrostatic solver Maxwell SV [4.19] was used to calculate both the electric field generated with 500 kV applied to the driver HV electrode (Figure 4.10) and to obtain the (pre-breakdown) capacitances of the two switches, for use in PSpice modelling. The capacitances obtained are: $C_{peaking} = 12.9\ pF$, $C_{grounding} = 25\ pF$. Both switches operate in pressurized gas at very high voltage and for both it is desirable to provide the shortest rise time possible. Gap distances can be adjusted.
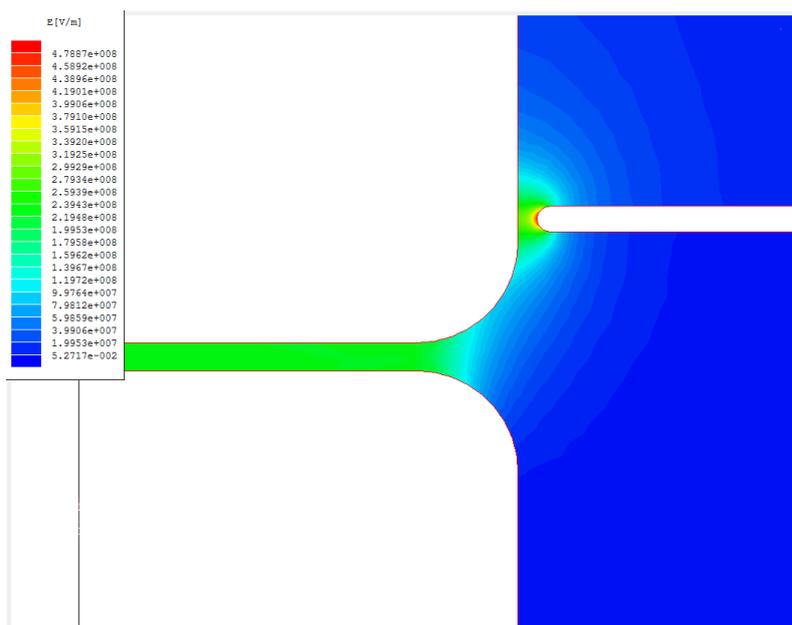
Figure 4.10 Electric field distribution generated by the electrodes of the two switches mounted at the bipolar former input, when a 500 kV voltage is applied on the lower electrode representing the HV output of the Blumlein PFL.

4.2.2.3. **Transmission line**

A 50 Ω transmission line was used to match the bipolar former wave impedance. The diameters of the external conductors at the coaxial input and output are equal to 30.5 mm and 110.9 mm, respectively, to match the impedance. The transmission line input was connected to the bipolar former output and the output of the transmission line short-circuited. To record the output pulse from the transmission line, a V-dot probe was installed inside the wall of the transmission line.

The transmission line design presents a 647 mm long coaxial line. The electromagnetic waves that are transmitted along the transmission line should only propagate in the TEM-mode in order to avoid distortion of the output pulse shape. The fields are assumed to be the same as if the plates were of infinite width, which means that any edge effects or other variations along one transverse coordinate are neglected in a first order analysis of the model. In the TEM mode the transverse electromagnetic wave

has neither E_z or H_z. For a coaxial structure the first higher order mode which can propagate is the TE_{11} mode [4.20][4.21], with a cut-off wavelength λ_c given by

$$\lambda_c = \pi \left[\frac{d_o + d_i}{2} \right] \tag{4.07}$$

and a corresponding cut-off frequency by

$$f_c = \frac{c}{\lambda_c \sqrt{\varepsilon_r}} \tag{4.08}$$

Normally, the line is designed such that the cut-off frequency of the higher order mode is well above the operating frequency. In this case, the length 647 mm is designed to maintain the pulse output and reflection pulse of short-circuited. Then the electromagnetic waves transmitted along the transmission line only propagate in the TEM-mode in order to avoid distortion of the output pulse shape.

4.3. Overall configuration
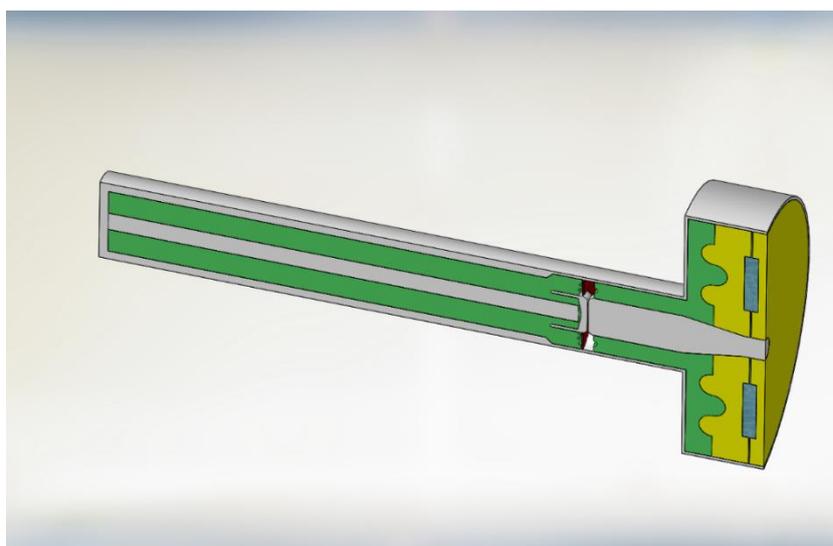
Figure 4.11 3D drawing of the bipolar former
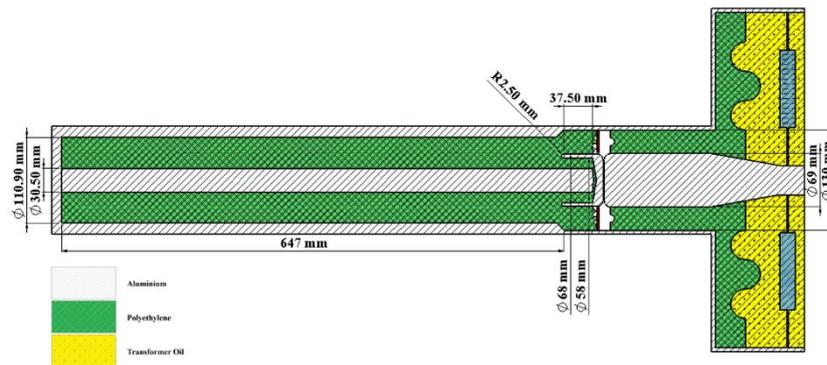
Figure 4.12 Dimensions of the bipolar former
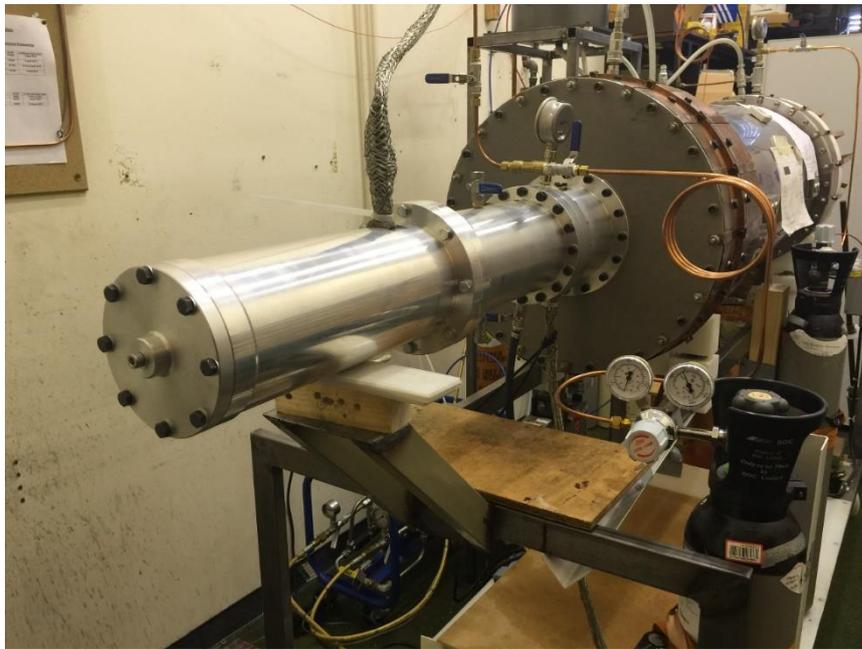
Figure 4.13 Bipolar former connected to the Tesla-Blumlein PFL output

Figures 4.11, 4.12 present the 3D drawing and a schematic of the bipolar former. From right to left it is easy to recognize the $CuSO_4$ resistors, followed by the peaking switch, the grounding switch, the Blumlein PFL, and the transmission line. Figure 4.13 shows the bipolar former assembled unit connected to the Tesla-Blumlein PFL output.

4.4. References

[4.1] P. Delmote, B. Martin (2008). The GIMLI: a compact High-Power UWB radiation source. *EUROEM 2008 Symposium, Ultra-Wideband, Short Pulse Electromagnetics 9*. Lausanne, Switzerland. pp315-321.

[4.2] Yu.V. Vvedenski. (1959). Tiratron generator of nanosecond pulses with universal output. *Izv. vuzov. Radiotekhmka*. N2, pp249-251.

[4.3] Yu. A. Andreev, Yu. I. Buyanov, A. M. Efremov, V. I. Koshelev, B. M. Kovalchuk, K. N. Sukhushin, V. A. Vizir, V. B. Zorin (1997). High power ultrawideband electromagnetic radiation generator. *Proc. 11th IEEE International Pulsed Power Conference*. Baltimore, Maryland, USA. pp730-735.

[4.4] V. G. Shpak, S. A. Shunailov, M. R. Oulmascoulov and M. I. Yalandin (1995). Generation of high-power broadband electromagnetic pulse with PRF of 100 pps. *Proc. 10th IEEE International Pulsed Power Conference*. Albuquerque, New Mexico, USA. pp666-671.

[4.5] V. G. Shpak, M. R. Oulmascoulov, S. A. Shunailov and M. I. Yalandin (1999). Active Former of monocycle high-voltage subnanosecond pulses. *Proc. 12th IEEE International Pulsed Power Conference*. Monterey, California, USA. pp1456-1459.

[4.6] M. I. Yalandin, S. K. Lyubutin, M. R. Oulmascoulov, S. N. Rukin, V. G. Shpak, S. A. Shunailov and B. G. Slovikovsky (2001). Subnanosecond modulator prossessing a 700 MW peak power and average power of 1.5 kW at repetition frequency of 3.5

kHz. *Proc. 13th IEEE International Pulsed Power Conference*. Las Vegas, Neveda, USA. pp1630-1634.

[4.7] Baptiste Cadilhon, Bruno Cassany, Jean-Christophe Diot, Patrick Modin, Eric Merle, Laurent Pecastaing, Marc Rivaletto, Antoine Silvestre de Ferron and Valerie Bertrand (2011). Self-Contained, Hand-Portable, and Repetitive Ultrawideband Radiation Source. *IEEE Transactions on Plasma Science*. 39 (6), pp1549-1559.

[4.8] Yefim Yankelevich and Alex Pokryvailo (2005). A Compact Former of High-Power Bipolar Subnanosecond Pulses . *IEEE Transactions on Plasma Science*. 33 (4), pp1186-1191.

[4.9] http://www.orcad.com/products/orcad-pspice-designer/overview. Last accessed 24th January 2015.

[4.10] B. Martin, P. Delmote and B. Jecko (2007). Design of an ultra compact UWB pulse former. *Proc. 16th IEEE International Pulsed Power Conference*. Albuquerque, New Mexico, USA. pp464-467.

[4.11] S. H. Saw, C. S. Wong and S. Lee (1991). A low-cost high power fast response voltage probe. *Review of Scientific Instruments* . 61 (12), pp534-536.

[4.12] R. E. Beverly III and Associates (2004). Application Notes for Aqueous-Electrolyte Resistors. U.S.A.

[4.13] R. E. Beverly III and R. N. Campbell (1995). Aqueous-electrolyte resistors for pulsed power applications. *Review of Scientific Instruments*. 66 (12), pp5625-5629.

[4.14] Yu. A. Andreev, V. P. Gubanov, A. M. Efremov, V. I. Koshelev, S. D. Korovin, B. M. Kovalchuk, V. V. Kremnev, V. V. Plisko, A. S. Stepchenko and K. N. Sukhushin (2003). High-power ultrawideband radiation source. *Laser and Particle Beams*. 21 (2), pp211-217.

[4.15] A. M. Efremov, V. I. Koshelev, B. M. Koval'chuk, V. V. Plisko, and K. N. Sukhushin (2007). Generation and Radiation of High-Power Ultrawideband Nanosecond Pulses. *Journal of Communications Technology and Electronics* (English translation of *Radiotekhnika i Elektronika,* in Russian). 52 (7), pp756-764.

[4.16] Yu. A. Andreev, A. M. Efremov, V. I. Koshelev, B. M. Koval'chuk, V. V. Plisko, and K. N. Sukhushin (2011). Generation and Emission of High-Power Ultrabroadband Picosecond Pulses. *Journal of Communications Technology and Electronics* (English translation of *Radiotekhnika i Elektronika,* in Russian). 56 (12), pp1429-1439.

[4.17] T. H. Martin, A. Guenther, and M. Kristiansen, Eds. (1996). *J. C. Martin on Pulsed Power*. New York: Plenum Press.

[4.18] P. Delmote, J. P. Duperous, F. Bieth and S. Pinguet (2011). Performance of an ultra compact, high-power, monocycle pulse former for WB and UWB applications. *Proc. 18th IEEE International Pulsed Power Conference*. Chicago, New Illinois, USA. pp558-562.

[4.19] http://www.ansys.com/Products/Electronics/ANSYS+Maxwell. Last accessed 29th December 2015.

[4.20] S. Ramo, J. R. Whinnery, and T. Van Duzer. (1994). *Fields and waves in communication electronics.* John Wiley & Sons Press.

[4.21] N. Marcuvitz. (1986). *Waveguide handbook.* Inst of Engineering & Technology, McGraw-Hill Book Company.

5. Diagnostics

Accurate monitoring of the current and voltage waveforms of the pulsed power system described aids interpretation of the experimental data obtained during testing. Since the pulsed power system is fast and high power, the measurement probes must have a high bandwidth and be located close to the system itself. This chapter describes diagnostics devices that were implemented to investigate both the detailed and the overall performance of the system. The sensors used are based on V-dot and I-dot techniques and are able to monitor the voltage and current waveforms by means of capacitive coupling and inductive coupling respectively.

5.1. BNC type V-dot sensor

5.1.1. Capacitive voltage sensor

Two high-voltage V-dot sensors were designed, manufactured and installed in the Tesla-Blumlein system: one in the outer wall of the Blumlein-PFL and the other in the outer wall of the coaxial load applied at the output. The sensors were both made of BNC type panel connectors.

The voltage sensors developed are capacitively-coupled devices, having the basic arrangement shown in Figure 5.1, mounted in the outer wall of both the oil-filled Blumlein PFL and the coaxial load. They have a coaxial structure, with a central electrode and an outer case in cylindrical geometry with the electrodes separated by an insulator and the sensor is mounted on the wall. The equivalent electric circuit for this sensor is given in Figure 5.2 [5.1], which includes both the sensor components and

the terminated signal cable, where C_1 is the capacitance between the sensor and the high voltage point, and C_2 is that between the electrodes of the sensor itself. R_1 is a resistor attached to the sensor (which is zero due to directly shorting of the sensor to the output terminal) and R_2 is the terminating resistance at the oscilloscope, which is 50 Ω in the present case.
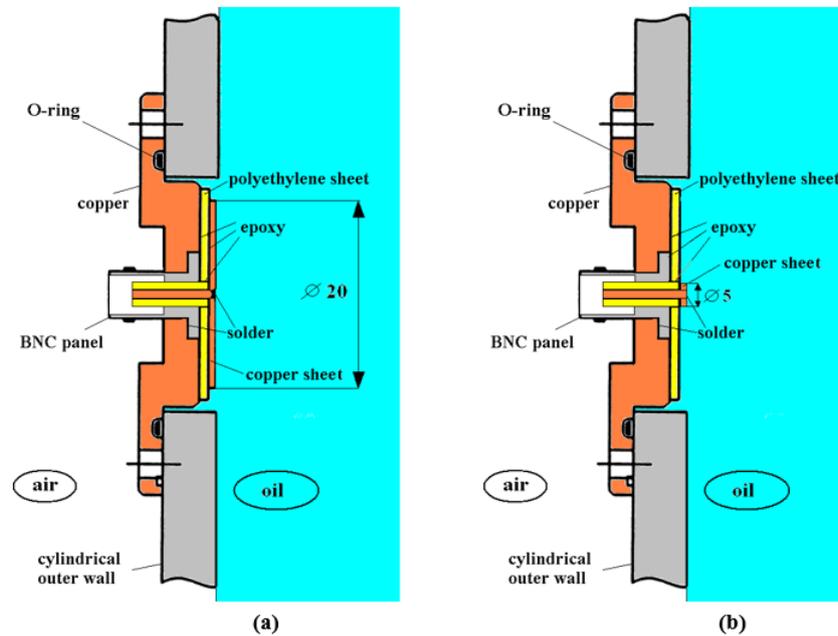
Figure 5.1 Sketch of the two V-dot sensor assemblies mounted in the outer wall of the (a) the oil-filled Blumlein PFL; (b) the coaxial load.
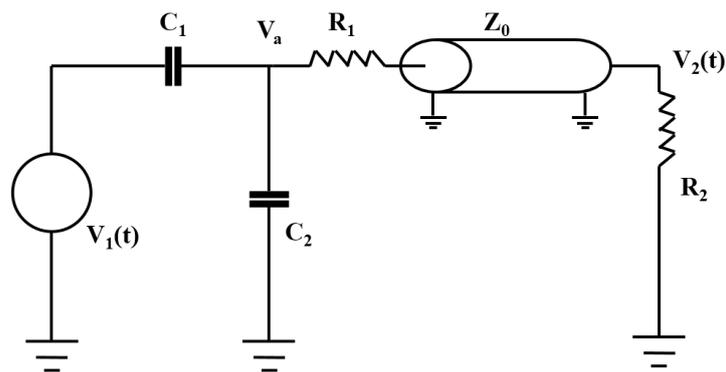
Figure 5.2 Equivalent circuit of the capacitively-coupled voltage sensor [5.1]

If $v_1(t)$ is the voltage input to the sensor and $v_2(t)$ is the corresponding output, it follows from Figure 5.2 that [5.2]

$$C_1 \frac{d}{dt}(v_1 - v_a) = C_2 \frac{dv_a}{dt} + \frac{v_a - v_2}{R_1} \tag{5.01}$$

$$\frac{v_a - v_2}{R_1} = \frac{v_2}{R_2} \tag{5.02}$$

$$v_a = v_2 \frac{(R_1 + R_2)}{R_2} \tag{5.03}$$

$$C_1 \frac{dv_1}{dt} = \frac{v_2}{R_2} + (C_1 + C_2) \frac{(R_1 + R_2)}{R_2} \frac{dv_2}{dt} \tag{5.04}$$

If

$$R_1 + R_2 = R \tag{5.05}$$

and

$$C_1 + C_2 = C \tag{5.06}$$

Equation (5.04) can be re-written as

$$\frac{R_2 C_1}{RC} \frac{dv_1}{dt} = \frac{dv_2}{dt} + \frac{v_2}{RC} \tag{5.07}$$

If RC is very small, the $\frac{dv_2}{dt}$ term in equation (5.07) can be neglected, when the output voltage v_2 becomes proportional to $\frac{dv_1}{dt}$, which means the sensor operates in the so-called 'V-dot' mode [5.2].

5.1.2. Criteria for the voltage sensor

From Figure 5.1 and 5.2, there is only a small spatial variation of the propagating voltage wave over the dimension, which characterizes the capacitive coupling between the probe and also the centre conductor. The RC time constant is much greater than

the times of interest. To make the voltage sensor work satisfactorily, the criteria and conditions that must be met are then

➢ The spatial variation of the field must be such that all information concerning voltage rise time, etc. reaches the sensor without distortion, i.e., $\mathrm{d} \ll \frac{\tau_{rise}c}{\sqrt{k_m}}$ where τ_{rise} is the rise time of the high voltage pulse, k_m is the dielectric constant of medium and d is the distance between voltage surface and the voltage probe. [5.1]

➢ The conductivity of the dielectric medium can be represented as a resistance shunting the coupling capacitance C_1 and therefore the probe gives an accurate measurement only for a time less than the RC product for the medium, where R is the effective resistance offered by the medium from sensor to high voltage point and $\mathrm{C} = C_1$. This time alternatively can be written as $\tau_{medium} = k_m \varepsilon_0 \sigma$, where k_m is the dielectric constant and σ is the conductivity of the dielectric material. [5.1]

➢ $(R_1 + R_2)(C_1 + C_2) \ll \tau_{rise}$ for the probe to work in a differential mode. If RC is much less than the fastest rate of change of the signal, the circuit has an output signal v_2 into a matched load that is proportional to the derivative of the transmission line waveform

$$v_2 = R_2 C_1 \frac{dv_1}{dt} \tag{5.08}$$

This is referred to as the 'V-dot' mode of operation, and the signal requires further integration to obtain the input voltage waveform, v_1. If $(R_1 + R_2)(C_1 + C_2) \gg \tau_{rise}$ the probe acts as capacitive voltage divider with the output signal directly proportional to the transmission line voltage. [5.2]

From equation (5.08) the output voltage from the Blumlein PFL sensor can be taken, where C_1 is the capacitance between the sensor and the Blumlein medium HV electrode and $R_2 = 50 \, \Omega$ is the impedance of the signal cable connecting the sensor to an oscilloscope. The sensor capacitance can be estimated from the fraction of the Blumlein PFL outer-conductor surface occupied by the sensor electrode as [5.1] [5.3]

$$C_1 = \frac{\varepsilon_0 \varepsilon_{oil} d^2}{r_3 \ln\left(r_3/r_2\right)} \tag{5.09}$$

where $\varepsilon_{oil} = 2.25$ is the dielectric constant of the transformer oil around the detector electrode, $d = 20 \, mm$ is the diameter of the sensor electrode (Figure 5.1) and the Blumlein radii $r_2 = 152.5 \, mm$ and $r_3 = 222.25 \, mm$. The capacitance estimated is obtained as $C_{Blumlein} = 9.54 \times 10^{-14} \, F$, and the estimated sensor sensitivity $k_{Blumlein} = C_{Blumlein} \times 50 \, \Omega = 4.76 \, ps.$

For the voltage sensor mounted in the outer wall of the coaxial load, the capacitance cannot be obtained from the formula. The coaxial load is not a cylindrical metal, where the current does not flow on a skin depth like in metal. The current is distributed and the electric field lines are having radically different geometry. The sensor sensitivity is obtained by the calibration.

5.1.3. Rise time consideration of voltage sensors

The rise time of the response of any voltage sensor is normally defined as the time taken for the output response to rise from 10% (t_{10}) to 90% (t_{90}) of the final steady-state value following the application of a step input voltage [5.4]. The rise time of the sensor can be also represented mathematically, by assuming that for high frequency

application it acts as a low-pass filter of resistance R and capacitance C, when the output voltage $v(t)$ following a step-function change at the input is

$$v(t) = V_0 \left(1 - e^{-t/RC} \right) \tag{5.10}$$

where V_0 is the final steady-state voltage.

Thus at time t_{10}

$$v(t_{10}) = 0.1V_0 = V_0 \left(1 - e^{-t_{10}/RC} \right) \; or \; t_{10} = 0.11RC \tag{5.11}$$

Similarly at time t_{90}

$$v(t_{90}) = 0.9V_0 = V_0 \left(1 - e^{-t_{90}/RC} \right) \; or \; t_{90} = 2.3RC \tag{5.12}$$

and the rise time t_r is

$$t_r = t_{90} - t_{10} = 2.19RC \tag{5.13}$$

The rise time of a sensor is also related to its upper frequency limit, i.e., the upper - 3dB point f_{3dB}. At this frequency the impedances due to the resistive and capacitive network are equal and the amplitude of the output voltage has fallen by 50% of its initial value, thus

$$R = \frac{1}{2\pi f_{3dB} C} \tag{5.14}$$

combining equations (5.13) and (5.14) gives

$$t_r = \frac{0.35}{f_{3dB}} \tag{5.15}$$

which is widely used for sensors, oscilloscopes, etc., wherever a rise time has to be specified. It is applied whenever a step response reaches its final value in the shortest possible time without any overshoot. For high frequency applications the sensor response will be subject to an overshoot as the stray inductance becomes significant. However in practice, an overshoot of not more than 10% of the final value is acceptable for equation (5.15) to be regarded as valid.

5.1.4. Calibration of voltage sensors

The voltage sensors designed fulfil all the above conditions. Figure 5.3 shows the voltage sensor for Blumlein PFL and Figure 5.4 presents a voltage sensor mounted on the coaxial load. It is important to note that mounting the sensors is straightforward and rapid and does not require any alteration to the internal coaxial geometry, i.e., no significant inductance is introduced in the circuit and no additional ground connection is required. There is no increase in the risk of high voltage breakdown either, as the original insulation is maintained.

Figure 5.3 Voltage sensor for oil-filled Blumlein PFL

Figure 5.4 Voltage sensor mounted on coaxial load

The capacitively coupled voltage sensors were calibrated using a commercially available voltage divider and a pulse generator. The experimental arrangement is shown in Figure 5.5. The pulse generator TG-70 produced a defined voltage pulse, which was measured by a voltage divider Northstar PVM-6 and a voltage sensor developed from the project. The outputs from the two sensors were compared to calibrate the sensors developed. The output terminal of the voltage sensor was fed to a 500 MHz oscilloscope through a 50 Ω coaxial cable. With results provided by the Northstar PVM-6 and the integrated responses of the voltage sensor being compared in Figure 5.6. The sensor sensitivity of the two sensors obtained from calibration are

$k_{Blumlein} = 5.2\,ps$ and $k_{load} = 1.3\,ps.$

Table 5-1 Electrical parameters of voltage divider, pulsed generator and oscilloscope used in calibrating the voltage sensors

Voltage divider: PVM-6, North Star Research[5.5]	Attenuation ratio: 2000X Max: 100 kV(pulse) Bandwidth: 90 MHz
Pulse generator TG-70, L-3 Communications[5.6]	Maximum charge voltage: 70 kV Output pulse polarity: Positive Output pulse rise time into one 50 Ω cable: $\leq$ 5 ns(10%-90%) Timing delay: ~400 ns Timing jitter: $\leq$ 5 ns rms
Oscilloscope Tektronix TDS 654C[5.7]	Bandwidth: 500 MHz Sampling rate: 5 GS/sec
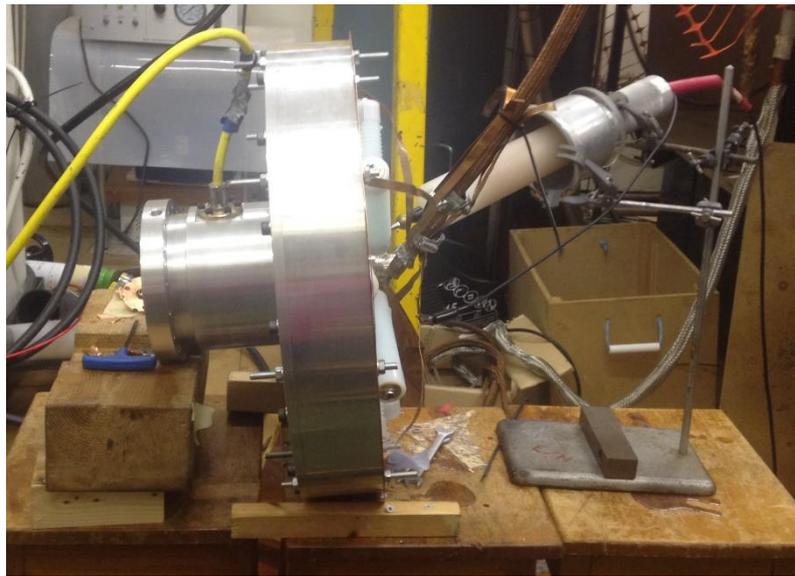
Figure 5.5 Arrangement for calibration of voltage sensor
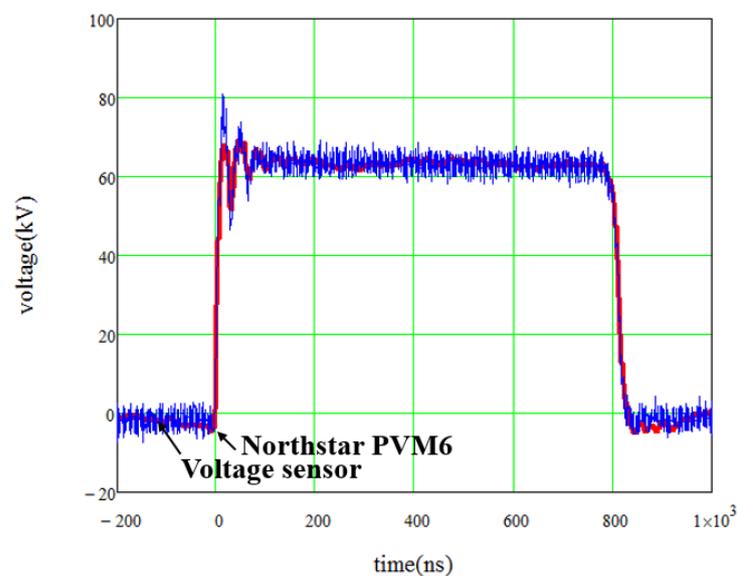
Figure 5.6 Output signal from a voltage sensor (blue line) compared with the corresponding signal from a commercial voltage sensor PVM-6 (red line)

5.2. I-dot sensor [5.1][5.3]

An inductive-shunt current sensor was designed and mounted in the outer wall of the coaxial load. The inductive-shunt current sensor consisted of an annular channel machined in one of a pair of mating flanges as shown in Figure 5.7. The flanges were relieved to accept annular insulation sheets with total thickness Δ thereby insuring that the axial return current on the inside surface of the outer conductor was forced to

95

flow around the inside surface of the annular channel. The high voltage was thus induced across the unbroken insulation by the time variation of the magnetic flux in the annular channel, and this voltage was detected by a capacitively-coupled detector that was recessed into one of the flanges as shown in Figure 5.7. The sensor sensitivity was calibrated using PSpice [5.8] numerical modelling which depends on the two BNC V-dot sensors. The sensitivity obtained was $k_{current} = 75\ ps$
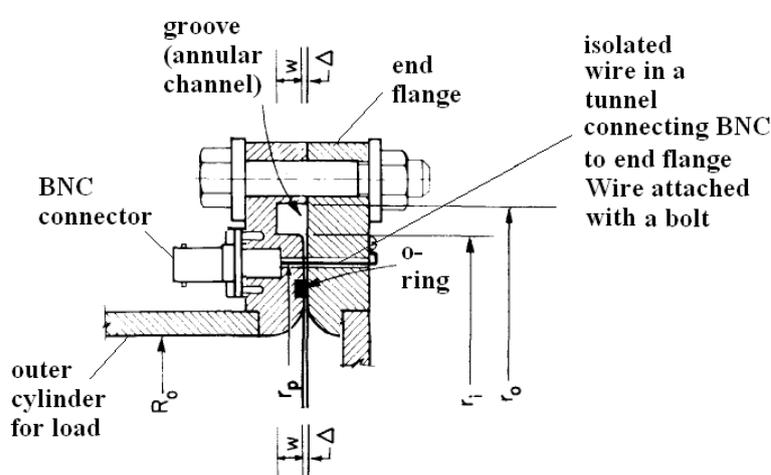
Figure 5.7 Inductive shunt current sensor. (1) Optional series resistor connected by insulated wire at radius $r_p = 91\ mm$ to opposite flange. (2) Annular inductive channel machined in flange surface with outer radius $r_o = 112\ mm$, inner radius $r_i = 106\ mm$ and depth $(w + \Delta) = (6\ mm + 0.25\ mm)$. (3) 'O ring' gas or water seal. (4) BNC signal cable connector. (5) Outer conductor of discharge chamber or water transmission line with radius $R_o = 65\ mm$. [5.1]

5.3. N type V-dot sensor

Voltages are difficult to measure in high frequency structures because they are distributed values and vary with position in high frequency structures. Waves are more easily measured in high frequency networks. A very high bandwidth measuring system is required to measure the output pulses of the bipolar former, because the expected pulse has a bandwidth of up to 2 GHz. Also, the sensors must be able to accurately measure very high voltage levels. Two sensors, both made from 18 GHz female-female

N-type adaptors (Figure 5.8) are placed correspondingly at the Blumlein-PFL output, one after the 130 Ω resistor and the other inside the wall of the bipolar former 50 Ω output transmission line. Two sensors are connected, using double shielded 18 GHz coaxial cables and attenuators, to a 18 GHz, 60 GS/s Lecroy real-time digital oscilloscope. The oscilloscope is housed in a Faraday box and powered by a UPS unit.

A three-dimensional model for the V-dot sensors was developed using the Computer Simulation Technology (CST) electromagnetic microwave studio software [5.9]. Results obtained with this software suggest that off-the-shelf N-type connectors can be directly used as ultrafast sensors up to a frequency of at least 6 GHz. Using a dedicated experimental assembly, it was demonstrated in practice that such sensors have indeed the characteristics indicated by the CST model. Finally, the same two-step technique was used to analyse the characteristics of ultrafast V-dot probes constructed with off-the-shelf SMA-type connectors.

Figure 5.8 AAREN precision adaptor N female to N female, DC-18 GHz

5.3.1. Numerical study of ultrafast V-dot sensor

One method of describing the behaviour of a two port network is in terms of incident and reflected waves. This method is in terms of scattering parameters usually denoted as s-parameters. To design the sensors, the s-parameters of the V-dot sensor was

97

established using CST software[5.9]. S-parameters are transmission and reflection coefficients, with transmission coefficients commonly called gains or attenuations, and the reflection coefficients are directly to VSWRs and impedance.

5.3.1.1. Definition of scattering parameters (s-parameters)
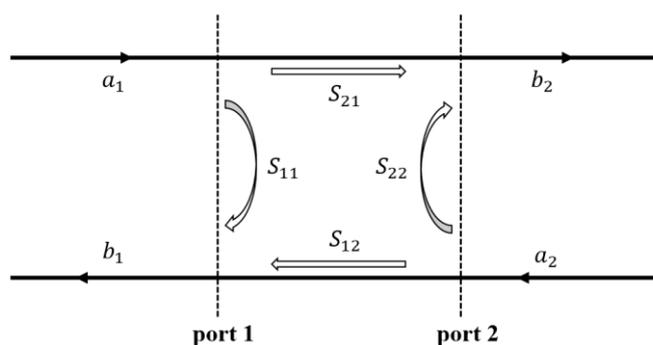
Figure 5.9 Signal flow diagram of the transmission element as a two-port network [5.10]

The significance of the signal flow diagram given in Figure 5.9 can be interpreted as follows: the wave a_1 incoming at the input port gives off part of its energy at the output port, via the internal channel S_{21}, whereupon a wave b_2 leaves the second port; the energy which is not absorbed by the second transmission port leaves the second port via an internal channel S_{11}, as part of the reflected wave b_1 at the input port. By analogy, the wave a_2, incoming at the output, supplies a contribution to b_2 via S_{22}, and to b_1 via S_{12}. This allows the following two equations to be complied [5.10]

$$b_1 = a_1 \cdot S_{11} + a_2 \cdot S_{12} \tag{5.16}$$

$$b_2 = a_1 \cdot S_{21} + a_2 \cdot S_{22} \tag{5.17}$$

The following two postulates serve the physical significance and the measurability of the s-parameters:

➢ The two-port network is connected at the output in such a way that $a_2 = 0$; i.e. either undisturbed radiation of b_2 into space or, more realistically, termination with a load Z_B via a line and, if necessary, a measurement arrangement with wave impedance $Z_W = Z_B$, so that no outwardly reflected wave can pass to the output port. The two-terminal network equivalent resistance Z_B of the external consumer, is independent of the two-port network that is to be measured, is the reference resistance for the measurement of the s-parameters. The following relationships then apply:

$$S_{11} = \frac{b_1}{a_1} \ and \ S_{21} = \frac{b_2}{a_1} \ when \ a_2 = 0 \qquad (5.18)$$

It can be seen that, S_{11} is the input s-parameter factor and S_{21} is the forward s-parameter factor, with the reference resistance $Z_B = 50 \ \Omega$. [5.10][5.11]

➢ The two-port network is connected in such a way that $a_1 = 0$; i.e. the power is fed in at port 2, and matched at port 1, as explained. The following relationships then apply:

$$S_{12} = \frac{b_1}{a_2} \ and \ S_{22} = \frac{b_2}{a_2} \ when \ a_1 = 0 \qquad (5.19)$$

It can be seen that, S_{12} is the reverse s-parameter factor, S_{22} is the output s-parameter factor, with the reference resistance $Z_B = 50 \ \Omega$. [5.10][5.11]

For sensors design case, the s-parameters are defined as in Figure 5.10.
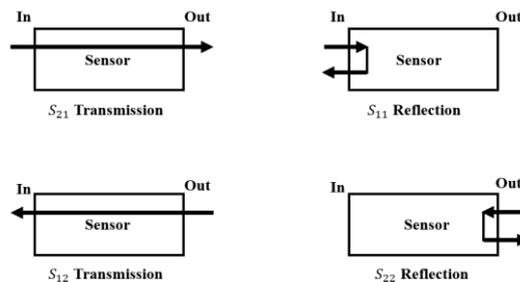
Figure 5.10 S-parameters of sensors designed

5.3.1.2. CST modelling of V-dot sensor

Figure 5.11 and Figure 5.12 show the CST model [5.9] for the V-dot sensor placed at the Blumlein-PFL output after the 130 Ω resistor and mounted inside the wall of the output transmission line. All dimensions are equal to the real design including bipolar former, transmission line and V-dot sensor. Arrows show the voltages monitors in CST [5.9]. The V-dot is made from the N type female-female adaptor, bought from Admiral Microwave Ltd. [5.12], having a PER MIL-STD-348A N type female interface with the dimensions shown in Figure 5.13.
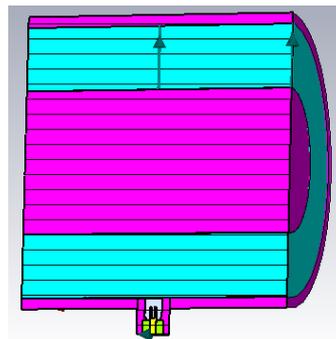
Figure 5.11 CST model of the V-dot sensor placed at the Blumlein PFL output.
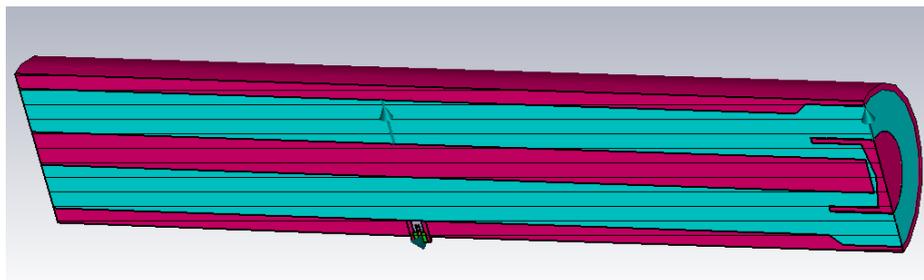
Figure 5.12 CST model of the bipolar former including second V-dot sensor.
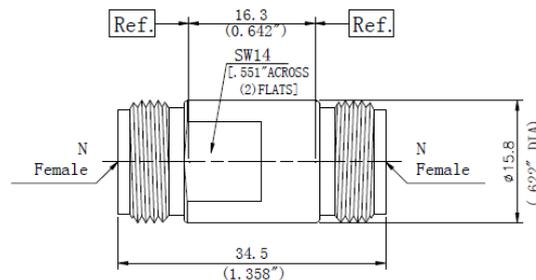
Figure 5.13 Dimensions of AAREN precision adaptor N female to N female, DC-18 GHz [5.12]

A Gaussian voltage impulse was applied at the bipolar former input and three so-called voltage monitors were used by the software to indicate the voltage signal at various positions inside the unit. Three CST voltage monitors used in the numerical study of second sensor are placed as follows: V_1 at the unit input (right hand side), V_2 across the 50 Ω transmission line at a position corresponding to the real V-dot sensor and V_3 at the sensor output. Figure 5.14 shows main results from CST study, which indicates that the off-the-shelf N-type connectors can be directly used as ultrafast sensors, acting as dV/dt V-dot operation. In addition, the s-parameter S_{21} of the sensor is linear up to a frequency of at least 6 GHz.
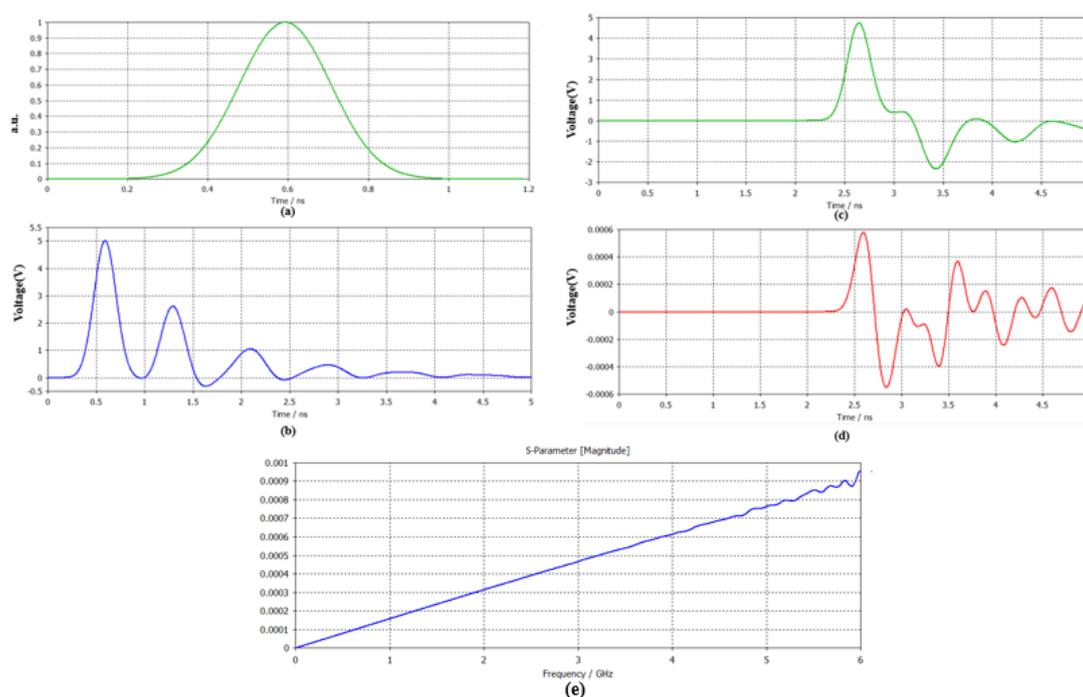
Figure 5.14 Main results of second V-dot sensor from CST study
(a) 3 GHz excitation Gaussian signal applied at the CST input port of the bipolar former; the output signals from the three CST voltage monitors of Figure 5.11 are (b) from V_1, (c) from V_2, (d) from V_3; (e) S_{21} parameters demonstrates that the sensor is linear up to 6 GHz.

5.3.1.3. Calibration of the V-dot sensors

According to the output signals from CST such as Figure 5.14(c), 5.14(d), the sensors can be calibrated. For first ultrafast V-dot sensor which placed at the Blumlein PFL after the resistor, sensor sensitivity obtained is $k_{N-Blumlein} = 3.03 \times 10^{-14} \, s$. For second ultrafast V-dot sensor which mounted in the outer wall of the bipolar former output transmission line, the sensor sensitivity obtained is $k_{N-bipolar} = 1.98 \times 10^{-14} \, s$. The calibration curves are shown in Figure 5.15.

| (a) | (b) |
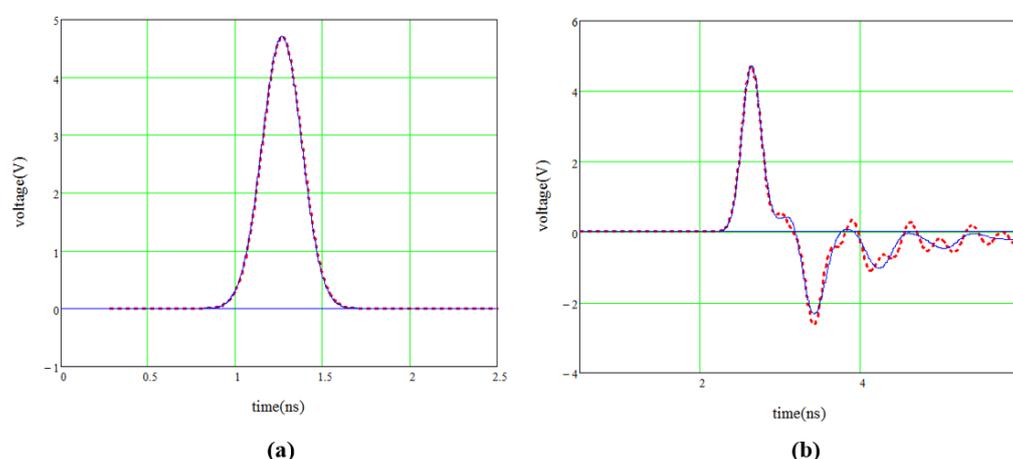
Figure 5.15 Calibration curves for: (left) first V-dot sensor after Blumlein and (right) second V-dot sensor after bipolar former. Output signal from position of transmission line corresponding to the real V-dot sensor: red dotted trace; Integrated signal of output signal from V-dot sensor: blue trace.

5.3.2. Experimental study of ultrafast V-dot sensor

Dedicated experimental assemblies were used to demonstrate that in practice such sensors have indeed the characteristics indicated by the CST model.

5.3.2.1. First arrangement: Multi-GHz coaxial cable

A 6 GHz coaxial cable was used as a transmission line with a N type adaptor and a SMA connector mounted. Figure 5.16, Table 5.2 and Table 5.3 present the construction and characteristics of the coaxial cable.
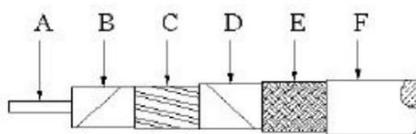
Figure 5.16 Construction of the coaxial cable [5.13]

Table 5-2 Construction data of coaxial cable

A Inner Conductor	Bare Copper Aluminum d=2.77 mm
B Dielectric	Foam Polyethyene D=7.3 mm
C First Outer Shield	Aluminum Tape
D Second Outer Shield	Tinned Copper
E Third Outer Shield	Tinned Copper
F Jacket	PE O=10.29 mm

Table 5-3 Characteristics data of coaxial cable

Impedance (Ω)	50.025
Capacitance (pF/m)	78.4
Frequency, Max (GHz)	6
Velocity of Propagation (%)	85

Figure 5.17 shows the CST numerical modelling of the arrangement with arrows indicating the voltages monitors in CST [5.9]. Figure 5.18 presents the experimental assembly of the arrangement. The cable was connected to a network analyser to obtain the S_{21} parameters of the N type adaptor and the SMA connector separately. The variations of the S_{21} parameters obtained experimentally were compared with the simulation results from CST model (Figure 5.19). The results indicate that the coaxial cable allows proper operation at multi-GHz level and prove that off-the-shelf connectors and adaptors can be used to measure, in the multi-GHz frequency range, electromagnetic waves propagating along transmission lines.
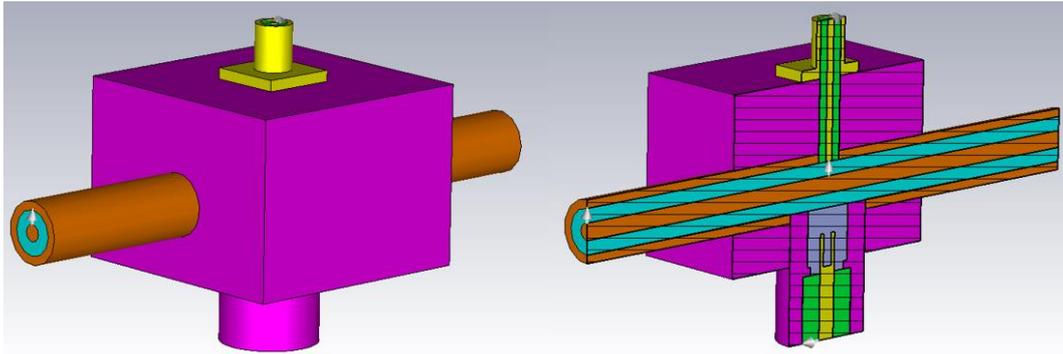
Figure 5.17 CST model of Multi-GHz coaxial cable arrangement

Figure 5.18 Multi-GHz coaxial cable arrangement
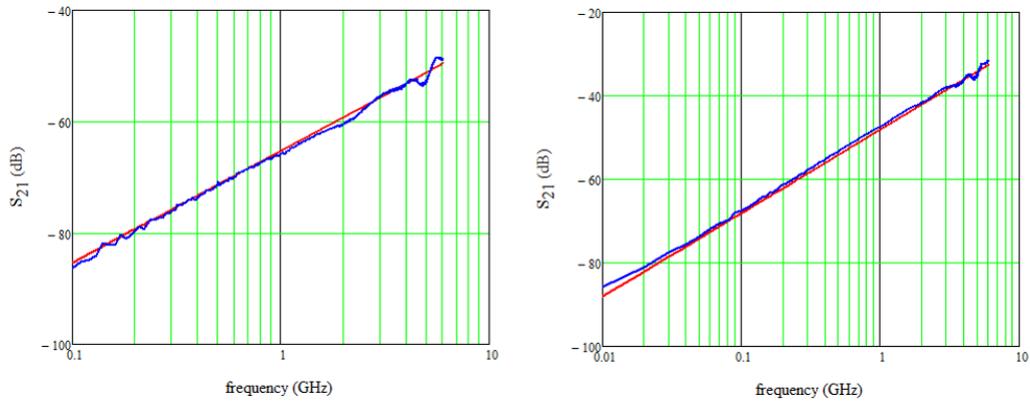
Figure 5.19 Variation with frequency of the S_{21} coefficients for: (left) N-type adaptor and (right) SMA connector. CST: red trace; experiment: blue trace.

5.3.2.2. Second arrangement: biconical transmission line

A biconical transmission line was built to test the ultrafast V-dot sensors. The impedance of the transmission line is 50 Ω along the construction. Two N type adaptors and two SMA connectors were mounted. Figure 5.20, 5.21 present the sketch and design details of the biconical transmission line.

Figure 5.20 Sketch of biconical transmission line

Figure 5.21 Design details of the biconical transmission line

Figure 5.22 shows the CST numerical model of the experimental arrangement with arrows indicating the voltages monitors in CST [5.9]. Figure 5.23 presents the experimental assembly of the arrangement. The biconical transmission line was connected to a network analyser to obtain the S_{21} parameters of N type adaptor and SMA connector separately. The variations of S_{21} parameters obtained from experimental were compared with the simulation results from CST model (Figure 5.22). The results indicate that the biconical transmission line allows proper operation

at multi-GHz level and prove that off-the-shelf connectors and adaptors can be used to measure, in the multi-GHz frequency range, electromagnetic waves propagating along transmission lines.

Figure 5.22 CST model of biconical transmission line arrangement

Figure 5.23 Biconical transmission line arrangement
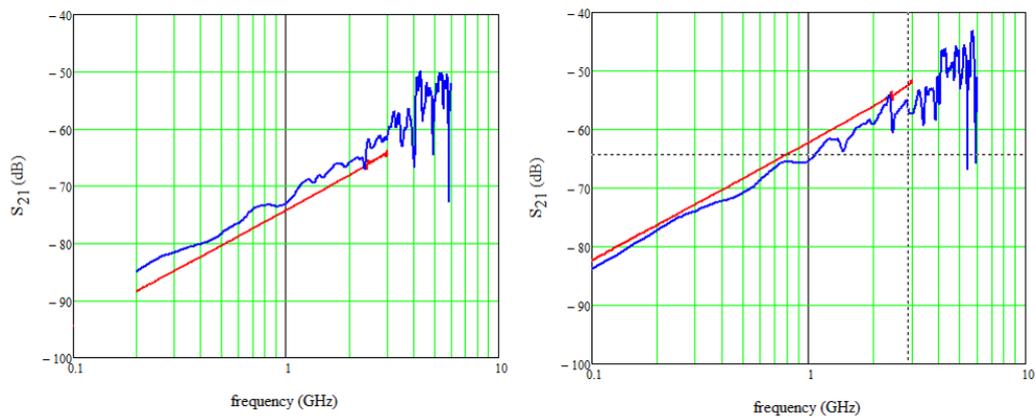
Figure 5.24 Variation with frequency of the S_{21} coefficients for: (left) N-type adaptors and (right) SMA connectors. CST: red trace; experiment: blue trace.

5.4. Electro-optic sensor

5.4.1. Principle of electro-optic sensor

The bipolar pulse generator is built for cancer treatment inside the water for the further research. An electro-optic sensor was designed at Loughborough to measure the pulsed intense electric fields [5.14]. The measurement of the electric field inside the water is only possible using electric-optic diagnostics based on either the Pockels effect [5.15] or the Kerr effect [5.16]. The Pockels effect uses a crystal as an active medium and therefore the probe must be calibrated when inserted in a liquid. The Kerr effect used the liquid itself as an active medium, making the measurement extremely convenient. Kerr effect measurements of electric fields were implemented to give valuable 'in situ' information for a number of high-voltage pulsed power systems. These include water-filled pulse forming lines (PFLs), closing switches operated under water and monitoring of the pulsed electric field in PEF equipment used in medical applications. In previous work [5.14], the main technical issues related to measuring the Kerr effect in water were highlighted and it was demonstrated that, in most cases, the values of the published Kerr constant are at best unreliable. There is however a supplementary issue, not covered by the previous work, that relates to the variation of the Kerr constant with temperature. To provide a reliable measurement of temperature variation, experiments of the Kerr constant for water between 19 ℃ and 45 ℃ were performed.

The experimental arrangement, presented in Figure 5.25 and 5.26, is similar to that used in previous Kerr experimentation [5.14]. A 658 nm laser launches a light beam through a water filled Kerr cell maintained at a constant temperature by a water bath

surrounding the cell. The temperature inside the cell is accurately measured with a thermocouple immediately before and after each test. The water inside the cell is both purified and heated by a system comprising a pump, a filter and a heating resistance. The Kerr cell described in [5.14] uses a pair of 400 mm long parallel-plate stainless-steel electrodes, placed a distance $d = 5.00 \pm 0.05$ mm apart with the aid of a polyethylene support. For the present work however, the material for the support was changed to PMMA (Polymethylmethacrylate), having a thermal expansion coefficient of about $70 \cdot 10^{-6}/°K$, so that even a twenty degree temperature increase will cause only a 7 μm increase of the 5 mm initial separation measured at 25 ℃, representing a change of 0.14%. The cell has been mounted vertically to encourage air bubbles to surface easily. The transient electric field $E(t)$ is generated between the cell electrodes by the application of a voltage impulse from a high-voltage trigger generator type TG-70 (L-3 Applied Technologies [5.6]). The corresponding time-varying light intensity $I(t)$ is detected by an opto-electronic converter and can be predicted using [5.14]:

$$I(t) = I_{max} sin^2 \left[\frac{\pi B l' V^2(t)}{d^2} \right]$$
(5.20)

where I_{max} is the maximum light intensity, B is the Kerr constant and $l' = d^2 \int_0^l E(x)^2 \, dx$ is the effective optical path length [5.14], calculated for the present cell using 3D ANSYS Maxwell[5.17] software as $l' = 404.11 \, mm$. The voltage $V(t)$ applied to the Kerr cell electrodes is measured using a North Star voltage probe type PVM 6 [5.5], mounted in a different way from that used in [5.14], a technique adopted

to simplify data interpretation and improve the precision of the measurement(Figure

5.27).
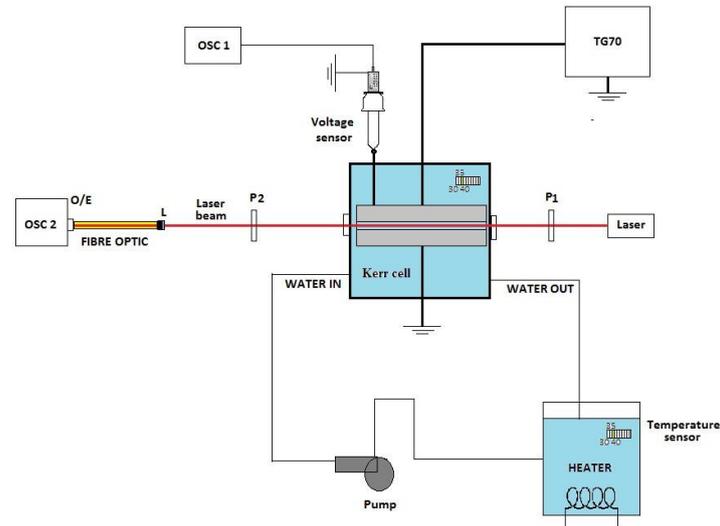
Figure 5.25 Practical arrangement for Kerr experiments, with the main elements listed below:
Electrical: TG70 is a pulsed voltage generator connected to the Kerr cell electrodes, with the high-voltage sensor attached to an oscilloscope (OSC 1). Optics: a battery-operated laser launches the light into the Kerr cell, with P_1 and P_2 being two crossed polarisers and L a collimating lens connected to a fibre-optic; O/E represents an opto-electronic convertor attached to an oscilloscope (OSC 2). Water system: a heated water tank (Heater) is connected through a pump and filter (not shown) to the Kerr cell.

(a)   **(b)**
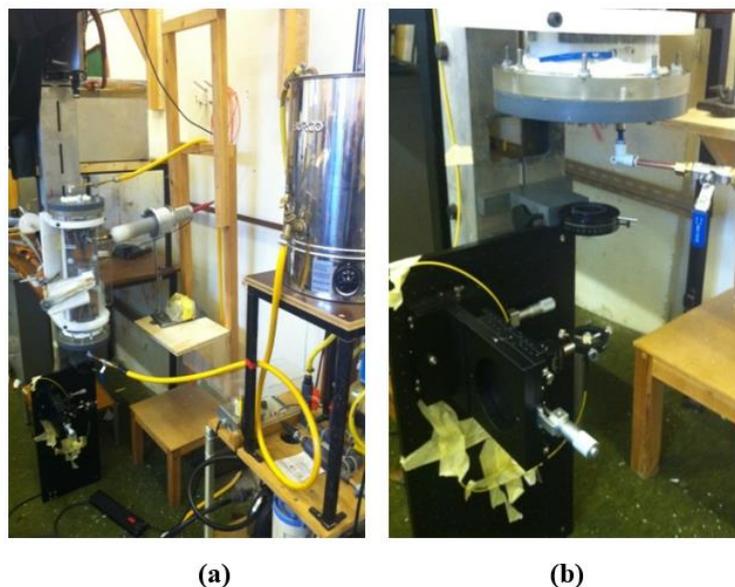
Figure 5.26 Experimental assembly. (a) Overall view of the Kerr cell with high-voltage sensor and water heating tank. (b) Detail showing a polariser and the high-precision mechanical components used to align the collimator lens.
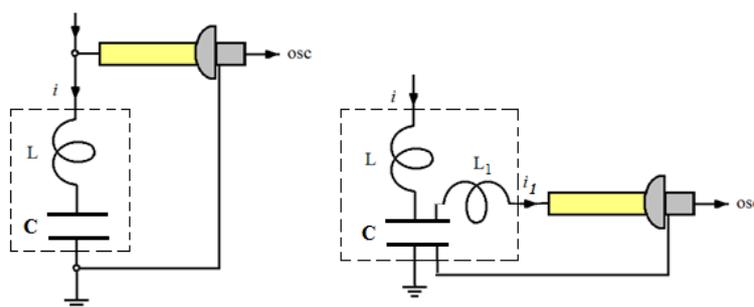
Figure 5.27 Alternative ways of mounting the voltage sensor to measure the voltage impulse applied to a Kerr cell, represented by the dotted rectangle

There are two ways in which a voltage sensor can be mounted to measure the voltage impulse applied across the Kerr cell capacitance C: In first case a current i having high time rate-of-change di/dt flows through the cell and therefore the voltage across C is different to that measured by the voltage sensor, which includes the supplementary inductive term $L\,di/dt$. To obtain the required result, a correction must be made, as indicated in [5.14]. In second case the connection between the sensor and the Kerr cell has a low value of self-inductance L_1 and, due to the high-impedance of the sensor, the time rate-of-change of the current i_1 is extremely small and as a consequence the inductive voltage term $L_1\,di_1/dt$ is negligible. In this case the sensor measures accurately the voltage across C and no corrections are required.

5.4.2. Temperature dependence of the Kerr constant for water at 658 nm and for pulsed intense electric fields

In each test a reproducible train of pulsed electric fields with a maximum peak in excess of $100\ kV/cm$ was applied between the Kerr cell electrodes, while from test to test the water temperature was varied between $292\ K\ (19\ ℃)$ and $318\ K\ (45\ ℃)$. Due to presently not well-understood phenomena (accumulation of air bubbles, water

turbulence, etc.), higher temperature shots do not provide reliable data. Typical experimental results are shown in Figure 5.28. The technique used to analyse the results and a detailed discussion of the errors were both presented [5.14]. As expected, the Kerr constant B is affected by the temperature T and for the data points in Figure 5.29 the best polynomial interpolation was found to be:[5.18][5.19]

$$\frac{B(T,\lambda_{ref})}{B(T_{ref},\lambda_{ref})} = \sum_{k=0}^{3} \frac{A_k}{T^k} \tag{5.21}$$

where the result is normalised to the Kerr constant $B\left(T_{ref},\ \lambda_{ref}\right) = 2.746 \cdot 10^{-14} \frac{m}{V^2}$ at the arbitrarily chosen reference temperature of $T_{ref} = 294.0\ K$, with $\lambda_{ref} = 658.0\ nm$. The four polynomial constants are:

$A_0 = 12.60;\ A_1 = -1.160 \cdot 10^4\ K;\ A_2 = 3.651 \cdot 10^6\ K^2;\ A_4 = -3.650 \cdot 10^8\ K^3;$
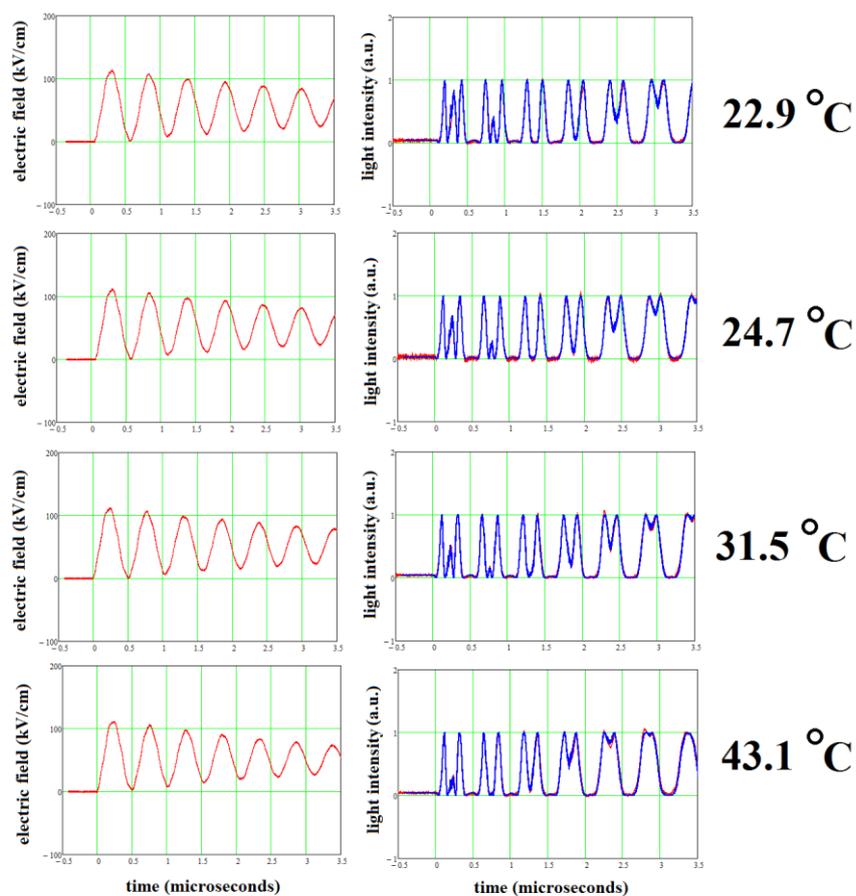
Figure 5.28 Typical oscilloscope recordings at various temperatures (as indicated). Left column: the train of electric field impulses applied on the Kerr cell electrodes, derived from the voltage signal; Right column: the corresponding recorded optical signals (blue lines); qualitatively, a decrease of the Kerr constant for higher water temperatures is clearly indicated by a reduced number of light oscillations. Theoretical predictions (red lines) and voltage data are practically undistinguishable.
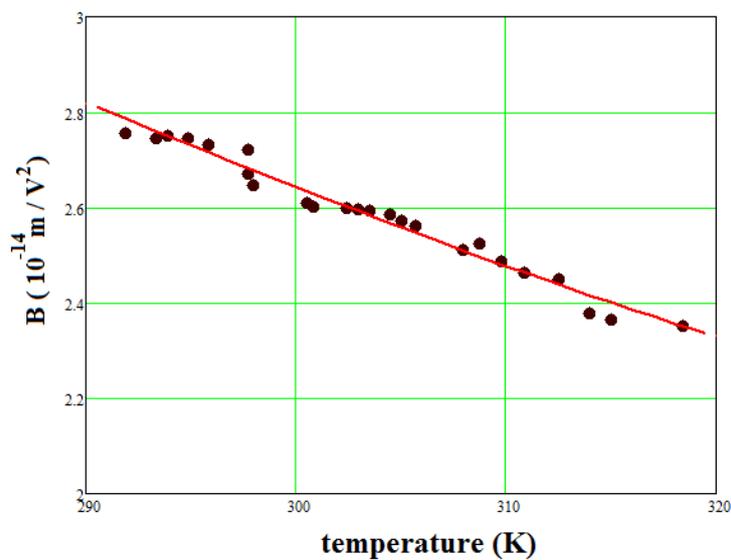
Figure 5.29 Temperature dependence of the Kerr constant for water at 658 nm. Full circles are experimental data while the line represents a temperature polynomial fit.

5.5. References

[5.1] C. A. Ekdahl (1980). Voltage and current sensors for a high-density z-pinch experiment. *Review of Scientific Instruments*. 51 (12), pp1645-1648.

[5.2] R. Kumar, B.M. Novac, I.R. Smith and J. Larour (2007). Simple, non-invasive and wide-band current and voltage sensors for use with coaxial cables. *Proc. 16th IEEE International Pulsed Power Conference*. Albuquerque, New Mexico, USA. pp486-489.

[5.3] C. A. Ekdahl (1980). Capacitively-coupled inductive sensors for measurements of pulsed currents and pulsed magnetic fields. *Review of Scientific Instruments*. 51 (12), pp1649-1651.

[5.4] F. B. Frungel. (1965). *High speed pulse technology Vol. 1: Capacitor Discharges, Magnetohydrodynamics, X-Rays, Ultrasonics.* Academic Press.

[5.5] http://www.highvoltageprobes.com. Last accessed 29th January 2015.

[5.6] http://www2.l-3com.com/ati/pdfs/PA80_PA100.pdf. Last accessed 29th January 2015.

[5.7] http://www.tek.com/. Last accessed 29th January 2015.

[5.8] http://www.orcad.com/products/orcad-pspice-designer/overview. Last accessed 29th January 2015.

[5.9] https://www.cst.com/. Last accessed 29th January 2015.

[5.10] F. Nibler. (1996). *High-frequency circuit engineering, IEE circuits and systems series 6.* The Institution of Electrical Engineers.

[5.11] E. Da Silva. (2001). *High frequency and microwave engineering.* MPG Books Ltd..

[5.12] http://www.admiral-microwaves.co.uk/index.php. Last accessed 29th January 2015.

[5.13] http://www.timesmicrowave.com/. Last accessed 29th January 2015.

[5.14] B. M. Novac, F. A. Banakhr, I. R. Smith, L. Pecastaing, R. Ruscassie, A. S. de Ferron and P. Pignolet (2012). Demonstration of Kerr Constant of Water at 658 nm for Pulsed Intense Electric Fields. *IEEE Transaction on Plasma Science*. 40 (10), pp2480-2490.

[5.15] G. Gaborit, P. Jarrige, F. Lecoche, J. Dahdah, E. Duraz, C. Volat and L. Duvillaret (2014). Single Shot and Vectorial Characterization of Intense Electric Field in Various Environments with Pigtailed Electrooptic Probe. *IEEE Transaction on Plasma Science*. 42 (5), pp1265-1273.

[5.16] J. Kerr (1875). A New Relation between Electricity and Light: Dielectrified Media Birefringent. *Philosophical Magazine*. 50(19), pp337-348.

[5.17] http://www.ansys.com/Products/Electronics/ANSYS-Maxwell. Last accessed 29th January 2015.

[5.18] Y. Chen and W.H. Ortung (1972). Temperature Dependence of the Kerr Constant of Water. *The Journal of Physical Chemistry*. 76 (2), pp216-221.

[5.19] R.K. Khanna, E. Dempsey, and G. P. Jones (1978). Kerr constant of water from 280 to 350 K at 632.8 nm. *Chemical Physics Letters*. 53(5), pp542-544.

6. Experimental arrangements and numerical modelling

This chapter introduce a description of the hardware items on the completed generator and numerical modelling which was used to analyse the generator.

6.1. Experimental arrangement

To study the pulsed power generator, a Tesla transformer, Blumlein PFL, bipolar former and diagnostics as stated in Chapter 2, 3, 4 and 5 were constructed. This chapter presents the experimental arrangement used for the experiments, which includes the initial power supply for the system, spark gaps, resistive load, and the data processing system. The completed generator unit is shown in Figure 6.1.
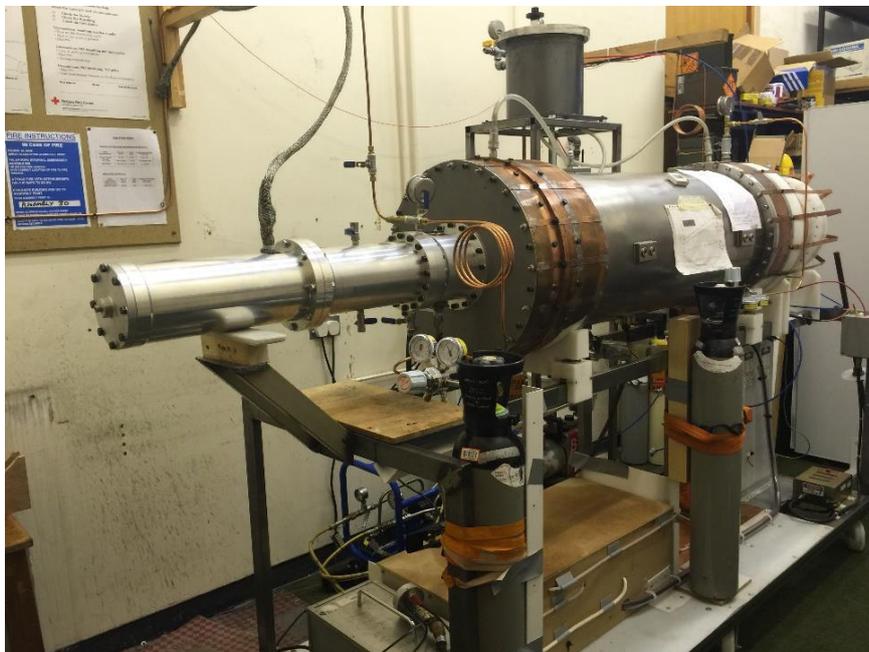
Figure 6.1 The completed generator unit

6.1.1. Initial power supply for the system

6.1.1.1.   High voltage charging power supply

This is a commercially available TDK Lambda model 202A-40kV series shown in figure 6.2 which is an OEM style high voltage power supply designed for operation in two modes. In the most common format it is a constant current capacitor charging supply which will reliably charge HV capacitors. The 202A can also operate as a constant voltage, continuous output DC power supply with the addition of an external filter capacitor. The 202A provides 2000 J/s of average power and can be paralleled indefinitely for higher total system power.

Figure 6.2 HV charging power supply [6.1]

6.1.1.2.   Capacitor bank

A typical pulsed power facility, the required energy is commonly accumulated from the energy source at relatively low power levels and subsequently stored. Depending on the application and requirement, the storage may be either in a capacitive energy storage or an inductive form or a combination of the two. In this case, capacitive energy storage used consists of a number of high voltage capacitors connecting parallel which is referred as a capacitor bank. The capacitor bank can supply large amounts of current[6.2].

117

The capacitors used for the capacitor bank satisfy the conditions:

- Rated voltage $\geq$ 30 kV

- Voltage reversal withstand capability 100%

- Low dissipation factor $<$ 2%

- Low inductance

Two parallel-connected capacitors GAEP type 37331[6.3] were therefore used (Figure 6.2). The capacitors are extended foil, single-ended plastic case capacitors which have compact designs for high voltage, very low inductance, high rep-rate, and pulsed applications. The dimension of the capacitor is height $\cdot$ width $\cdot$ length $= 58 \cdot 150 \cdot 699 \ mm^3$. Each capacitor has a capacitance of 154 nF and a self-inductance of 15 nH and capable of being charged to an initial voltage 50 kV.

Figure 6.3 Capacitor bank arrangement

6.1.1.3. Trigger generator

The trigger generators from R. E. Beverly III & Associates [6.4] employ all solid-state, IGBT topology and are designed to fire the SG-series trigatron spark gaps. The THD-

02B-02a trigger head is a self-contained, HV pulse generator with an integral pulse transformer. A complete system consists of a THD-02B-02a trigger head, an FO-series optical fiber link and a PG-103D control unit.

The THD-02B-02a (Figure 6.4) is based on the switch requirements (trigger voltage and rise time) and also on the operational needs (repetition rate and isolation voltage). The THD-02B system utilizes a trigger transformer with exceptionally large DC isolation (primary-to-secondary hold-off potential). The primary application for the THD-02B head is high current, high charge-transfer switches. The trigger heads are enclosed in heavy-gauge steel boxes for increased immunity to EMI, RFI, and magnetic fields. Transformers and boxes have provisions for surface mounting and attachment. All trigger heads receive their fire command through an optical fiber link. These utilize industry FO-20 20m standard ST™ connectors and multimode fiber (Avago 820-nm multimode HFBR-1412/2412 transmitter-receiver links). [6.5]

Figure 6.4 THD-02B-02a trigger head

Model PG-103D4-02a (Figure 6.5) is an all solid-state pulser employing IGBT topology. It is designed to trigger SG-series trigatron spark gaps and is capable of controlling up to four switches. A complete system consists of a control box, optical fiber link(s), trigger head(s), and trigger transformer(s). Since there is no direct electrical connection between the control box and trigger head, noise immunity is

greatly enhanced. The number of channels is specified at the time of order, but the system may be subsequently upgraded at the factory with additional channels. Multi-channel systems offer internally programmable delays, which is useful with crowbar applications, for example. When properly configured and installed, the model PG-103D trigger generator will fire independent or multiple-channel switches with ratings to 100 kV and 500 kA. [6.6]

Figure 6.5 PG-103D front panel and rear panel showing four channel unit [6.6]

6.1.2. Spark gaps

6.1.2.1.   Trigatron

For low-repetition rate switching, a trigatron type SG-101M-75C (R. E. Beverly III & Associates[6.4]) was used to trigger pulse transformer shown in Figure 6.6 and 6.7. The SG-101M-75C is a moderate-HV, moderate-current switch with enhanced

electrodes for small charge-transfer applications. A supply of flowing nitrogen is required for operation within the nominal voltage range. Table 6.1 presents the detailed specifications for switch SG-101M-75C and the Figure 6.8 shows the self-breakdown voltage(V_{sb}), recommended operating voltage(V_{op}), and minimum operating voltage for reliable triggering(V_{min}) using a PG-103 trigger generator. The operating voltage curve is calculated using approximately 85% of the self-breakdown voltage. Actual operation above the recommended voltage $(|V_g| > V_{op})$ increases the probability of pre-fire; operation below the recommended voltage $(|V_g| < V_{op})$ increases the breakdown delay time and trigger jitter. From Figure 6.8, the trigatron operates in ambient air, pressurized with nitrogen, between about 20 kV and 30 kV. The trigatron resistance R_{switch} varies with the operating voltage, from tens of mΩs at initial voltage $V_0 = 20\ kV$ to about $1\text{m}\Omega$ at $V_0 = 30\ kV$. [6.7]

Table 6-1 Detailed specification for SG-101M-75C

Parameter	Specification	
Internal gas	N$_2$	10%SF$_6$: N$_2$
Internal gas pressure, kPa(psig)	0-100(0-15)	0-50(0-7)
Operating voltage(V_g), kV	10-30	22-40
Breakdown delay, ns	<250	
Trigger jitter, ns	≤100	
Switch inductance, nH	<20	
Trigger method	Trigatron	
Electrode material	Sintered W-Cu alloy(2.5 cm diameter)	
End-plate material	Ni-plate brass	
Discharge gap, mm	6.35	
Exterior body dimensions, mm(inches)	127(5.00) diameter × 40.6(1.60) height	
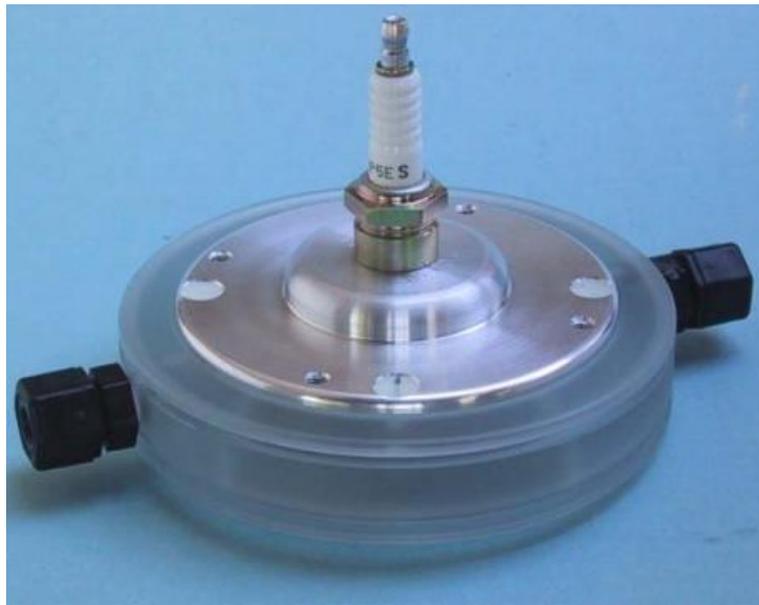
Figure 6.6 Switch SG-101M-75C [6.7]
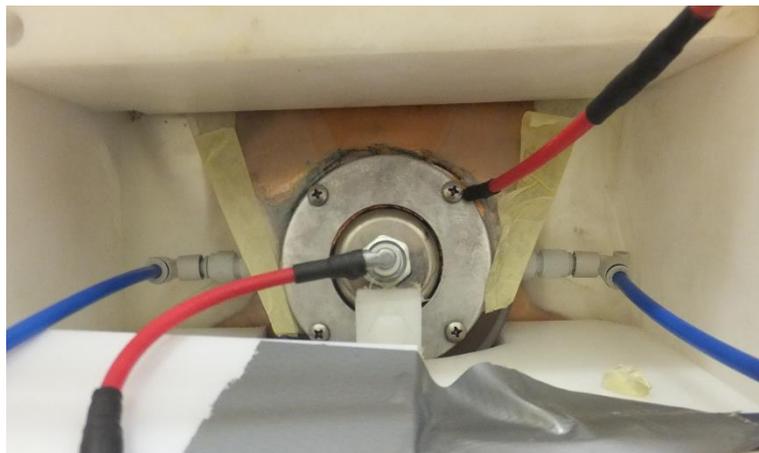
Figure 6.7 switch mounted in the Tesla transformer
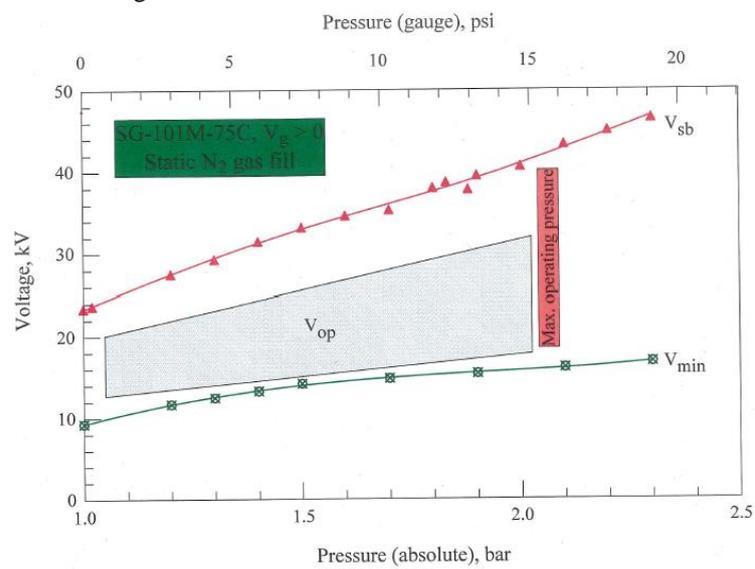
Figure 6.8 Operation curve for SG-101M-75C [6.7]

6.1.2.2.   Closing switch

In high voltage pulse generators closing or opening switches, such as spark gaps, are important components of pulsed power circuitry and the system output performance is critically dependent on their characteristics. Closing spark gap switches depend on the functions they perform. In generators for example, it may be necessary to have a short switching time $t_s = 10^{-19} - 10^{-8} s$ [6.8]. Spark gap switches display an excellent voltage withstand capability (as high as a few MV), and a high charge transfer capability. In addition, their operation can be synchronized with other circuit elements by triggering them through a third electrode. A gas switch can be considered to be electrically closed when under a high electric field stress the insulating gas between the electrodes becomes conducting and a plasma channel develops. This transition of the switch from the insulating to the conducting state can be explained in two ways, the Townsend model and the streamer model. Two electrode switches are widely used in repetitive system generators. The gas flow velocity should be sufficiently high to remove plasma from the gap within the pulse interval, but not too high so as to keep the discharge region at the cathode heated in order that initiating electrons will appear during the discharge initiated by the next pulse [6.9].

A low-inductance insulation breakdown closing switch was designed by Loughborough [6.10]. The schematic diagram of the spark gap switch is presented in Figure 6.9, in which (1) are the pins of the switch, (2) is the electrode bar, (3) SF_6 gas at 15-18 bar.
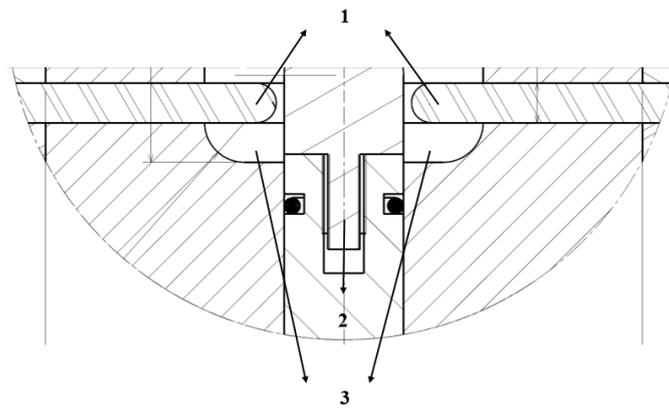
Figure 6.9 Schematic diagram of the spark gap switch

The high-voltage spark-gap will operate in a self-breakdown mode in a pressurised SF$_6$ environment. The switch is made with the HV electrode in the form of a bar and with the ground electrode having the form of a disc with a hole placed co-axially with the bar. The breakdown distance is 7.5 mm and the HV electrode can be changed relatively easily with the aid of multi-contact technology. The dimensions of the HV electrode and the electrode bar are shown in Figure 6.10 and 6.11.
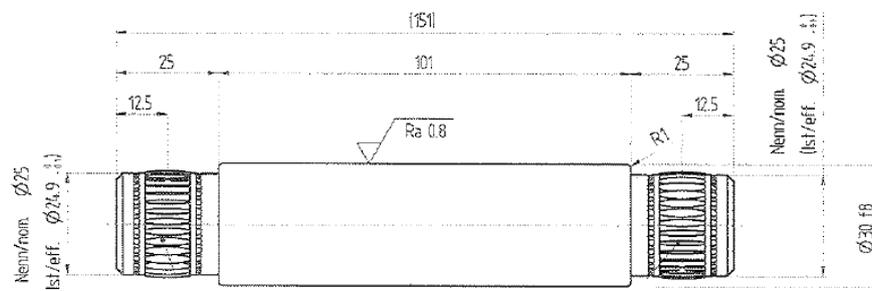
Figure 6.10 Dimensions of the spark gap switch HV electrode

Figure 6.11 HV electrode bar of spark gap

6.1.2.3.   Gas arrangement

There are two types of gas used in the experiments. The gases were used in three switches: trigatron SG-101M-75C in Tesla transformer, main switch spark gap before the Blumlein PFL and the bipolar switch in bipolar former. Nitrogen and Sulphur Hexafluoride were both bought from BOC company [6.11].

➢ Nitrogen (Oxygen-Free) (Figure 6.12)

Odourless and colourless; non-toxic; inert, dry and slightly soluble; Available in 300-bar MCPs; Inert to nearly all substances at ambient temperatures and moderate conditions; nitrogen keeps laser-cut faces oxide-free due to the chemical inertness to react with the atmosphere.[6.12]

Figure 6.12 Nitrogen(Oxygen-Free) arrangement

➢ Sulphur Hexafluoride (Figure 6.13)

Sulphur Hexafluoride is colourless and odourless gas whose chemical formula is SF_6. It is asphyxiant gas in high concentrations, so do not allow back feed into the container. For security, SF_6 should be use only in properly specified equipment which is suitable, the cylinders should be protected from physical damage, and damaged valves should be reported immediately to the supplier. Then replace valve outlet caps or plugs and container caps where supplied as soon as container is disconnected from equipment. SF_6 must not be discharged to atmosphere and discharged3 into any place where its accumulation could be dangerous, refer to the EIGA code of practice (Doc.30 "Disposal of Gases"[6.13]) for more guidance on suitable disposal methods. [6.14]

Figure 6.13 Sulphur Hexafluoride arrangement

The amount of the pressure gas used in the three switches was:

➤ Trigatron SG-101M-75C: 1.5 bar -2.0 bar nitrogen at initial voltage between 20 kV to 30 kV. (Figure 6.8)[6.7]

➤ Spark gap: SF_6 has unique properties which render SF_6 a nearly ideal medium for arc interruption and dielectric strength. The dielectric strength is greater than any other known medium at the same density. The reason lies in the relatively large physical size and mass. The molecular weight is 146. Nitrogen and Oxygen are 28 and 32 respectively. The size and mass help reduce the propagation of free electrons. SF_6 also acts as an inelastic damper for collision mechanism. The higher densities and pressures increase the liquefaction temperature, a very unsatisfactory side effect. Figure 6.14 shows the curve which was used to maintain the gas warm to allow a prudent reserve heat mass as a safety margin [6.15]. 16 bar – 18 bar SF_6 was used for main switch in experiments.
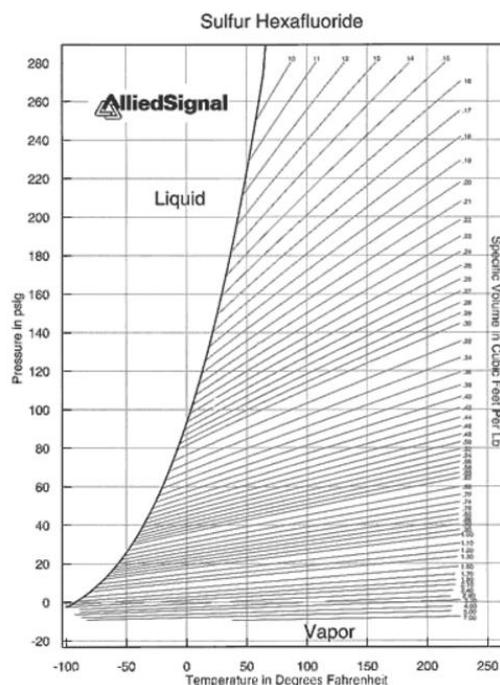
Figure 6.14 Operation curve of Sulfur Hexafluoride [6.15]

➢ Bipolar closing switches: both bipolar switches designed in Chapter 4 operate at very high voltage and for both it is desirable to provide the shortest rise time possible. In such case usually the best gas to be used is H_2 and possibly N_2. Both gases require very large pressures but, unfortunately, in the present bipolar system the maximum operable overpressure is only 20 bar, insufficient for the switches to be operated at very high-voltage. In order to withstand high-voltage levels at lower pressure, SF_6 can replace H_2 or N_2 but, due to its heavier molecular mass, the resulting rise time will become unacceptable slow. Previous experience demonstrated that SF_6-N_2 mixtures are the simplest substitute for pure SF_6, as even a small amount of SF_6 mixed with N_2 results in a substantial increase in the breakdown electric field of pure N_2. For example, experiments demonstrated [6.16] that only 10% of SF_6 is required to increase the critical reduced field of pure N_2 to about 70% of that of pure SF_6 (Figure 6.15). A somehow unexpected benefit, also demonstrated experimentally[6.17], is that the rise time of a switch operated with certain SF_6-N_2 mixtures can be lower than with the same switch using pure N_2 gas (Figure 6.16). Based on these results, it was decided to operate the bipolar switches at 20 bar using a 10%-90% SF_6-N_2 mixture.
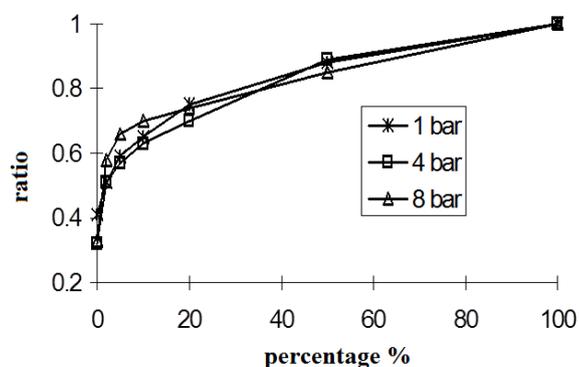
Figure 6.15 Influence of SF_6 percentage on the ratio electric field breakdown for SF_6-N_2 mixture to pure SF_6 [6.16]
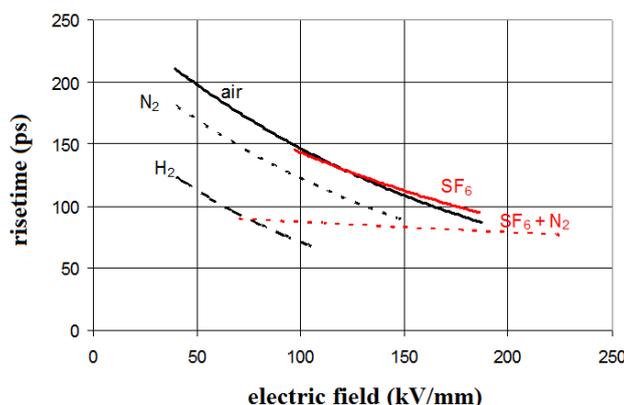
Figure 6.16 Experimentally determined rise time of the voltage impulse as a function of the applied electric field for a closing switch operated using gases: H_2, Air, N_2, pure SF_6 and SF_6-N_2 mixture [6.17]

6.1.3. Resistive load

An oil-immersed high voltage resistive load was designed and manufactured to test the Tesla-Blumlein generator before the bipolar former mounted. The oil-immersed high voltage resistive load was manufactured by HVR [6.18]. Table 6-2 presents the coaxial resistor specification. Figure 6.17 shows the side view of the drawing. $R_{load} = 30 \, \Omega$ was designed to match the Blumlein PFL and the resistive load comprises $N_{discs} = 12 \, discs$, each with an outer diameter $d_{load} = 50 \, mm$ and a length $l_{disc} = 25.4 \, mm$ and held under pressure by four plastic bars (Figure 6.18(a)). The resistor is positioned coaxially inside a stainless steel cylinder with an inner diameter $D_{load} = 130 \, mm$ by a Multi-Contact connector [6.19] (Figure 6.18(b)). When driven by a fast rising voltage impulse, the load acts like a transmission line.

Table 6-2 Resistive load specification

Parameter	Specification
Resistance value	30 Ω
Peak voltage	500 kV
Energy per impulse	140 J
Environment	Transformer oil
Resistor weight	2.5 kg
Volume of active material	321.6 cm^3
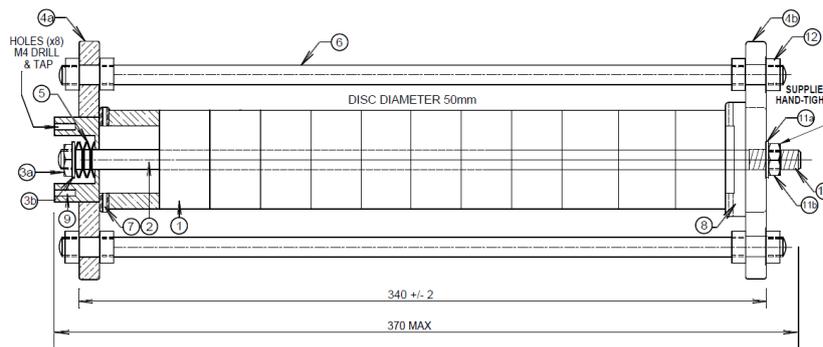
Figure 6.17 Side view of the resistive load: (1)ceramic resistor disc type M002C; (2)&(6) threaded delglas rod; (3)&(11) brass retaining nut & flat washer; (4)glastic insulated cover; (5)schnorr disc spring; (7)&(8)brass oil ported terminal; (9)brass ring terminal; (10)brass stud terminal; (12)glastic nut.

Figure 6.18 30 Ω resistive load (a) resistor showing Multi-Contact end connector; (b) this connector allows very convenient mounting of the load.

6.1.4. Oscilloscopes

The three diagnostics installed were connected using double shielded 18 GHz coaxial cables and attenuators (Figure 6.19), to two oscilloscopes. The high performance fixed attenuators are from ARRA Inc. [6.20]. The extremely wide bandwidth is DC-18.0

GHz and the attenuation values are 3, 6, 10 & 20 dB. Nominal impedance is 50 Ω and the attenuators are based on model AN944 type N connectors.

Figure 6.19 High performance fixed attenuators [6.20]

6.1.4.1. Tektronix TDS 654C digital real-time oscilloscope 500 MHz [6.21]

The Tesla transformer output sensor was connected to Tektronix TDS 654C digital real-time 500 MHz oscilloscope. Its 500 MHz bandwidth preserves waveform's fast rising edges and accurately shows signal details. With 5 GS/s digitizing rate simultaneously on all four channels and a high-stability timebase, it makes critical timing measurements with the highest resolution and accuracy.

Figure 6.20 Tektronix TDS 654C digital real-time oscilloscope 500MHz [6.21]

6.1.4.2. Teledyne LeCroy SDA18000 real-time digital oscilloscope 18 GHz [6.22]

The Blumlein and bipolar ultrafast output sensors are connected to a 18 GHz bandwidth, 60 GS/s LeCroy real-time digital oscilloscope: Blumlein output sensor to

a 6 GHz bandwidth input and bipolar sensor to a 18 GHz input. The oscilloscope is

housed in a Faraday box and powered by a UPS unit.

Figure 6.21 Teledyne LeCroy SDA18000 real-time digital oscilloscope 18 GHz [6.22]

6.2.   Numerical modelling

OrCAD PSpice [6.23] is an analysis software to deliver a complete circuit simulation

and verification solution, which provides the best, high-performance circuit simulation

to analyse and refine the circuits, components, and parameters before committing to

layout and fabrication. The PSpice simulation was used to achieve the simulation

results which were compared with the experimental results.

6.2.1. Tesla-Blumlein PSpice modelling

The PSpice model of the Tesla-Blumlein generator is presented in Figure 6.22. From

left to right it is easy to recognize the HV charging unit, followed by the bank circuit

and the Tesla transformer. $V_0 = 30\ kV$ is the initial voltage, C_1 is the capacitor bank,

U_1 presents the trigatron SG-101M-75C, TX_1 is the Tesla transformer. From

preliminary testing of the primary winding circuit of the Tesla transformer without the

secondary winding present and undertaken at very low voltage using the low-

inductance insulation breakdown closing switch, showed that the overall self-

inductance of the bank, including the switch and a short transmission line, is about 32.5 nH. This enables the natural resonant frequency of the primary winding circuit to be calculated as about 449 kHz, almost equal to that of the secondary winding circuit and therefore satisfying the essential requirement for the dual resonant condition to be fulfilled. Using data from the manufacture, the frequency can then be used to estimate the equivalent series resistance (ESR) of the capacitor bank as $R_b \approx \frac{8}{2}\ m\Omega = 4\ m\Omega$. Therefore the overall resistance of the primary winding circuit as $R_1 = R_b + R_{switch} + R_{pw}^0$. The trigatron resistance R_{switch} varies with the operating voltage, from tens of $m\Omega s$ at $V_0 = 20\ kV$ to about $1 m\Omega$ at $V_0 = 30\ kV$. The Blumlein PFL HV closing switch includes a series self-inductance $(15\ nH)$ and a parallel equivalent capacitance $(1.6\ pF)$. A small value inductor, placed between the switch and the Blumlein PFL, controls the duration of the load voltage impulse to meet the specific application. For a charging voltage $V_0 = 30\ kV$ and a $38\ nH$ inductor, the FWHM is $15\ ns$ and the load peak voltage close to $600\ kV$, and when the inductance is $20\ nH$ or less, the FWHM is reduced to less than $10\ ns$, with the load peak voltage increasing to $640\ kV$ or even higher. To the right in the PSpice model is the Blumlein PFL, followed by two very short transmission lines corresponding to two transition parts, connecting the Blumelin PFL to the testing resistive load, while maintaining the HV integrity during charging. The load itself is modelled as a transmission line with distributed inductance, capacitance and resistance. These electrical characteristics per unit length were calculated as follows:

$$C_{T5} = \frac{2\pi\varepsilon_0\varepsilon_{oil}}{\ln\left(\frac{D_{load}}{d_{load}}\right)} \tag{6.01}$$

$$L_{T5} = \frac{\mu_0}{2\pi} \ln \left(\frac{D_{load}}{d_{load}} \right) \tag{6.02}$$

$$R_{T5} = \frac{R_{load}}{N_{disc} l_{disc}} \tag{6.03}$$

Finally, a small correction due to the transient skin depth effect was applied on L_{T5}.
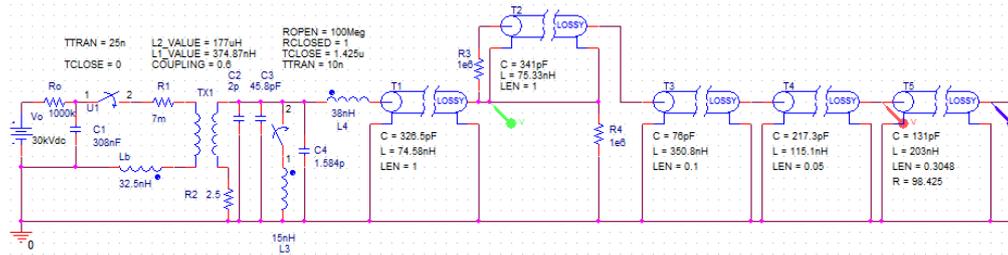
Figure 6.22 PSpice model of the Tesla-Blumlein generator

6.2.2. Tesla-Blumlein-bipolar PSpice modelling

Figure 6.23 shows the PSpice model for the entire system (Tesla-Blumlein PFL-bipolar former). Part a, b, c show the Tesla-Blumlein PFL generator mentioned. R_5 is the $130\,\Omega$ CuSO4 resistor which replaced the testing resistive load. Part d shows three very short transmission lines and followed by the two closing switches in bipolar former. Each HV closing switch includes a series self-inductance and a parallel equivalent capacitance obtained from Maxwell software calculations. Part e and f are the bipolar former and a short-circuited $50\,\Omega$ line output.

Figure 6.23 PSpice model of Tesla-Blumlein PFL-bipolar former system

6.3. References

[6.1] http://www.us.tdk-lambda.com/hp/product_html/202apower.htm. Last accessed 9th February 2015.

[6.2] S T Pai and Qi Zhang (1995). *Introduction to high power pulse technology*. Singapore: World Scientific Publishing Co. Pre. Ltd..

[6.3] http://www.ga.com/capacitor-product-guide. Last accessed 9th February 2015.

[6.4] http://www.reb3.com/. Last accessed 9th February 2015.
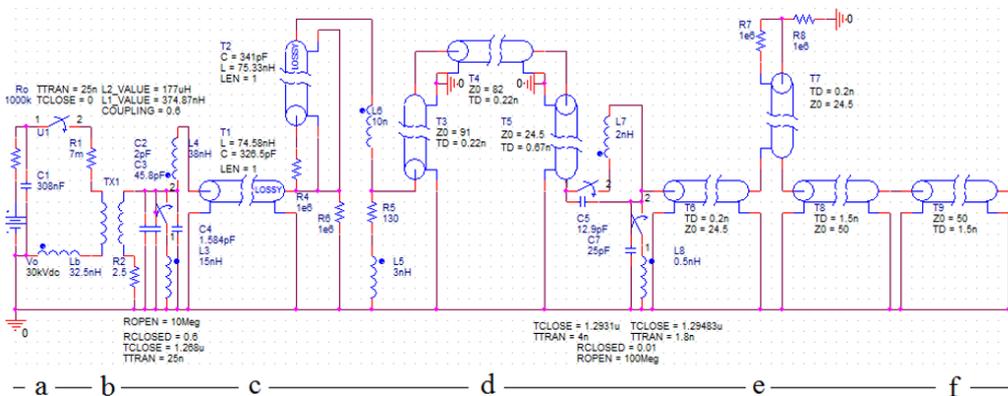
[6.5] http://www.reb3.com/docs.html. Last accessed 9th February 2015.

[6.6] http://www.reb3.com/pdf/pg103d_specs.pdf. Last accessed 9th February 2015.

[6.7] http://www.reb3.com/pdf/sg_specs.pdf. Last accessed 9th February 2015.

[6.8] Gennady A. Mesyats (2005). *Pulsed Power*. U.S.A: Springer Science Business Media Inc..

[6.9] Ihor Vitkovitsky (1987). *High Power Switching*. New York: Van Nostrand Reinhold Company Inc..

[6.10] P. Senior, C. D. Hacker, B. M. Novac and I. R. Smith (1997). Switch characteristics for a high efficiency 20 kJ electromagnetic launcher. *Proc. 11th IEEE International Pulsed Power Conference*. Baltimore, Maryland, USA. pp1144-1149.

[6.11] http://www.boconline.co.uk/en/index.html. Last accessed 9th February 2015.

[6.12]http://www.boconline.co.uk/en/products-and-supply/industrial-gases/inert-gases/nitrogen-oxygen-free/nitrogen.html. Last accessed 9th February 2015.

[6.13] http://www.eiga.org. Last accessed 9th February 2015.

[6.14]http://www.boconline.co.uk/en/products-and-supply/speciality-gas/pure-gases/sulphur-hexafluoride/sulphur-hexafluoride.html. Last accessed 9th February 2015.

[6.15]http://www.metatechcorp.com/aps/cold_weather_operating_problems_.htm. Last accessed 9th February 2015.

[6.16] L. Pecastaing, T. Reess, P. Espel, J. Paillol, A. Gibert and P. Domens (1999). Investigation of breakdown characteristics of N_2, SF_6 and N_2-SF_6 mixtures under pressure. *Proc. 11th International Symposium on High Voltage Engineering*. London, UK. pp224-227.

[6.17] G. Bouttemant, L. Pecastaing, J. Paillol, and T. Reess (2004). High speed pressurised gas breakdown in a high voltage ultrawideband pulse generator. *Proc. 15th International Conference on Gas Discharge and their Applications*. Toulouse, French.

[6.18] http://www.hveint.com. Last accessed 9th February 2015.

[6.19] http://www.multi-contact.com. Last accessed 9th February 2015.

[6.20] http://www.arra.com/attenuators.html. Last accessed 9th February 2015.

[6.21] http://uk.tek.com/oscilloscope#all. Last accessed 9th February 2015.

[6.22] http://teledynelecroy.com/oscilloscope/. Last accessed 9th February 2015.

[6.23]   http://www.orcad.com/products/orcad-pspice-designer/overview.   Last

accessed 9th February 2015.

7. Results

A range of experiments was carried out on the pulsed power generator. The experimental results are generally in good agreement with data predicted from numerical modelling and have provided theoretical justification of the bipolar pulsed power generator properties. The following section provides details of the testing results of individual system and whole system. As a preliminary test, experiments were carried out to measure the performance of the Tesla-Blumlein PFL generator. Since the bipolar former generates an extremely high voltage and fast transient pulse, ultrafast V-dot sensors were used to measure the results. Experimental results obtained during the major experimental program are compared with theoretical predictions.

7.1. Tesla-driven Blumlein pulsed power generator

7.1.1. Single-shot operation

In an effort to investigate the limits, at an initial bank charging voltage of $V_0 = 30\ kV$, operation of the system begins with Blumlein-PFL being charged by the Tesla transformer for 1.4 µs, followed by the fast discharge of the Blumlein-PFL (Figure 7.1). The record voltage impulse has a peak time rate-of-change of about $225\ \text{kV/ns}$, and an integrated peak of $V_{peak} = 596\ kV$, with a rise time of 2.2 ns, (Figure 7.2). The corresponding overall Tesla transformer efficiency is in this case

$$\eta = \frac{C_p V_0^2}{C_s V_{peak}^2} \approx 92\% \tag{7.01}$$

and, after the Blumlein PFL HV switch closes, a percentage of the energy is transferred to the resistive load with a peak instantaneous power of 10 GW, which maintains over 6 GW for 10 ns and 9 GW for 5 ns. (Figure 7.3)
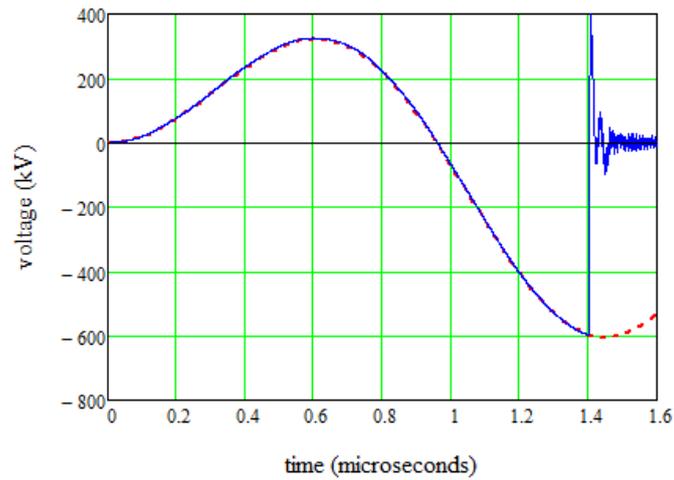
a)
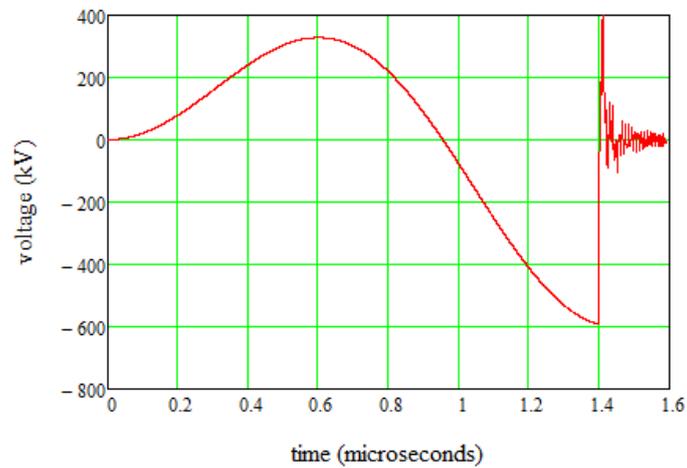
b)

Figure 7.1 Time history of Blumlein PFL voltage during a 0.6 MV shot; (a) experimental data (continuous blue line) compared with 2D filamentary modelling(dotted red line); (b) PSpice prediction. Time origin from the bank switch closure.
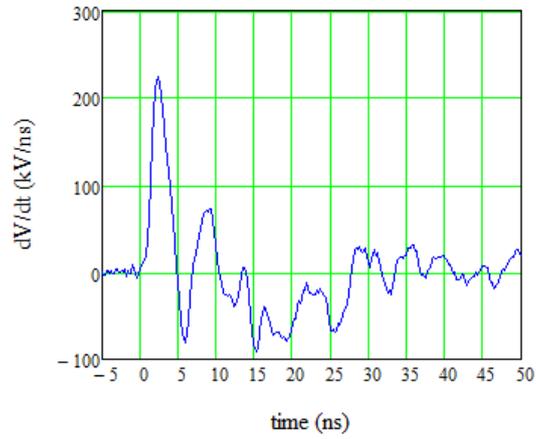
a)
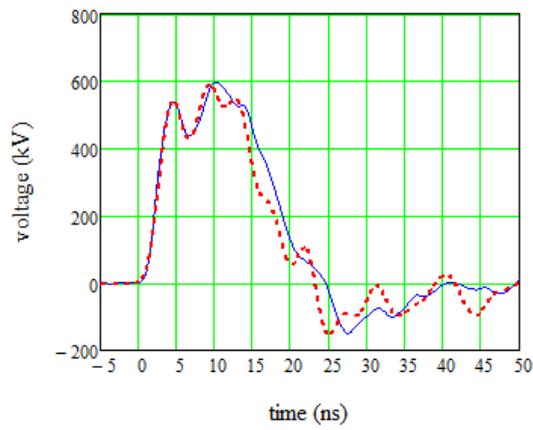
b)

Figure 7.2 Load voltage corresponding to the test of Figure 7.1; (a) time rate-of-change signal; (b) integrated voltage(continuous blue line), compared with PSpice prediction(dotted red line); time origin from the Blumelin PFL HV switch closure.
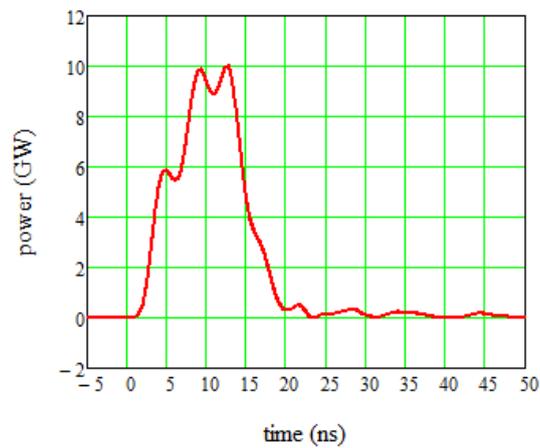
Figure 7.3 Instantaneous load power corresponding to data in Figure 7.1 and Figure 7.2. Time origin from Blumlein PFL HV switch closure.

7.1.2. Repetitive operation

Typically, the generator is operated at a peak load voltage close to $500\,kV$ (Figure 7.4), with an experimentally observed dispersion of the peak load voltage for five 'identical' consecutive shots being $485\,kV \pm 3\%$. The corresponding peak instantaneous power is about $7\,GW$. Repetitive operation, in bursts of five shots, has been tested between $1\,Hz$ and $2\,Hz$, with the dispersion in the load voltage being $\pm 8\%$. Flowing SF_6 gas during discharge or re-design of the spark gap will both increase the repetition rate that can be achieved and the reproducibility of the peak load voltage.

a)

b)

Figure 7.4 Load voltage and current corresponding to a standard $\approx 0.5\,MV$ test. Integrated signals (a) voltage and (b) current; experimental data(continuous blue lines) compared with PSpice prediction(dotted red lines); for convenience the current is presented as positive; time origin from Blumlein PFL HV switch closure.
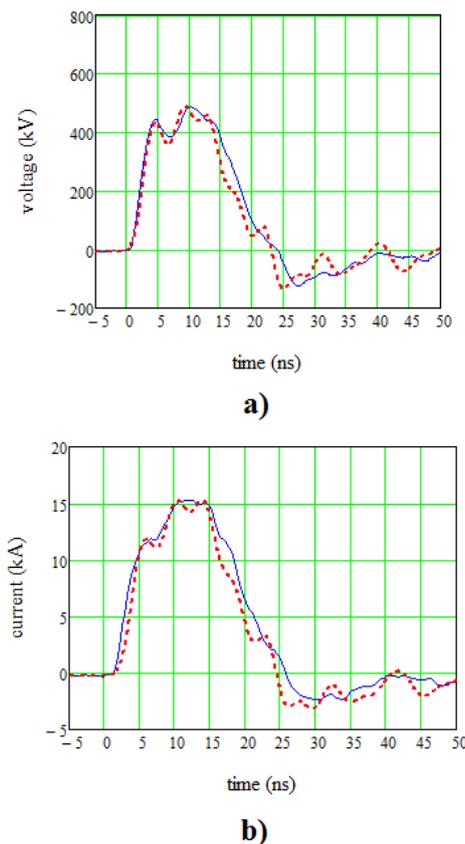
141

7.2. Bipolar modulation of the output of the Tesla-Blumlein PFL generator

After the preliminary work on Tesla-Blumlein PFL generator, a bipolar former was attached to the 10 GW generator. As design details shown in chapter 4, the testing resistive load was replaced by a 130 Ω parallel-coupled CuSO$_4$ resistor. Although the resistors are operated under oil, calculations predicted that they have to withstand a very high output voltage impulse that can attain value well in excess of 0.6 MV, the peak voltage inside the previously developed Tesla-Blumlein PFL generator. A series of experiments have been performed therefore to test the resistors under high-voltage loading, by operating the attached bipolar former without its second grounding switch. The results obtained clearly demonstrate the resistors are capable, together with the central electrode of the Blumlein PFL, of maintaining their electrical integrity up to and even above 0.9 MV (Figure 7.5), a performance in excess of the design expectations.

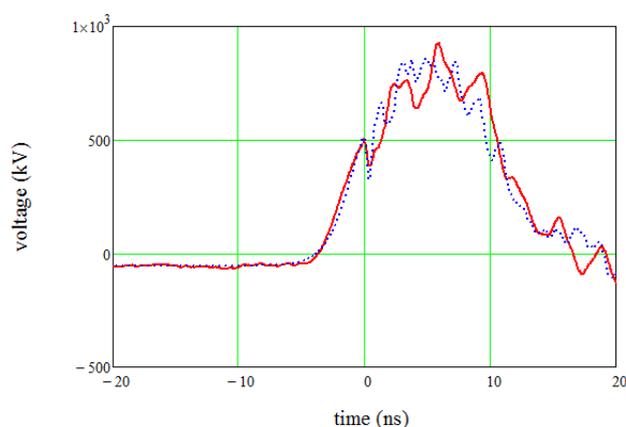Figure 7.5 Blumlein PFL output voltage with a parallel-connected 130 Ω resistance and a bipolar former operated with grounding switch. The continuous red line represents experimental data, while the dotted blue line represents the corresponding PSpice simulation. The time origin is from the action of the action of the 500 kV bipolar former first closing switch, connecting the unit to the Blumlein PFL.

After bipolar former with two closing switches mounted, a series of experiments were constructed to find the optimum combinations of the gaps for the two switches mounted at the bipolar former input. Table 7-1 presents an overview of the main results during the experimental study. Figure 7.6 shows a number of output signals clearly indicating the progress made in increasing the first positive voltage peak.

Table 7-1 Results from the study on the two closing switch gaps of the large-size bipolar former

Peaking switch gap (mm)	Grounding switch gap (mm)	Positive voltage peak (kV)	Negative voltage peak (kV)	Peak dV/dt (MV/ns)	Voltage signal shown in Figure 7.6
0.8	1.2	108	-264	1.5	a
0.8	1.5	139	-391	2.1	b
1.0	1.3	143	-332	1.7	c
1.3	1.3	152	-313	1.8	d
1.9	1.4	165	-303	2.4	−
2.0	1.3	157	-340	2.1	e
2.0	1.5	185	-312	2.0	f
2.0	1.65	205	-353	2.7	g
2.0	1.75	229	-394	2.2	h
2.1	1.65	240	-387	2.8	i
2.2	1.4	176	-306	2.9	−
2.2	1.6	220	-339	2.7	−
2.2	1.65	273	-382	2.3	−
2.2	1.75	232	-353	2.3	−
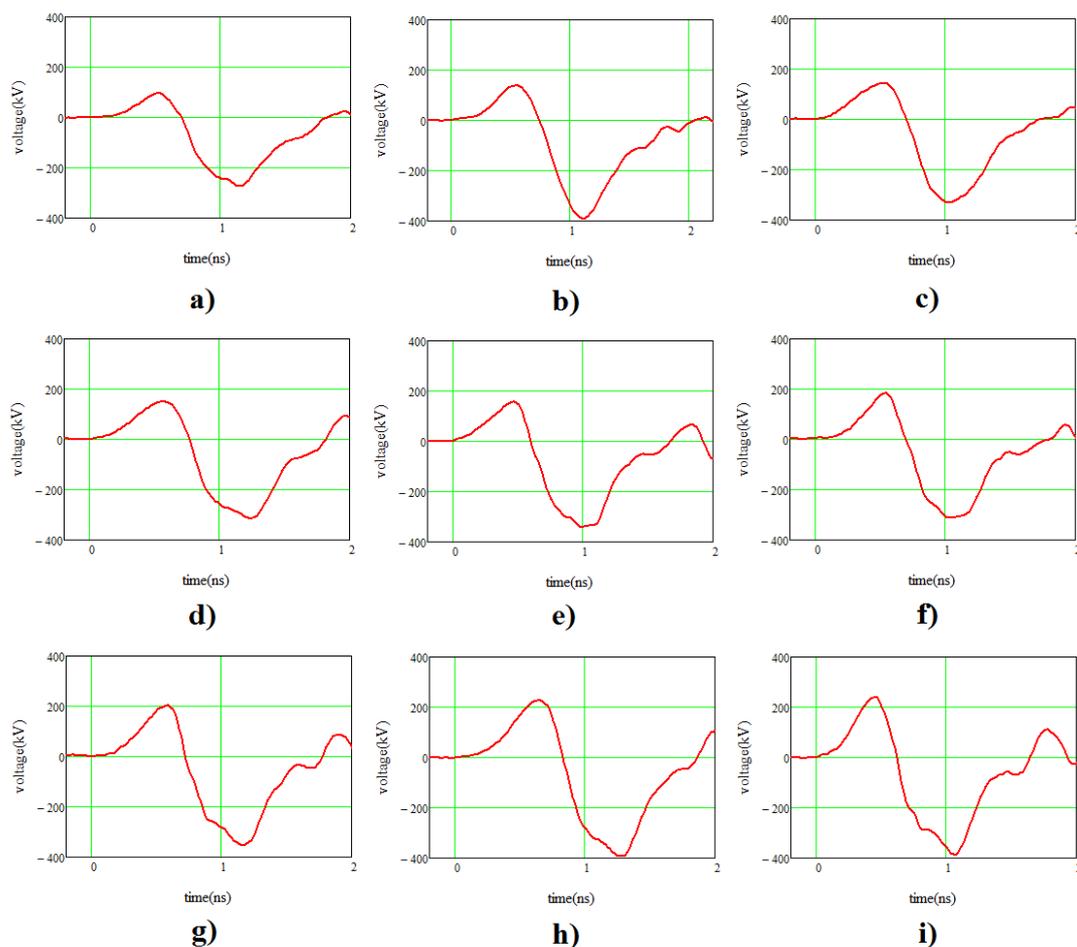
Figure 7.6 Load voltage impulses generated by the bipolar former during the process of adjusting the bipolar former switch gaps: a continuous increase in the first positive peak can be clearly observed. Time origin from the connecting bipolar switch closure.

Figure 7.7 presents the results obtained with a gap combination of 2.2 mm with 1.65 mm. The resulting bipolar signal has a first rise time of about 300 ps, a peak-to-peak value of 650 kV with a time interval between the two peaks approximately 550 ps and a peak time rate-of-change of the voltage signal in excess of 2 MV/ns. Figure 7.8 show the best match predicted voltage signals from the Tesla-Blumlein PFL-bipolar former PSpice model delivered by the bipolar former into the 50 Ω output transmission line when the driver Blumlein PFL generator operates close to its peak performance.
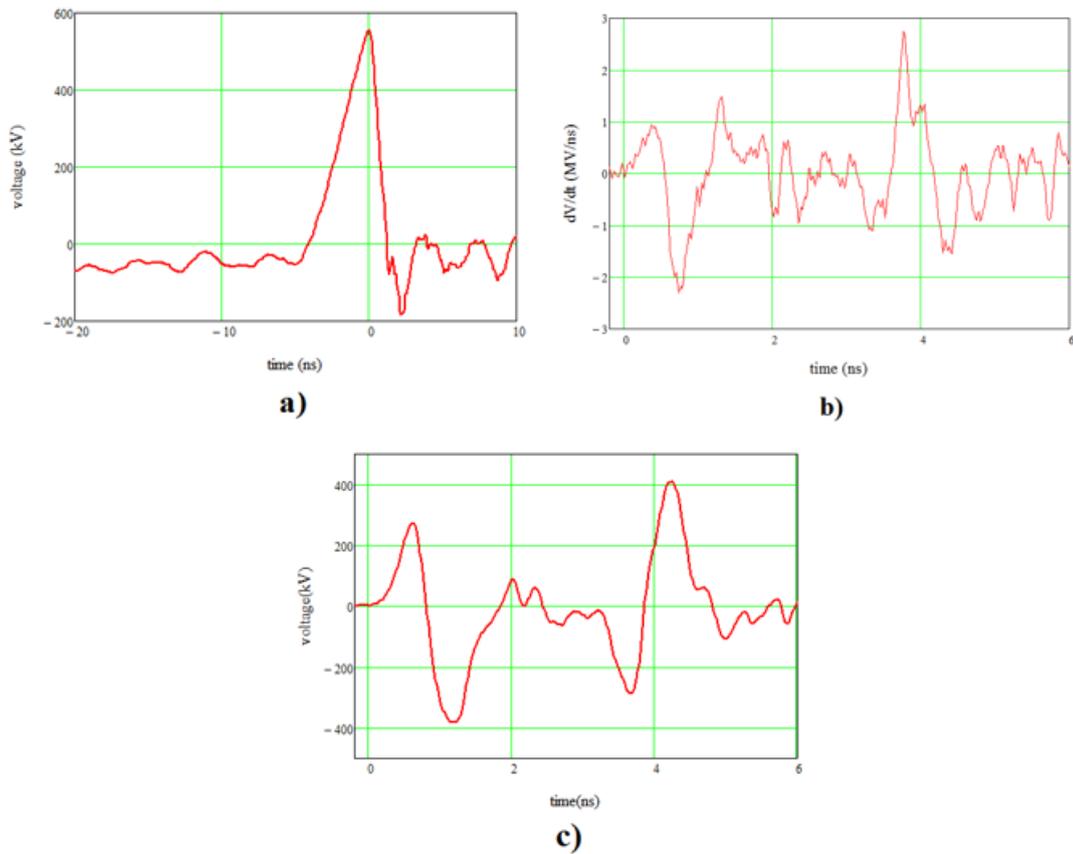
Figure 7.7 Typical experimental results from the final pulsed power system. (a) Blumlein PFL output voltage impulse; (b) dV/dt signal recorded by the bipolar output probe; (c) integrated bipolar voltage generated inside the 50 Ω output transmission line, followed by its reversed polarity mirror image produced by reflection at the short-circuited end. In all cases the time origin is from the closing switch action connecting the bipolar former to the Blumlein PFL.
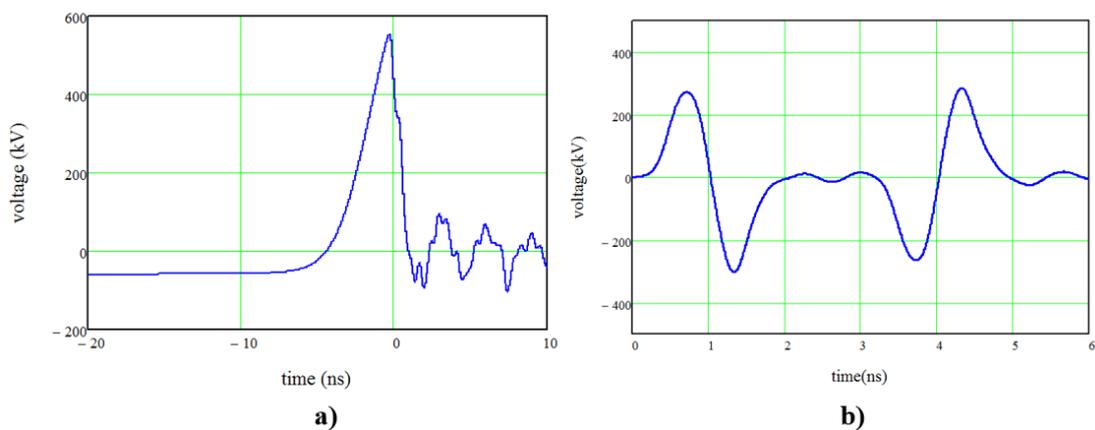
Figure 7.8 Main results from PSpice modelling: (a) Blumlein output voltage impulse; (b) bipolar voltage generated inside the 50 Ω output transmission line, followed by its reversed polarity mirror image produced by reflection at the short-circuited end. In both cases the time origin is from the closing switch action connecting the bipolar former to the Blumlein PFL.

The monopolar output of the 10 GW Tesla-Blumlein PFL pulsed power generator has been successfully time-compressed and modulated using a bipolar former. The resulting sinusoidal-like shape of the bipolar output voltage impulse has a peak-to-peak voltage of 650 kV and a frequency approaching 1 GHz(Figure 7.9), close to expectations in chapter 4.

Figure 7.9 Comparison between the previously demonstrated 600 kV monopolar Blumlein PFL output (dotted red line) and the 650 kV peak-to-peak time-compressed and modulated signal generated by the bipolar former (continuous blue line) in: (a) time domain and (b) frequency domain.

8. Conclusions and the way ahead

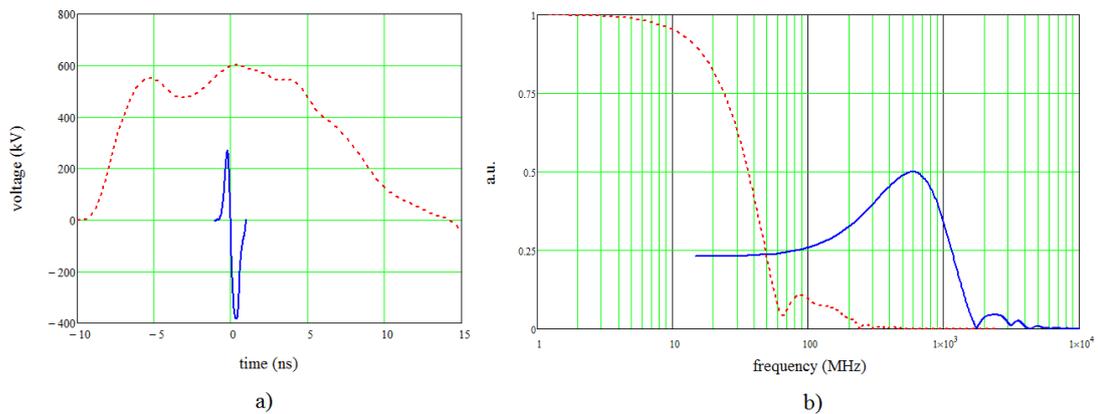## 8.1. Major personal achievements

The research programme described in this thesis was focused on the Tesla-Blumlein PFL-Bipolar pulsed power generator. A compact Tesla transformer has been developed and has successfully charged capacitive loads to peak voltages up to 0.6 MV with an overall energy efficiency in excess of 90%. Based on this unit, a Blumlein PFL pulsed power generator has been designed, manufactured and successfully tested. The Tesla-Blumlein PFL generator is capable of producing a voltage impulse approaching 0.6 MV with a rise time close to 2 ns, generating a peak instantaneous power of 10 GW, which maintains over 6 GW for 10 ns and 9 GW for 5 ns when connected to a 30 Ω resistive load. Repetitive operation has been demonstrated at lower voltage and power levels. After improving the Blumlein PFL HV switch operation and replacing the static 30 Ω load resistor with a $CuSO_4$ resistor, a bipolar former was designed, manufactured and mounted including a pair of very fast acting high pressure closing switches. The monopolar output of the Tesla-Blumlein PFL generator has been successfully time-compressed and modulated. An experimental study to find the optimum combinations of the gaps of the two closing switches mounted at the bipolar former input was demonstrated. The resulting sinusoidal like shape of the bipolar output voltage impulse has a peak-to-peak voltage of 650 kV and a frequency beyond 1 GHz. All experimental results obtained were compared with numerical modelling results.

8.1.1. Tesla-Blumlein PFL generator

First complete and precise calculation of both capacitances and inductances that allow an ideal design to be generated. In particular, only using these filamentary techniques, it was possible to achieve 93% efficiency. In the performance study of Tesla-Blumlein PFL generator, a self-inductance placed near the Blumlein PFL HV closing switch was used to control the load voltage impulse characteristics and increase the pulse duration to meet the specific application. Complete work of Tesla-Blumlein PFL generator was fully published and acknowledged at an international conference 'EAPPC 2014 5th Euro-Asian Pulsed Power Conference' by obtaining the award 'Best Student Award'.

8.1.2. Bipolar former

First detailed numerical modelling and experimental techniques for optimizing the two closing switches of the bipolar former. The original use of the off-the-shelf sensors backed with the CST detailed modelling and calibration. A three-dimensional model for V-dot sensors, using the Computer Simulation Technology (CST) electromagnetic microwave studio software, suggests that off-the-shelf N-type connectors can be directly used as ultrafast probes up to a frequency of 6 GHz. By using dedicated experimental assemblies, it is demonstrated in practice that such sensors have indeed the characteristics indicated by the CST model. The off-the-shelf N-type adaptors have recently been successfully used to accurately measure the 1 GHz, ± 250 kV output from the generator. Explain and present the importance of connect pointing of the sensors along a transmission line, far from the spark gap. These findings are the main objects of a new paper that is about to published and were acknowledged at an international

conference '2015 IEEE International Pulsed Power Conference' by obtaining the award 'IEEE Nuclear and Plasma Sciences Society 2015 Best Student Paper Award'.

8.1.3. Electro-optic sensors

The Kerr constant for water at 658 nm for a range of temperatures between 19 ℃ and 45 ℃ has been accurately defined. The results obtained represent an important step in the development of a reliable and accurate very fast pulsed and intense electric field measurement technique. It is of particular value for PEF treatment systems and in general for water-filled HV pulsed power components such as transmission lines, capacitors and spark gaps.

8.2.   The way ahead

Based on the findings reported it is possible to think about the design of a future system for the medical application. The application is to use the generator for medical cancer treatment, by attaching to its output an antenna to remotely generate intense pulsed electric fields (PEF). The generator is now fully prepared to be connected to an antenna for beginning the study of application.

8.3.   Worldwide recognition

8.3.1. Awards

(1) EAPPC 2014 5th Euro-Asian Pulsed Power Conference Best Student Award, Kumamoto, Japan, 2014.

(2) IEEE Nuclear and Plasma Sciences Society 2015 Best Student Paper Award (IEEE International Pulsed Power Conference) Austin, USA, 2015.

8.3.2. Publications

Journal Publications

(1) B. M. Novac, **M. Wang**, I. R. Smith and P. Senior (2014). A 10 GW Tesla-Driven Blumlein Pulsed Power Generator. *IEEE Transactions on plasma science*. 42(10),. pp2876-2885.

(2) **M. Wang**, B. Novac, L. Pecastaing, I. Smith (2016). Bipolar modulation of the output of a 10 GW pulsed power generator. Accepted for publication in the IEEE Transactions on Plasma Science.

(3) B. M. Novac, R. Ruscassie, **M. Wang**, A. De Ferron, L. Pecastaing, I. R. Smith and J. Yin (2016). Temperature dependence of Kerr constant for water at 658 nm and for pulsed intense electric fields. Accepted for publication in the IEEE Transactions on Plasma Science.

(4) **M. Wang**, B. Novac, L. Pecastaing, I. Smith (2016). Ultrafast off-the-shelf V-dot Probes: Theory and Experimentation. Will be submitted and published in the IEEE Transactions on Plasma Science soon.

Conference publications

(5) **M. Wang**, B. M. Novac, I. R. Smith and P. Senior (2014). A 10 GW Pulsed Power Generator. *UK Pulsed Power Symposium*. Loughborough, UK.

(6) **M. Wang**, B. M. Novac, I. R. Smith and P. Senior (2014). A 10 GW Pulsed Power Generator. *2014 IEEE International Power Modulator and High Voltage Conference.* Santa Fe, USA.

(7) **M. Wang**, B. M. Novac, I. R. Smith and P. Senior (2014). A 10 GW Pulsed Power Generator. *5th Euro-Asian Pulsed Power Conference.* Kumamoto, Japan. (Best Student Award)

(8) B. M. Novac, R. Ruscassie, **M. Wang**, A. De Ferrou, L. Pecastaing, P. Pignolet and I. R. Smith (2015). Determination of the Temperature Variation of the Kerr Constant of Water: Preliminary Results. *20th IEEE International Pulsed Power Conference 2015.* Austin, TX, USA.

(9) B. M. Novac, L. Pecastaing, **M. Wang** and A. De Ferrou (2015). Ultrafast off the Shelf V-dot Probes: Theory and Experimentation. *42nd IEEE International Conference on Plasma Science 2015.* Belek, Antalya, Turkey.

(10) **M. Wang**, B. M. Novac, L. Pecastaing, P. Senior and I. R. Smith (2015). Additional Pulse Compression and Modulation of the Output of A 10 GW, Tesla-Blumlein Generator. *20th IEEE International Pulsed Power Conference 2015.* Austin, TX, USA. (Best Student Paper Award)

(11) B. M. Novac, **M. Wang**, L. Pecastaing, P. Senior and I. R. Smith (2016). 600 kV Bipolar output Tesla-Blumlein generator with frequency bandwidth > 1 GHz. *IEEE International Power Modulator and High Voltage Conference 2016.* San Francisco, CA, USA.